sciendo

Slovak Journal of Civil Engineering

Vol. 32, 2024, No. 1, 1 – 9
DOI: 10.2478/sjce-2024-0001

EFFECT OF STRAPPING STRAPS WASTE FIBERS ON FRESH AND HARDENED PROPERTIES OF CONCRETE

Rachid DJEBIEN[1*], Rachid KEBOUT[1], Mouloud BELACHIA[2]

Abstract

Faced with the increasingly growing need for construction material resources and the strict requirements and conditions for preserving the environment, it has become necessary and relevant to study all possibilities and opportunities for the recycling and valorization of industrial waste and by-products in the construction field. Strapping straps is a product used to bundle and transport goods and construction materials. After its use, it is considered as waste. The objective of this experimental work is to study the possibility of reusing the strapping strap waste as fibers in the production of fiber-reinforced concrete. For this purpose, three families of concrete were composed using strapping strap fibers, steel fibers, and polypropylene fibers, which were introduced into a concrete composition by volumetric substitution (0.4%, 0.8% and 1.2%) of aggregates. The fresh properties were evaluated through slump, density and air content tests. Hardened properties were investigated using the compressive and flexural strengths, pulse velocity, dynamic elastic modulus, and water absorption tests. The results obtained showed that strapping strap waste fibers significantly improve the mechanical properties of fiber-reinforced concrete and have a behavior similar to that of steel fibers. The optimum rates of strapping strap fibers were 0.4% and 1.2% for compressive and flexural strengths respectively. Compared to polypropylene fibers, the strapping strap fibers were found to be more efficient and led to a gradual increase in flexural strength with an increase in the strapping strap fibers. The results obtained also showed that the increase in strapping strap fiber content gradually increased the water absorption of fiber-reinforced concrete.

Address

[1] LMGHU Laboratory, Department of Civil Engineering, University 20 August 1955, Skikda, Algeria.

[2] Dept. of Civil Engineering and Hydraulic, University 08 May 1945, Guelma, Algeria.

* ***Corresponding author:*** dj_rachid_08@yahoo.fr

Key words

- Strapping straps,
- Fibers,
- Reinforced concrete,
- Properties.

1 INTRODUCTION

Fiber-reinforced concrete (FRC) is a composite material in which fibers are incorporated. Unlike traditional reinforcements, the fibers are distributed throughout the concrete mass. FRC exhibits better flexural and tensile strength (Tiberti et al., 2014; Cuenca et al., 2015) and more ductile behavior (Alabduljabbar et al., 2019; Ghamari et al., 2020). Fibers used in concrete also permit higher impact energy absorption (Chalioris, 2013, Rahmani et al., 2014) and higher dynamic strength

(Deepa Raj et al., 2020; Abid et al., 2020). The fibers used make the concrete suitable for various applications such as offshore and military infrastructures (Abid et al., 2020), airports pavements (Aydin, 2007, Watanabe et al., 2010), bridge decks, channel lining and industrial flooring (Ding et al., 2011; Slater et al., 2012; Abid et al., 2020). The efficiency of adding fibers to a concrete composition depends on the type, geometry, content, and orientation of the fibers (Bentur and Mindess, 1990; Buratti et al., 2011). Several types of fibers are used in FRC technology. Steel and polypropylene fibers are the most commonly used in FRC compositions (Sorelli et al., 2006; Caratelli et al., 2011). FRC containing steel fibers (SF) found their first applications in the 1960s. Polymeric fibers were marketed in the 1970s, glass fibers in the 1980s, and carbon fibers in the 1990s (Abid et al., 2020).

Over the decades, various studies have demonstrated the use of fibers in concrete technology. Aydin (2007) used up 2% of SF in self-compacting concrete (SCC) compositions. He found that SF decreased the workability and increased the compressive and tensile strengths of SCC. Similar results were obtained by Alabduljabbar et al. (2019), who added that SF improved the segregation resistance and mechanical properties of SCC with an optimum rate equal to 2%. With 2% of SF, the compressive strength and splitting strength increased by 13.38% and 91.44% respectively at 90 days. Akcay and Tasdemir (2012) reported that the main factor concerning the ability to flow of SCC containing SF was the geometry of the fibers. Khaloo et al. (2014) found that both the workability and the compressive strength of SCC containing SF decreased, but the splitting tensile and flexural strengths tended to increase. The addition of 2% SF decreased the compressive strength by 18.60% and increased the tensile strength by 28.50%. Iqbal et al. (2015) reported that the flexural and tensile strength of SCC containing SF were significantly improved. They also reported that there was no significant impact of SF on the compressive strength and elastic modulus. Nagarkar et al. (1987) observed that the compressive and flexural strengths of steel fiber-reinforced concrete (SFRC) increased by 13 and 40% when 0.5% of SF were used. Olivito and Zuccarello (2010) reported that the failure mode of FRC considerably changed from fragile to ductile when SF were used. They also reported that the ductility and tenacity of FRC increased when the fiber length and content increased. A similar trend was observed by Tadepalli et al. (2013). Bentur and Mindess (1990) reported that the effect of fibers on the mechanical properties of FRC depended on the load transfer process from the matrix to the fibers and the bridging effect across the cracks. Banthia et al. (1996) reported that concrete containing 0.5% of SF exhibited an increase in fracture energy by 2.4 times. Shah and Naaman (1976) added that the flexural and tensile strengths of FRC containing SF increased by two to three times. De Figueiredo and Ceccato (2015) found that the use of fibers in FRC composition decreased its workability. This decrease was more pronounced when SF were used (Hughes and Fattuhi, 1976; Bayasi and Soroushian, 1992; Guerini et al., 2018). Song and Hwang (2004) reported that the compressive strength of FRC increased by up to 1.5% of SF content. With further additions, the compressive strength tended to decrease. Ma et al. (2013) showed an improvement in compressive strength, splitting tensile strength, and flexural toughness when 2% SF was used. Additionally, they found that the improvement in splitting tensile strength was more pronounced.

On the other hand, Alhozaimy et al. (1996) reported that polypropylene fibers (PPF) had no significant effects on the compressive and flexural strengths of FRC. They also found that PPF significantly affected the flexural toughness. With 0.3% PPF, the flexural toughness and failure impact resistance increased by 387% and 90% respectively. Similar results were found by Song et al. (2005). However, Kakooei et al. (2012) reported that the presence of PPF in a concrete composition improved the compressive strength and electrical resistivity and reduced the permeability and volume variations of FRC with an optimum rate equal to 1.50 kg/m^3. Han et al. (2005) reported that the PPF did not significantly affect the bulk density and air content of FRC. They also reported that PPF slightly increased the compressive strength and significantly improved the spalling strength. Mazaheripour et al. (2011) observed that PPF decreased the workability of SCC, increased the flexural and splitting tensile strengths, and did not affect the compressive strength and elastic modulus. A similar trend was also observed by Yap et al. (2013). Mindess and Vondran (1988) reported that the use of 0.5% PPF led to increasing the bending load by 40% and double the fracture energy. Afroughsabet and Ozbakkaloglu (2015) reported that the improvement in mechanical strength was more pronounced when the SF were used compared to the PPF. They also observed that both the SF and PPF reduced the electrical resistivity of FRC. Similar results were found by Mastali and Dalvand (2017). Guerini et al. (2018) found that the use of fibers in a concrete composition slightly increased the air content. They also showed that PPF adversely affected the air content more than SF.

2 SIGNIFICANCE OF RESEARCH

Ordinary concrete exhibits low tensile strength and poor ductility. To resolve these handicaps, previous studies have broached the effect of fibers such as SF and PPF on the properties of concrete. However, much less is known about the properties and behavior of concrete containing strapping straps waste fiber (SSF). The strapping strap are made of polyethylene terephthalate (PET) and used for both manual and automatic applications to strengthen packaging. After its use, the strapping strap is discarded as waste, thereby causing environmental problems (disposal and aesthetic problems, clogging the waterways). The objective of this study is to investigate the effect of SSF considered as waste on fresh and hardened properties of FRC and compare it with commonly available fibers used in reinforcing concrete. For this purpose, SF, PPF and SSF were used to carry out this experimental investigation. The valorization of SSF in the composition of concrete not only aims to improve some properties of concrete, but also to produce a 'green' concrete. On the other hand, concrete is one of the most used materials in the world because of its high strength, low cost and durability (Afroughsabet and Ozbakkaloglu, 2015; Mazloom and Mirzamohammadi, 2019; Alwesabi et al., 2020). When waste can be used in the composition of concrete, then a large quantity of this waste can be eliminated from the environment.

3 MATERIALS USED

3.1 Cement

Ordinary Portland cement (OPC) Type CEMI 42.5 with a specific gravity of 3.15 g/cm^3 and specific surface of 3600 cm^2/g produced by the Hadjar Elsoud Cement Plant (Eastern Algeria) was used in this experimental work. The chemical properties of OPC are illustrated in Table 1.

Tab. 1 *Chemical properties of OPC*

Chemical properties (%)	OPC
CaO	61.38
Al_2O_3	5.18
Fe_2O_3	3.34
SiO_2	19.97
MgO	0.99
Na2O	0.20
K2O	0.44
Cl-	0.19
SO_3	2.90
Loss in ignition	3.71
C_4AF	10.25
C_3A	8.08
C_3S	58.45
C_2S	13.24

3.2 Aggregates

Coarse aggregate (CA) from natural crushed limestone aggregate was used for all the mixtures. Two types of gravel (G1 and G2) were used with maximal nominal sizes of 16 mm and 25 mm respectively. The specific density of these gravels is 2.65 g/cm^3. Moreover, fine aggregate (FA) from natural crushed limestone sand (CS) with a specific density of 2.61 g/cm^3 and a water absorption of 0.80 % was used. The CS had a maximum particle size of 4.00 mm. The fineness modulus, which was obtained from the sieve analysis, was equal to 2.91. The aggregate properties are illustrated in Table 2.

Tab. 2 *Properties of aggregates*

Properties	FA	CA
Specific density (g/cm^3)	2.61	2.65
Sand equivalent (%)	70	-
Fineness modulus	2.91	-
Methylene blue value	0.50	-
Micro-deval test (%)	-	14.40
Los Angeles test (%)	-	20.10

The particle distributions of FA and CA are presented in Fig 1.

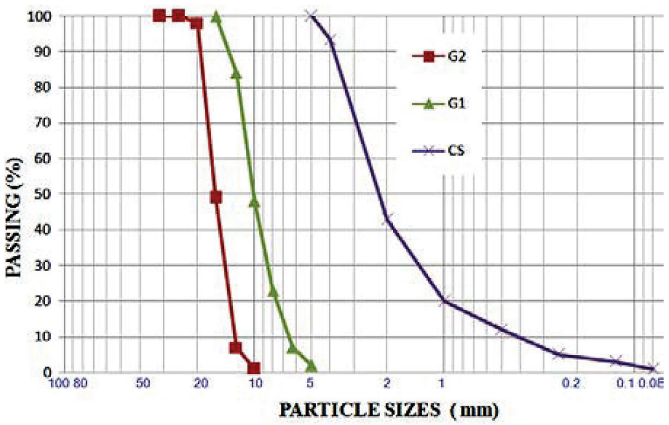

Fig. 1 *Particle size distribution of aggregates used*

3.3 Fibers

SF with a 50 mm length and a diameter of 0.95 mm, PPF with a 12 mm length, and SSF with a 50 mm were used in this study. The SSF were derived from shredding strapping strap waste. The properties of the fibers are provided in Table 3.

Tab. 3 *Properties of fibers*

Properties	SF	PPF	SSF
Length (mm)	50	12	50
Color	Grey	White	Green
Diameter (µm)	95	25	95
Density (g/cm^3)	7.85	0.91	1.27

Fig 2 shows the SSF used for the composition of the FRC mixtures.

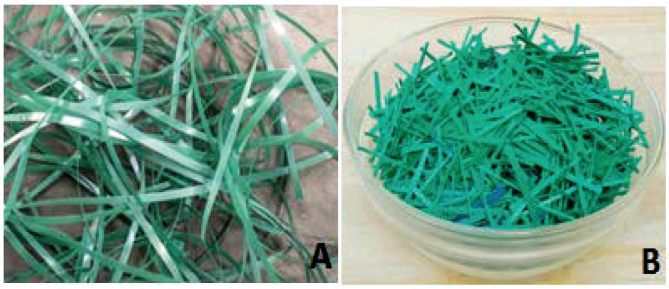

Fig. 2 *SSF used in FRC composition: A) Strapping strap waste before shredding; B) SSF after shredding*

3.4 Admixture

To obtain the desired workability for the control concrete mixture, the superplasticizer (SP) used was Polyflow SR 5400, which is based on polycarboxylate with a brown color, a density of 1.07, and a PH of 5.

4 MIXING PROCEDURE AND TESTING METHODS

The FRC mix proportions are provided in Table 4. The Dreux-Gorisse method was used for the composition of the concrete mixtures. In the table, the SP content is presented in volume and is taken as equal to 0.8% of the total weight of OPC. The dosages of OPC, water and SP are kept constant. SSF, SF and PPF have been introduced into the concrete composition by volumetric substitution (0.4%, 0.8% and 1.2%) of the aggregates.

To ensure a good degree of homogeneity for all the mixtures, the solid constituents were mixed for three minutes. The water and SP were then mixed with the other constituents for three more minutes. The mixture was then introduced and vibrated into standard steel molds according to NF P18-405. Cube samples (150×150×150 mm) were used for the compressive strength, pulse velocity, and water absorption by immersion tests. Prismatic samples (70×70×280 mm) were used for the flexural strength (Fig 3).

Fig. 3 *Flexural strength test*

After 24 hours of molding, the samples were demolded and conserved in water for curing (at 23 °C and 100% relative humidity) until their testing ages. The fresh and hardened properties tests were performed according to the standards mentioned in Table 5. For each test, the results obtained represent the average of three readings.

Tab. 5 *Tests carried out*

Tests	Standards
Workability (Slump test)	NF EN 12350-2
Bulk density	NF EN 12350-6
Air content	NF EN12350-7
Compressive strength	NF EN 12390-3
Flexural strength	NF EN 12390-5
Pulse velocity	NF EN 12504-4
Water absorption	NBN B15-215

5 DISCUSSION OF RESULTS

5.1 Workability

The results of the workability test are shown in Fig 4 for specimens containing different fiber types and volume fractions. As can be seen, the workability of FRC decreases with the increasing fiber content regardless of the type of fibers. It can also be seen that the PPF significantly affects the work-ability values of FRC compared to SF and SSF. SF and SSF. The workability decreases from 210 to 80 mm when the PPF content increases from 0 to 1.2%. While the workability decreases by 10 and 35 mm only when 1.2% of SF and SSF are used respectively. It can also be seen that with 0.4% of SF and SSF, the decrease in workability remains insignificant. The decrease in the workability of FRC was also observed

Tab. 4 *Composition of FRC mixtures for 1 m³*

	G2 (kg/m³)	G1 (kg/m³)	FA (kg/m³)	OPC (kg/m³)	SP (L/m³)	Water (L/m³)	SF (kg/m³)	PPF (kg/m³)	SSF (kg/m³)
C0	306	612	695.08	350	3	147	0	0	0
SFRC0.4	303.10	606.30	688.14	350	3	147	24	0	0
SFRC0.8	299.99	599.91	681.17	350	3	147	48	0	0
SFRC1.2	296.89	593.79	674.23	350	3	147	72	0	0
PFRC0.4	303.10	606.30	688.14	350	3	147	0	7.28	0
PFRC0.8	299.99	599.91	681.17	350	3	147	0	14.56	0
PFRC1.2	296.89	593.79	674.23	350	3	147	0	21.84	0
SSFRC0.4	303.10	606.30	688.14	350	3	147	0	0	5.08
SSFRC0.8	299.99	599.91	681.17	350	3	147	0	0	10.18
SSFRC1.2	296.89	593.79	674.23	350	3	147	0	0	15.26

by (Abhishek et al., 2015; Anandaraj et al., 2019; Awoyera et al., 2021), and was attributed to the fact that the fibers have a low water-wetting ability and therefore increase the friction between the concrete constituents and make the concrete flow more difficult. Ali et al. (2020) recommended the use of plasticizers to compensate for the negative effect of the fibers on FRC workability. De Figueiredo and Ceccato (2015) also recommended the reduction of the maximum size of the aggregate used and increasing the amount of mortar in the concrete composition.

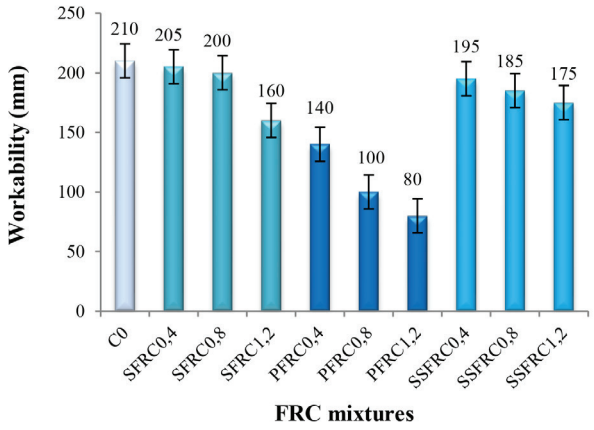

Fig. 4 *Workability of FRC mixtures*

5.2 Bulk density

Fig 5 shows the bulk density values of the FRC mixtures. Unlike SF, the increase in PPF and SSF contents gradually decreased the density of FRC. This decrease is more pronounced when PPF are used. The bulk density decreased by 4.14% and 8.29% when 1.2% of SSF and PPF are used respectively, while with the same content of SF, the bulk density of FRC increased by 1.02%. The bulk density of concrete mainly depends on the density of its components (Han et al., 2005). PPF and SSF have lower densities than the other components, and the addition of these fibers leads to decreasing the bulk density of the concrete. On the other hand, SF have higher density than those of the other constituents; therefore, FRC containing SF have higher bulk densities.

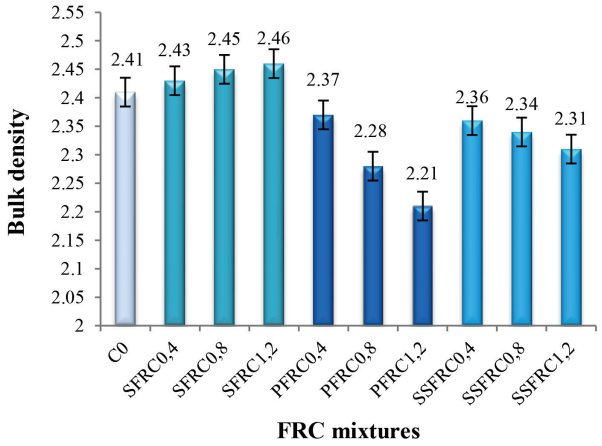

Fig. 5 *Bulk density of FRC mixtures*

5.3 Air content

The air content values are illustrated in Fig 6. As shown, increasing the fiber content in FRC composition leads to an increase in the air content values. It can also be seen that SF significantly increases the air content values compared to PPF and SSF. The air content increases by 69.69% when 1.2% of SF is used, while the air content increases by 27.27% and 15.15% only when the same content of PPF and SSF is used. A similar trend was observed by (Hughes and Fattuhi, 1976; Guerini et al., 2018), who explained this increase by the reduction in the workability of FRC, which promotes the trapping of air bubbles inside the concrete. It should be noted that with 0.4% of fibers, the increase in air content does not exceed 10.60%.

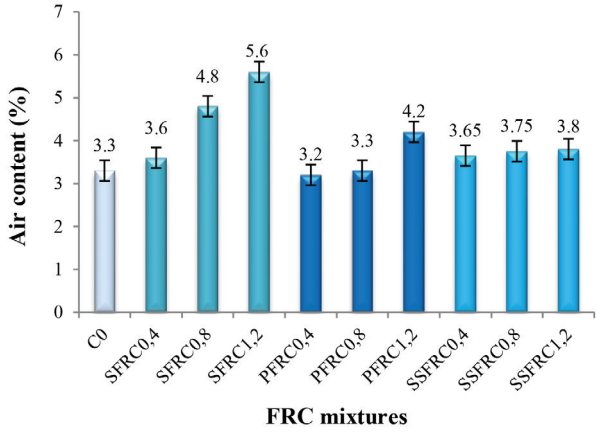

Fig. 6 *Air content of FRC mixtures*

5.4 Compressive strength

The variations in the compressive strength of FRC containing different types and volumes of fibers at 7, 28 and 56 days are illustrated in Fig 7. Except for the concrete containing the PPF, all the concrete mixtures show an improvement in compressive strength with an optimal rate of 0.4%. With further additions, the compressive strength tends to decrease. The FRC containing 0.4% of SSF exhibits an improvement in compressive strength by 16.02, 5.23, and 4.07% at 7, 28, and 56 days respectively, while the FRC containing 0.4% of SF shows the maximum increase in compressive strength at 56 days by 7.56%. The improvement in the compressive strength of FRC was shown in several studies (Yan et al., 1999; Afroughsabet and Ozbakkaloglu, 2015; Sabri and Walid, 2020), which explained it by the fact that the fibers have an ability to slow the expansion of cracks, change their direction and delay the rate growth in cracks. The increase in the compressive strength of FRC containing SF is also attributed to the higher mechanical properties of SF compared to those of SSF and PPF (Afroughsabet and Ozbakkaloglu, 2015). However, all FRC containing PPF exhibits a gradual reduction in compressive strength. This reduction is more pronounced when the PPF rate exceeds 0.8%. With 1.2% of PPF, the compressive strength drops by 22.51, 34.93, and 44.71% at 7, 28, and 56 days. The reduction in the compressive strength of FRC containing SF and PPF was shown by (Alhozaimy et al.,1996;

Iqbal et al., 2015; Khaloo et al., 2014; Marthong, 2019), who attributed this reduction to the decrease in workability and the increase in air content with increasing the fiber content in FRC composition. Additionally, when the fiber content exceeds the optimal rate, more initial voids and a lack of adhesion between the cement paste and fibers will be created and lead to a decrease in the compressive strength.

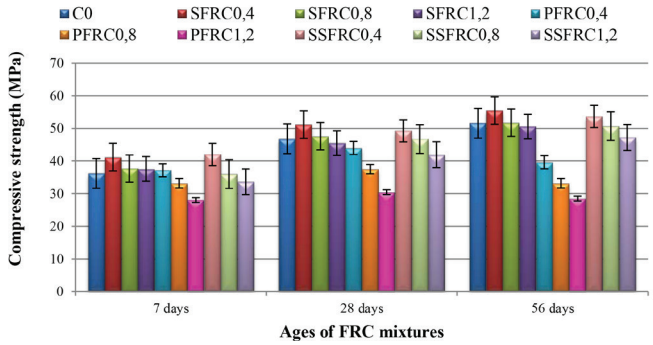

Fig. 7 *Compressive strength of FRC mixtures*

5.5 Ultrasonic pulse velocity

Fig 8 displays the ultrasonic pulse velocity of the FRC mixtures at 28 days. The control mixtures had an ultrasonic pulse velocity of 4.84 km/s, whereas the FRC containing 0.4% of SSF and SF had 4.93 and 4.88 km/s with an increase of 1.86 and 0.83% respectively. With a further addition of SSF and SF above 0.4%, the ultrasonic pulse velocity tends to gradually decrease. It can also be seen that the incorporation of PPF negatively affects the ultrasonic pulse velocity values. The FRC containing 0.4 and 0.8% of PPF showed a decrease in ultrasonic pulse velocity by 3.72 and 7.85% respectively. The decrease in the ultrasonic pulse velocity values is explained by the increase in the internal porosity of the FRC containing a higher fiber content. It should be noted that according to ASTM C597, which considers concrete to be of a very good quality when the ultrasonic pulse velocity is higher than 4.50 km/s, all the FRC mixtures are classified to have a very good quality.

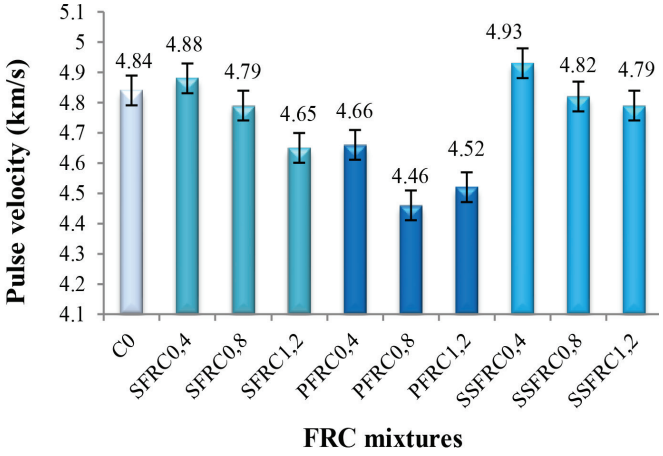

Fig. 8 *Ultrasonic pulse velocity of FRC mixtures*

5.6 Flexural strength

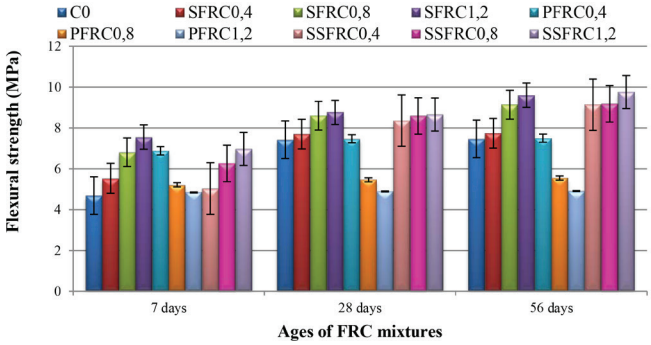

Fig. 9 *Flexural strength of FRC mixtures*

The results of the flexural strength test are illustrated in Fig 9. The addition of SF and SSF in the FRC composition has a beneficial effect on the flexural strength. The flexural strength of the FRC gradually increases with an increase in the SF and SSF fiber content. At 56 days, the flexural strength increased from 7.46 to 9.60 and 9.76 MPa when 1.2% of SF and SSF were used respectively, i.e., an increase of 28.68 and 30.83% respectively. For FRC containing PPF, the improvement in the flexural strength is more pronounced at an early age and is shown when the PPF rate does not exceed 0.4%. With 0.4% of PPF, the flexural strength increases by 46.69, 0.54, and 0.4% at 7, 28, and 56 days respectively. The enhancement of concrete's flexural strength was attributed to the arresting and bridging effects played by the fibers on the crack (Khaloo et al., 2014; Li et al., 2018; Marthong, 2019; Sabri and Walid, 2020). When the fiber content exceeds the optimal rate, the workability decreases and more initial voids and weak interfaces are produced, thereby causing flexural strength reductions (Song et al., 2005; Huang et al., 2016). Afroughsabet and Ozbakkaloglu (2015) also reported that the improvement in the flexural strength of FRC containing SF is attributed to the higher tensile strength and elastic modulus of SF.

5.8 Water absorption

The water absorption represents the permeable pore volumes and their connectivity inside the concrete. It constitutes a major factor that affects the durability (Nagarkar et al., 1987). The water absorption values of FRC mixtures are presented in Fig 10. As shown, all the FRC mixtures have water absorption values higher than that of the control concrete. The water absorption gradually increases with increasing the fiber content regardless of the type of fibers. The water absorption of the control concrete was 2.60%, while the maximum water absorption of the FRC was 3.80, 4.46, and 3.80% for the FRC containing SF, PPF, and SSF respectively. It can also be shown that the FRC containing 1.2% of PPF exhibits the maximum increase in the water absorption value by 71.53% compared to that of the control concrete. The increase in the water absorption values is attributed to a) the increase in the air content of FRC in the fresh state, which increases the air content in the hardened state b) the reduction of the workability of FRC, in

particular, FRC containing PPF, which promotes the creation of voids inside the FRC and facilitates the water penetration into FRC (Hughes and Fattuhi, 1976; Guerini et al., 2018). According to (CEB-FIP, 1989), concrete having a water absorption of less than 3%, between 3 to 5%, and higher than 5% can be classified as good, average, and poor quality. According to this classification, the FRC containing 0.4% of SSF exhibits good quality, whereas all the other FRC mixtures have an average quality.

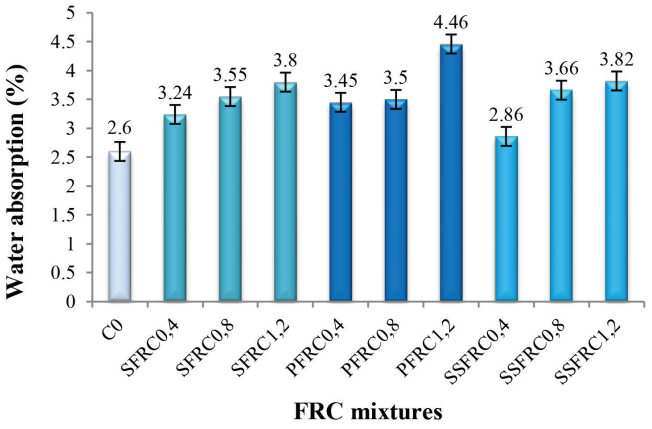

Fig. 10 *Water absorption of FRC mixtures*

5.9 Dynamic elastic modulus

The dynamic elastic modulus of the concrete mixtures was evaluated using the following equation (Uysal and Yilmaz, 2011):

$$E = 10^5 \times V^2 \times \left(\frac{\Delta}{g}\right) \quad (1)$$

E is the dynamic elastic modulus (GPa); V is the ultrasonic pulse velocity (m/s); Δ is the bulk density of the concrete (kg/m^3); and g is the gravity acceleration (m/s^2).

As with the compressive strength, the dynamic elastic modulus increases with 0.4% of SF and SSF. With further additions, the dynamic elastic modulus tends to decrease (Fig 11). With 0.4% of fibers, the dynamic elastic modulus increases by 2.50 and 1.61% for SF and SSF respectively. This improvement is mainly due to the increase in the compressive strength values of FRC containing 0.4% SF and SSF and also to the higher mechanical properties of SF (Afroughsabet and Ozbakkaloglu , 2015) . However, all the FRC mixtures containing PPF exhibit a gradual decrease in the dynamic elastic modulus. A maximum decrease of 20.02% was shown with 1.2% of PPF. The reduction in the dynamic elastic modulus values is explained by the increase in the FRC porosity and the drop in the compressive strength with the increase in the fiber content.

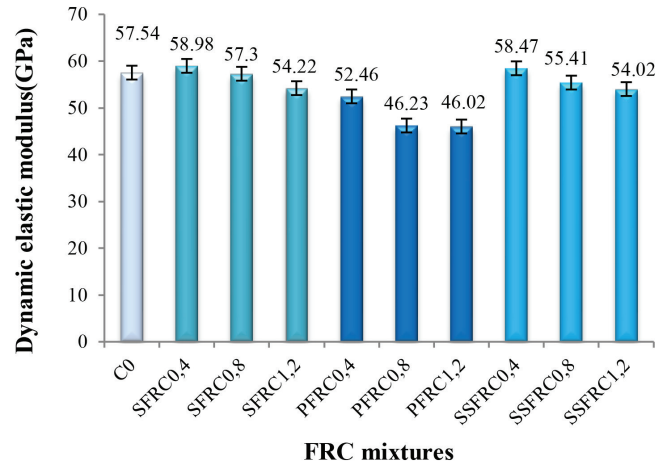

Fig. 11 *Dynamic elastic modulus of FRC mixtures*

6 CONCLUSIONS

In this study, the fresh and hardened properties of FRC containing SSF were investigated and compared with those of FRC containing SF and PF. Through this experimental work, the following conclusions can be drawn:

- As for all types of fibers, the incorporation of SSF in an FRC composition decreases the workability values. This decrease does not significantly alter the ability of the concrete to flow as long as the SSF content does not exceed 1.2%. The workability of FRC was found to be reduced by 16.66% when the SSF content reached 1.2%.
- Due to the lower density of SSF, the inclusion of SSF in an FRC composition reduces the bulk density values and makes FRC less dense than ordinary vibrated concrete and FRC containing SF. The introduction of SSF led to a gradual decrease in the bulk density, which reached 2.31 with 1.2% of SSF.
- The addition of SSF in the FRC composition increases the porosity and causes a gradual increase in water absorption in the hardened state and the air content in the fresh state.
- The FRC containing SSF has a behavior similar to that of the FRC containing SF. In fact, the addition of SSF in the FRC composition improves the mechanical properties of FRC with an optimal rate of 0.4% for the compressive strength and dynamic elastic modulus and 1.2% for flexural strength. This improvement is due to the arresting and bridging effects that the SSF plays on cracks.

In addition to the ecological interest coming from the valorization of SSF waste, this study showed promise as to the technical interest in of the introduction of this waste in the composition of FRC. From the results obtained, SSF can be considered as fibers having a mechanical behavior similar to SF. Future research should be established to study the durability and behavior of FRC containing SSF towards different chemical attacks. Also, it could be very interesting to study the ductility and energy absorption capacity for beams made of FRC containing SSF.

REFERENCES

Abhishek, T.S. – Vijaya, S. – Swamy, B.S. (2015) *Study of fresh and mechanical properties of coconut fiber reinforced self compacting concrete enhanced with steel fibers*. International Journal of Engineering Research & Technology, 4 (6), pp. 911–914.

Abid, S.R. – Abdul-Hussein, M.L. – Ayoob, N.S. – Ali, S.H. – Kadhum, A.L. (2020) *Repeated drop-weight impact tests on self-compacting concrete reinforced with micro-steel fiber*. Heliyon, 6, e03198, https://doi.org/10.1016/j.heliyon.2020.e03198

Afroughsabet, V. – Ozbakkaloglu, T. (2015) *Mechanical and durability properties of high-strength concrete containing steel and polypropylene fibers*. Construction and Building Materials, 94, pp. 73-82. http://dx.doi.org/10.1016/j.conbuildmat.2015.06.051

Akcay, B. – Tasdemir, M.A. (2012) *Mechanical behaviour and fibre dispersion of hybrid steel fibre reinforced self-compacting concrete*. Constrution and Building Materials, 28, pp. 287-293. doi:10.1016/j.conbuildmat.2011.08.044

Alabduljabbar, H. – Alyousef, R. – Alrshoudi, F. – Alaskar, A. – Fathi, A. – Mohamed, A.M. (2019) *Mechanical effect of steel fiber on the cement replacement materials of self-compacting concrete. Fibers, 7 (4), 36. https://doi.org/10.3390/fib7040036*

Alhozaimy, A. M. – Soroushiad, P. – Mirza, F. (1996) *Mechanical properties of polypropylene fiber reinforced concrete and the effects of pozzolanic materials*. Cement and Concrete Composites, 18, pp. 85-92.

Ali, S. – Kumar, H. – Rizvi, S.H. – Raza, M.S. – Ansari, J.K. (2020) *Effects of steel fibres on fresh and hardened properties of cement concrete*. CEER, 30 (3), pp. 186-198. DOI: 10.2478/ceer-2020-0039

Alwesabi, A.E. – Abu Bakar, B.H. – Alshaikh, I.M.H. – Akil, H.M. (2020) *Impact resistance of plain and rubberized concrete containing steel and polypropylene hybrid fiber*. Materials Today, 101640. https://doi.org/10.1016/j.mtcomm.2020.101640

Anandaraj, S. – Rooby, J. – Awoyera, P.O. – Gobinath, R. (2019) *Structural distress in glass fibre-reinforced concrete under loading and exposure to aggressive environments*. Constrution and Building Materials, 197, pp. 862–870. https://doi.org/10.1016/j.conbuildmat.2018.06.090

Awoyera, P.O. – Olalusi, O, B. – Iweriebo, N. (2021) *Physical, strength, and microscale properties of plastic fiber-reinforced concrete containing fine ceramics particles*. Materialia, 15, 100970. https://doi.org/10.1016/j.mtla.2020.100970

Aydin, A.C. (2007) *Self compactability of high volume hybrid fiber reinforced concrete*. Construction and Building Materials, 21, pp. 1149-1154. doi:10.1016/j.conbuildmat.2006.11.017

Banthia, N. – Mindess, S. – Trottier, J.F. (1996) *Impact resistance of steel fiber reinforced concrete*. ACI Materials Journal, 93, pp. 472–479.

Bayasi, M.Z. – Soroushian, P. (1992) *Effect of steel fiber reinforcement on fresh mix properties of concrete*. ACI Materials Journal, 89, pp. 369–374.

Belgium Standard NBN B15-215, T*esting hardened concrete, Absorption of water by immersion*

Bentur, A. – Mindess, S. (1990) *Fiber Reinforced Cementitious Composites*. Taylor and Francis Group, London and New York.

Buratti, N. – Mazzotti, C. – Savoia, M. (2011) *Post-cracking behaviour of steel and macrosynthetic fibre-reinforced concretes*. Construction and Building Materials, 25, pp. 2713–2722. https://doi.org/10.1016/j.conbuildmat.2010.12.022

Caratelli, A. – Meda, A. – Rinaldi, Z. – Romualdi, P. (2011) *Structural behavior of precast tunnel segments in fiber reinforced concrete*. Tunnelling and Underground Space Technology, 26, pp. 284–291. https://doi.org/10.1016/j.tust.2010.10.003

CEB-FIP, (1989) *Diagnosis and assessment of concrete structures-state of art report.* CEB Bulletin, Euro-International Concrete Committee (Comité Euro-International du Béton), 83–85.

Chalioris, C.E. (2013) *Steel fibrous RC beams subjected to cyclic deformations under predominant shear*. Engineering Structures, 49, pp. 104–118. https://doi.org/10.1016/j.engstruct.2012.10.010

Cuenca, E. – Echegaray-Oviedo, J. – Serna, P. (2015) *Influence of concrete matrix and type of fiber on the shear behavior of self-compacting fiber reinforced concrete beams*. Composites Part B: Engineering, 75, pp. 135-147. http://dx.doi.org/10.1016/j.compositesb.2015.01.037

Deepa Raj, S. – Ganesan, N. – Abraham, R. (2020) *Role of fibers on the performance of geopolymer concrete exterior beam column joints*. Advances in Concrete Constructions, 9(2). pp. 115-123. https://doi.org/10.12989/acc.2020.9.2.115

De Figueiredo, A.D. – Ceccato, M.R. (2015) *Workability analysis of steel fiber reinforced concrete using slump and Ve-Be test*. Materials Researchs, 18, pp. 1284–1290. https://doi.org/10.1590/1516-1439.022915

Ding, Y. – You, Z. – Jalali, S. (2011) *The composite effect of steel fibres and stirrups on the shear behaviour of beams using self-consolidating concrete*. Engineering Structures, 33,pp. 107–117.

European Standard NF EN 12350-2, *Test for fresh concrete - Part 2: Slump test*

European Standard NF EN 12350-6, *Test for fresh concrete - Part 6: Bulk density test*

European Standard NF EN12350-7, *Test for fresh concrete - Part 7: Air content test*

European Standard NF EN 12390-3, *Test for hardened concrete - Part 3: Compressive strength test*

European Standard NF EN 12390-5, *Test for hardened concrete - Part 5: Flexural strength test*

European Standard NF EN 12504-4, *Test for hardened concrete - Part 4: Pulse velocity test*

Ghamari, A. – Kurdi, J. – Shemirani, A.B. – Haeri, H. (2020) *Experimental investigating the properties of fiber reinforced concrete by combining different fibers*. Computers and Concrete, 25(6), pp. 509-516. https://doi.org/10.12989/cac.2020.25.6.509

Guerini, V. – Conforti, A. – Plizzari, G. – Kawashima, S. (2018) *Influence of Steel and Macro-Synthetic Fibers on Concrete Properties*. Fibers, 6 (3), 47. doi:10.3390/fib6030047

Han,C.G. – Hwang, Y.S. – Yang, S.H. – Gowripalan, N. (2005) *Performance of spalling resistance of high performance concrete with polypropylene fiber contents and lateral confinement*. Cement and Concrete Research, 35, pp. 1747– 1753. doi:10.1016/j.cemconres.2004.11.013

Huang, L. – Chi, Y. – Xu, L. – Chen, P. – Zhang, A. (2016) *Local bond performance of rebar embedded in steel polypropylene hybrid fiber reinforced concrete under monotonic and cyclic loading*. Construction and Building Materials, 103, pp. 77–92. https://doi.org/10.1016/j.conbuildmat.2015.11.040

Hughes, B. P. – Fattuhi, N.I.(1976) *The workability of steel-fibre-reinforced concrete*. Magazine of Concrete Research, 28 (96), pp. 157-161.

Iqbal, S. – Ali, A. – Holschemacher, K. – Bier, T.A. (2015) *Mechanical properties of steel fiber reinforced high strength lightweight self-compacting concrete (SHLSCC)*. Construction and Building Materials, 98, pp. 325–333. http://dx.doi.org/10.1016/j.conbuildmat.2015.08.112

Kakooei, S. – Akil,H.M. – Jamshidi, M. – Rouhi, J. (2012) *The effects of polypropylene fibers on the properties of reinforced concrete structures.* Construction and Building Materials, 27, pp. 73–77. doi:10.1016/j.conbuildmat.2011.08.015

Khaloo, A. – Raisi, E.M. – Hosseini, P. – Tahsiri, H. (2014) *Mechanical performance of self-compacting concrete reinforced with steel fibers*. Construction and Building Materials, 51, pp. 179-186. http://dx.doi.org/10.1016/j.conbuildmat.2013.10.054

Li, B. – Chi, Y. – Xu, L. – Shi, Y. – Li, C. (2018) *Experimental investigation on the flexural behavior of steel-polypropylene hybrid fiber reinforced concrete*. Construction and Building Materials, 191, pp. 80-94. https://doi.org/10.1016/j.conbuildmat.2018.09.202

Ma, H.L. – Cui, C. – Li, X. – Hu, S.L. (2013) *Study on mechanical properties of steel fiber reinforced autoclaved lightweight shell-aggregate concrete*. Materials and Design. 52, pp. 565–571. http://dx.doi.org/10.1016/j.matdes.2013.05.086

Marthong, C. (2019) *Effect of waste cement bag fibers on the mech*anical strength of concrete. Advanced Materials Research, 8(2), pp. 103-115. https://doi.org/10.12989/amr.2019.8.2.103

Mastali, M. – Dalvand, A. (2017) *Fresh and Hardened Properties of Self-Compacting Concrete Reinforced with Hybrid Recycled Steel-Polypropylene Fiber*. Journal of Materials in Civil Engineering, 29(6), 04017012. doi: 10.1061/(ASCE)MT.1943-5533.0001851

Mazaheripour, H. – Ghanbarpour, S. – Mirmoradi, S.H. – Hosseinpour, I. (2011) *The effect of polypropylene fibers on the properties of fresh and hardened lightweight self-compacting concrete*. Construction and Building Materials, 25, pp. 351-358. doi:10.1016/j.conbuildmat.2010.06.018

Mazloom, M. – Mirzamohammadi, S. (2019) *Thermal effects on the mechanical properties of cement mortars reinforced with aramid, glass, basalt and polypropylene fibers*. Advanced Materials Research, 8(2), pp. 137-154. https://doi.org/10.12989/amr.2019.8.2.137

Mindess, S. – Vondran, G. (1988) *Properties of concrete reinforced with fibrillated polypropylene fibers under impact loading*. Cement and Concrete Research,18, pp. 109–115.

Nagarkar, P.K. – Tambe S.K. – Pazare, D.G. (1987) *Study of Fibre Reinforced Concrete.* Proceedings of International Symposium of Fibre Reinforced Concrete, Madras, India, December.

Olivito, R.S. – Zuccarello, F.A. (2010) *An experimental study on the tensile strength of steel fiber reinforced concrete*. Composites Part B: Engineering, 41, pp. 246-255. doi:10.1016/j.compositesb.2009.12.003

Rahmani, T. – Kiani, B. – Shekarchi, M. – Safari, A. (2014) *Statistical and experimental analysis on the behavior of fiber reinforced concretes subjected to drop weight test*. Construction and Building Materials, 37, pp. 360-369. http://dx.doi.org/10.1016/j.conbuildmat.2012.07.068

Sabri, F- Walid, M. (2020) *Evaluate the effect of steel, polypropylene and recycled plastic fibers on concrete properties*. Advances in Concrete Construction, 10(4), pp. 319-332. https://doi.org/10.12989/acc.2020.10.4.319

Shah, S.P. – Naaman, A.E. (1976) *Mechanical properties of glass and steel fibre reinforced mortar*. ACI Journal, 73(1), pp. 50–53.

Slater, E. – Moni, M. – Alam, M.S. (2012) *Predicting the shear strength of steel fiber reinforced concrete beams*. Construction and Building Materials, 26, pp. 423–436. https://doi.org/10.1016/j.conbuildmat.2011.06.042

Song, P.S. – Hwang, S. (2004) *Mechanical properties of high-strength steel fiber-reinforced concrete*. Construction and Building Materials, 18, 669-673. doi:10.1016/j.conbuildmat.2004.04.027

Song, P.S. – Hwang, S. – Sheu, B.C. (2005) *Strength properties of nylon- and polypropylene-fiber-reinforced concretes*. Cement and Concrete Research, 35, pp. 1546– 1550. doi:10.1016/j.cemconres.2004.06.033

Sorelli, L.G. – Meda, A. – Plizzari, G.A. (2006) *Steel fiber concrete slabs on ground: A structural matter*. ACI Structural Journal, 103, pp. 551–558. Doi:10.14359/16431

Tadepalli, P.R. – Hsu, T.T.C. – Mo, Y.L. (2013) *Mechanical properties of steel fibre concrete*. Magazine of Concrete Research, 65(8), 462-474. http://dx.doi.org/10.1680/macr.12.00077

Tiberti, G. – Minelli, F. – Plizzari, G.A. – Vecchio, F.J. (2014) *Influence of concrete strength on crack development in SFRC members*. Cement and Concrete Composites, 45, pp. 176-185. https://doi.org/10.1016/j.cemconcomp.2013.10.004

Uysal, M. – Yilmaz, K.(2011) *Effect of mineral admixtures on properties of self-compacting concrete*. Cement and Concrete Composites, 25, 4112-4120. doi:10.1016/j.cemconcomp.04.005

Watanabe, K. – Kimura, T. – Niwa, J. (2010) *Synergetic effect of steel fibers and shear reinforcing bars on the shear-resistance mechanisms of RC linear members*. Construction and Building Materials, 24, pp. 2369–2375. https://doi.org/10.1016/j.conbuildmat.2010.05.009

Yan, H. – Sun, W. – Chen, H. (1999) *The effect of silica fume and steel fiber on the dynamic mechanical performance of high-strength concrete*. Cement and Concrete Research, 29 (3), pp. 423–426. https://doi.org/10.1016/S0008-8846(98)00235-X

Yap, S. – Alengaram, U. – Jumaat, M.Z. (2013) *Enhancement of mechanical properties in polypropylene and nylon–fibre reinforced oil palm shell concrete*. Materials and Design, 49, pp. 1034–1041. https://doi.org/10.1016/j.matdes.2013.02.070

sciendo

Slovak Journal of Civil Engineering

Vol. 32, 2024, No. 1, 10 – 17
DOI: 10.2478/sjce-2024-0002

NON-LINEAR BEHAVIOR OF DOUBLE-LAYERED GRIDS

Tarek, METROUNI[1*], Nadia, KHELLAF[2], Khelifa, KEBICHE [2]

Abstract

This study presents a numerical approach to an analysis of the mechanical behavior of double-layered tensegrity grids. We present a comparative study on the behavior of tensegrity grids through geometric nonlinear analysis (GNA) and combined nonlinear analysis (CNLA) (geometric and material), considering the possible effect of evolution in the elasto-plastic domain of the cable elements. The effect of the relaxation of cable on the amplification of the displacement of these grids was taken into account. The updated Lagrangian formulation, which modifies the Newton-Raphson iterative scheme with incremental loading, was adopted. We have developed a numerical computational model specific to tensegrity structures that simulates the geometric and material nonlinear behavior. The reliability of the calculation tool developed has been validated. Additionally, the results of the application of the numerical model on a grid, which was generated based on demi-cuboctahedral tensegrity cells, are presented.

Address

[1] Dept. of Civil Engineering, Research Unit on Emerging Materials (RUEM), Ferhat Abbas University of Setif 1, Setif 19000, Algeria

[2] Dept. of Civil Engineering, Civil Engineering Research Laboratory of Setif (LRGCS), Ferhat Abbas University of Setif 1, Setif 19000, Algeria

* ***Corresponding author:*** tarek.metrouni@univ-setif.dz

Key words

- Tensegrity,
- Double layer grids,
- Geometrical nonlinearity,
- Material nonlinearity,
- Relaxation.

1 INTRODUCTION

Double-layer tensegrity grids are spatial and tensile reticulated systems containing two parallel arrays of tension members forming top and bottom chords, the nodes of which are connected using vertical and/or inclined web members under compression and tension (Gómez-Jáuregui, 2012; Kaveh and Ghazaan, 2018). These lightweight constructive systems are frequently employed to cover large-span areas. Although Snelson (2013) was the inventor of these structures, they were first studied from a technical point of view in 1975 by Fuller, who presented most of their geometric properties (Fuller, 1982). In recent years, methods to analyze these structures have been developed, and regular and systematic research has been carried out to provide a theoretical basis for the analysis and design of these structures. Studies by (Pellegrino,1990; Pellegrino and Caladin,1986; Motro,1992; Motro et al., 1990), and Hanaor (1991) play an important role in understanding the mechanical behavior of tensile systems. In terms of behavioral studies, methods have been developed to describe the behavior of tensegrity systems in the context of large displacements (Zhang, 2013; Foroughi and Lee, 2014; Nuhoglu and Korkmaz, 2011; Feng and Guo, 2017).

Obara and Tomasik (2020) have conducted a comprehensive study focusing on a qualitative analysis of plate-like tensegrity structures constructed with modified Quartex modules. The main goal of their research was to evaluate and understand the unique properties of tensegrities, which enable control over static and dynamic parameters.

Bel Hadj Ali et al. (2021) conducted a static analysis of tensioned structures with sliding cables. They integrated friction induced by cable sliding into finite element and dynamic relaxation analysis methods using a linear complementarity approach. The study demonstrated the significance of considering sliding-induced friction through various examples, by there revealing its significant effects on the mechanical be-

havior of the structures without impacting computation time.

Kan et al (2021) introduced an innovative approach for the mechanical analysis of clustered cable structures. Their multibody-based method, which utilizes generalized coordinates to describe the configurations of rigid bodies, departs from traditional finite element formulations; the results demonstrated that friction between the cables and bars significantly affects the mechanical behavior of a clustered cable.

The dynamic behavior of double-layer tensegrity systems has been analyzed using the time integration algorithms developed (Greco and Ferreira, 2013). Ben Kehla et al. (2020) studied the dynamic response of a pentagonal ring-based tensegrity bridge, while considering the sudden cable break selected.

A finite element formulation, based on the co-rotational approach by (Feng and Guo, 2017), was developed for geometrically nonlinear elastoplastic analyses of a classical and clustered tensegrity. Murakami (2001) derived the basic equations for static and dynamic analyses of tensegrity structures with large deformations in Eulerian and Lagrangian formulations.

Tran and Lee (2011) developed a similar study; however, instead of the incremental load method for nonlinearities, they used total and updated Lagrangian formulations to establish the equations and a variant of the Newton-Raphson method to solve them, which was similar to the approach used by (Murakami, 2001). Bel Hadj Ali and Smith (2010) developed a modified dynamic relaxation method to simulate the static response of a clustered tensegrity beam and a quasi-static deployment of a clustered tensegrity tower.

Logzit and Kebiche (2022) developed a fatigue analysis model for Geiger-type cable domes subjected to in-phase biaxial loads. They used multiaxial fatigue criteria based on the critical plane approach and formulated a specific fatigue criterion for cable domes. This model makes it possible to predict the lifetime of these structures as a function of the response in a monotonic loading mode.

Shekastehband et al. (2012) studied the progressive collapse behavior under static loading on a tensegrity grid of (3x3x0.7). Logzit and Kebiche (2020) adopted a model based on the verification of iterative stability for a tensegrity cable dome using a geometric nonlinearity analysis.

As to the static studies carried out on these structures, we have focused on (Kebiche et al., 1999; Khellaf and Kebiche, 2013), who developed a calculation code treating geometric and combined nonlinear analyses (geometric and material) of the elements based on tensegrity modules. The code was applied to linear structures (columns or beams), where the focus was on the effect of local instabilities (slackening and plasticization of cables) on the global behavior of the structure. In addition, (Khellaf and Kebiche, 2014) studied the geometric and material nonlinear mechanical behavior of reconstructed tensile systems of hexagon-based rings by adopting the arc length driving technique imposed.

These studies aim to establish a strategy for the safe dimensioning of these innovative construction systems intended for different applications, such as covering large spaces. The present study, which is a part of these investigations, focuses on an analysis of the non-linear behavior of double sheet tensile grids. This study presents a novel numerical approach for analyzing the mechanical behavior of double-layered tensegrity grids. With their complex geometric and material nonlinear behavior, tensegrity structures have been thoroughly investigated through a comparative study utilizing both geometric nonlinear analysis (GNA) and combined nonlinear analysis (CNLA). The study accounts for the evolution in the elastoplastic domain of cable elements and for their relaxation on the displacement amplification of tensegrity grids. The motivation for this research was driven by the need to better understand tensegrity grid behavior and overcome the challenges posed by their unique nonlinear characteristics. It aims to develop and validate a specialized numerical computational model that associates material and geometric nonlinearity and demonstrates interest numerically in various tensegrity grid configurations. The interest of this model, once validated, makes possible the extension of a study to deal with more complex problems such as the phenomena of cable fatigue or buckling struts.

2 ANALYSIS METHOD

The tangential stiffness matrix of a tensile structure is derived from its equilibrium, compatibility, and ratio constitution. A numerical model has been developed to simulate and highlight the amplification of the displacements of the tensegrity plates, known for their great flexibility, considering the large deformations (plastification) and large displacements (slackening) of the cables.

2.1 Nonlinear resolution method

The nonlinear behavior of tensegrity grids (load-displacement), which is due to their great flexibility, can be amplified by the geometric or material nonlinearity of their constitutive elements (struts or cables).

The resolution method used is iteratively incremental. For an increment, a balance correction is introduced, using an iterative process. The Newton-Raphson method, which is based on a tangent stiffness matrix re-estimated at each iteration in order to reach equilibrium, is used.

The use of this method has the advantage of ensuring fairly rapid convergence with reliable results; its major drawback arises in the time spent updating the tangent stiffness matrix at each iteration.

The following figure shows an example of a non-linear process using the incremental method. The values used in the non-linear calculations are displayed:

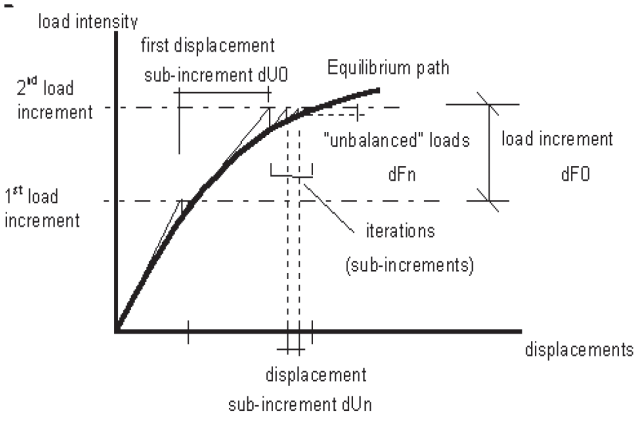

Fig. 1 *Nonlinear calculation process.*

2.1.1 Modeling of the grid elements (cables, struts)

The cable is an element that works only in traction (palisade). Owing to its non-linearity, an analysis of a structure containing cable elements requires the use of calculation algorithms defined for an analysis integrating geometric non-linearity.

The following equations were used (Khellaf and Kebiche, 2013):

$$\sigma = E_T.\varepsilon \ \ if \ \ \sigma < \sigma_y. \tag{1}$$

$$\sigma = f(\varepsilon) \ \ if \ \ \ \sigma \geq \sigma_y \tag{2}$$

where σ is the axial engineering stress; is the stress limiting the elastic behavior of the material; E_T is the elastic stiffness modulus of the material ('Young's modulus'), is the axial engineering strain; and represents the one-dimensional flow law (Khellaf and Kebiche,2014; Abedi and Shekastehband,2008). The work-hardening rule will be defined later.

As to **struts**, which are assumed to have a perfect elastic plastic behavior, the constitutive law is:

$$f(\varepsilon) = \sigma_y \tag{3}$$

3 VALIDATIONS OF THE CALCULATION MODEL

3.1 Validation using numerical results from ANSYS

In this section, we validate our simulation results by comparing the simulation results obtained using commercial software (ANSYS V20.2) with the results of the calculation model developed.

Geometric and mechanical characteristics of the grid

All the geometric and mechanical characteristics as well as the values of the initial self-stressing applied to the elements composing the structure (bars and cables) of the grid are specified in Table 1.

The nodal loads were applied as shown in Fig. 2. For practical realization conditions, we assumed that all the peripheral nodes on the bottom sheet of the grid were fixed according to the X, Y, and Z directions (Fig.2).

The vertical displacements (Z_{mean}) of the central nodes (6,7,10, and 11) as a function of the increasing load applied are plotted in Fig. 3. As shown in Fig. 2, the results were compared with those obtained using the ANSYSV20.2 software and were found to be in perfect agreement.

3.2 Validation using experimental results

To confirm the reliability of the simulation model developed, a comparison with the data obtained from experimental tests carried out on a double-layer tensegrity grid was performed.

Geometric specifications of the grid tested

An experimental study was conducted by (Shekastehband et al., 2012) on a tensile grid consisting of nine modules in a demi-cuboctahedron (3 m × 3 m × 0.7 m). The module and the assembled structure are shown in Fig.5, and the material properties are presented in Table 2. The grid was composed of 132 elements, including 36 compressed struts (steel tubes) and 96 tensioned cables (steel), which were connected through the nodes, as shown in Fig. 5.

Tab. 1 *Geometric and Mechanical Characteristics of Cables and Struts Elements*

Group	Component Type	Initial yield stress σy (daN/cm²)	E (daN/cm²)	A (cm²)	Critical buckling stress (daN/cm²)	Initial tension (daN)
1	struts	2350	2000000	3.25	1116.9	-1469.64
2	Base cables	4800	400000	0.28	-	600.0
3	Upper and braced cables	4800	400000	0.28	-	848.52
4	common cables	4800	400000	0.56	-	848.52

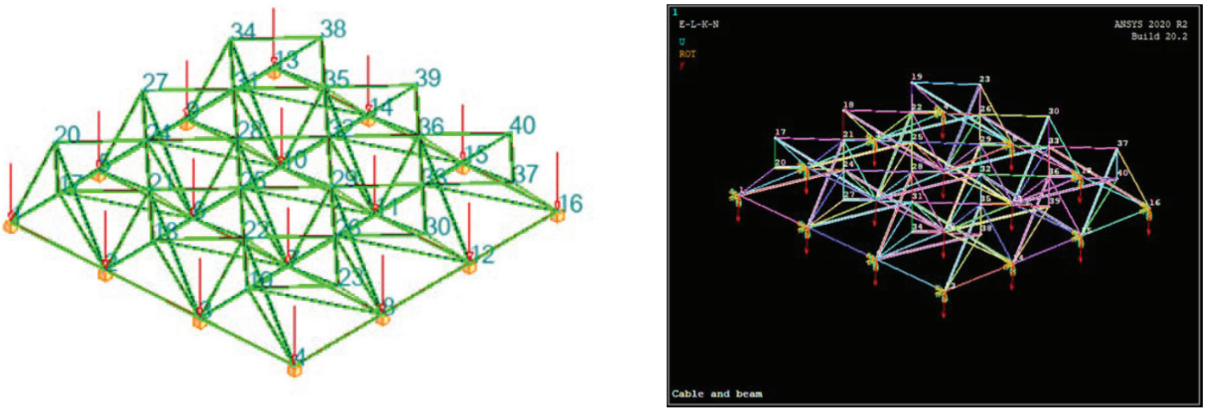

Fig. 2 *Geometry and loading of the 9-module double-layer grid*

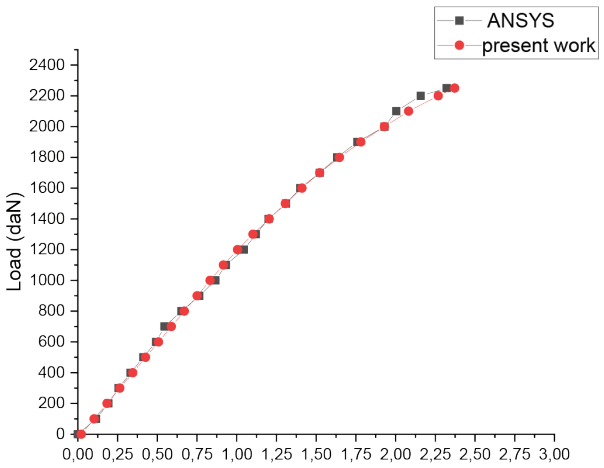

Fig. 3 *Average z displacements of nodes (6,7,10,11) in the Z direction.*

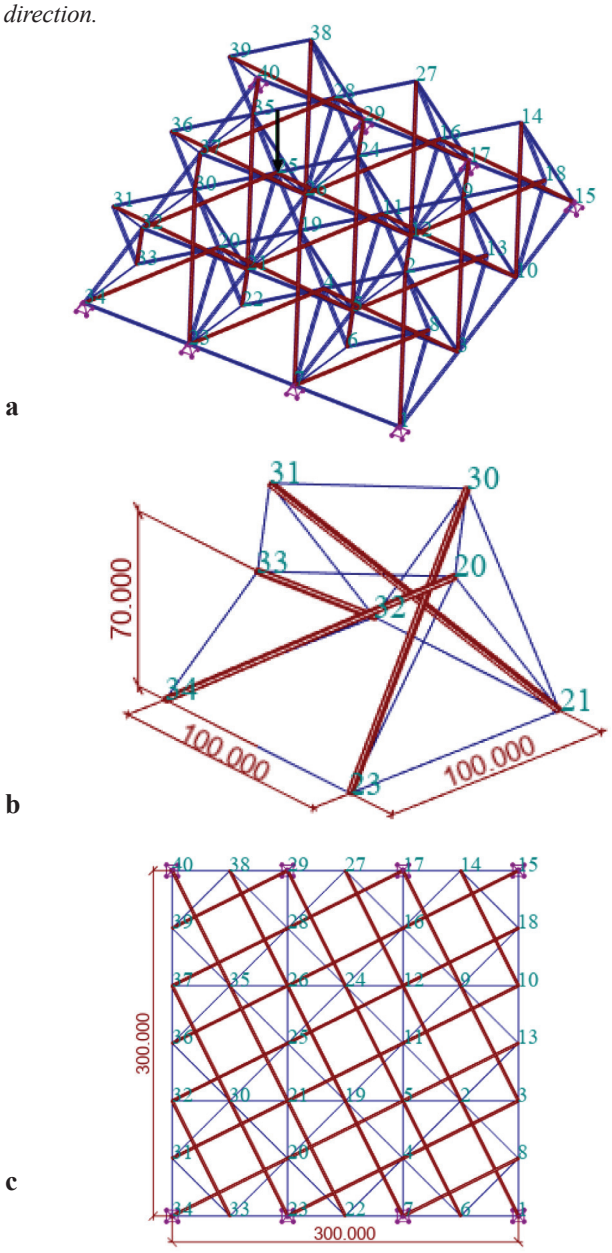

Fig. 5 *Regularly arranged tensegrity grid composed of 36 spacers and 96 cables. a) Perspective view. b) The quadruplex module .c) Plan view.*

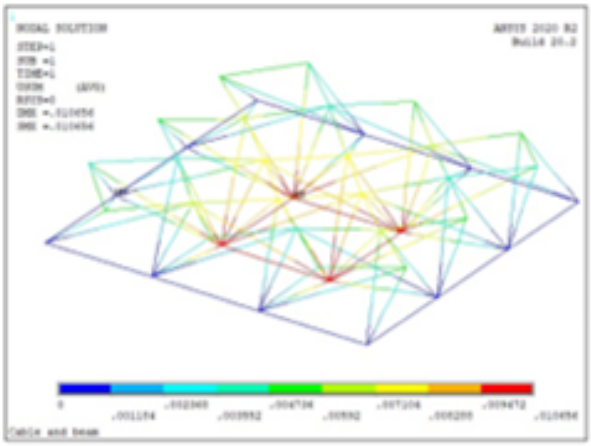

Fig. 4 *Displacement of nodes obtained by Ansys under load 1200 daN.*

The load was applied on Node 25 (Fig.5). Nodes 1, 7, 23, 34, 15, 17, 29, and 40, were blocked along the X and Y directions, as shown in Fig. 5. The experimental investigation was carried out under a load control; there was therefore no control on the displacements.

Tab. 2 *Mechanical properties of elements used in the tensegrity model*

Element		Initial yield stress [daN/cm^2]	Elasticity module [daN/cm^2]	Element Section [cm^2]
Struts		3450	2040000	2.07240
cables	Type 1	13500	1250000	0.50240
	Type 2	13800	1370000	0.50240
	Type 3	16400	1930000	0.50240

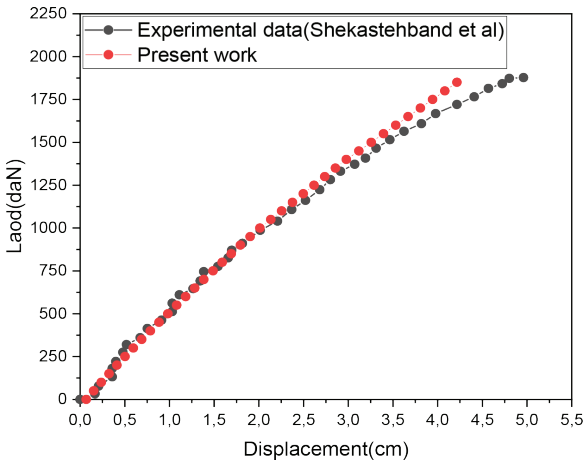

Fig. 6 *Behavior curve at node 25*

Figure 6 shows the experimental and numerical load-deformation responses of the tensile grid at Node 25. The Z-displacements of Node 25 are plotted as a function of the increasing load applied.

Discussion

It can be seen from Fig. 6 that the experimental and numerical values obtained from the present model are very close. The table below shows the maximum divergence (%) between the two calculation methods:

Load P(daN)	1850
$Z_{\text{numerical value}}$(cm)	4.21589
$Z_{\text{experimental value}}$(cm)	4.64265
Difference	10%

This small difference may be owing to some imperfections, such as the application of initial tensions at the cables and possible looseness at the connection nodes in the experimental execution.

4 APPLICATION

4.1 4x4 Tensegrity grid

This section describes the application of a proposed code for the analysis of a 4 x 4 double-ply quadruplex tensile grid under a bending load (Fig. 7). The results are presented as the evolution of the displacements of the stressed nodes as a function of the external loads. The Elastic and elastoplastic deformations are studied as a function of the external loads.

4.1.1 *Geometric and material specifications of the grid*

Fig. 7 shows a square (4 x 4) plane tension grid generated based on 16 quadruplex cells. It is composed of 65 nodes, 64 struts, and 168 cables. The nodal coordinate, mechanical characteristics, and self-tension vector of the grid are given in Tables 4, 5, and 6, respectively.

Tab. 3 *Nodal coordinates (cm) of a quadruplex*

Node	X[cm]	Y[cm]	Z[cm]
1	0	0	0
2	0	100	0
3	0	50	50
4	50	0	50
5	50	100	50
6	100	0	0
7	100	100	0
8	100	50	50

For practical purposes, we assumed that all the peripheral nodes on the bottom sheet of the grid were fixed along the X, Y, and Z directions. The vertical load 'F' was applied as shown in Fig. 8.

Fig. 9 shows the load-displacement curves for the NEA and NEPA of the tensile grid (4x4) (Fig.8). The displacements were measured in cm at Node 13 in the center of the plate. The effect of the cable slack was taken into account for both types of analyses. The purpose of this study was to highlight the impact of the material nonlinear behavior of cables on the amplification of the maximum displacements of the structure.

It should be noted from Fig. 9 that the behavior of the grid in **NEA** presents a barely detectable non-linearity. The divergence between the two curves starts from the load at F=850daN. When this load reaches its maximum value at F=1300 daN, the difference between the displacements corresponding to the two types of analysis is approximately 1 cm.

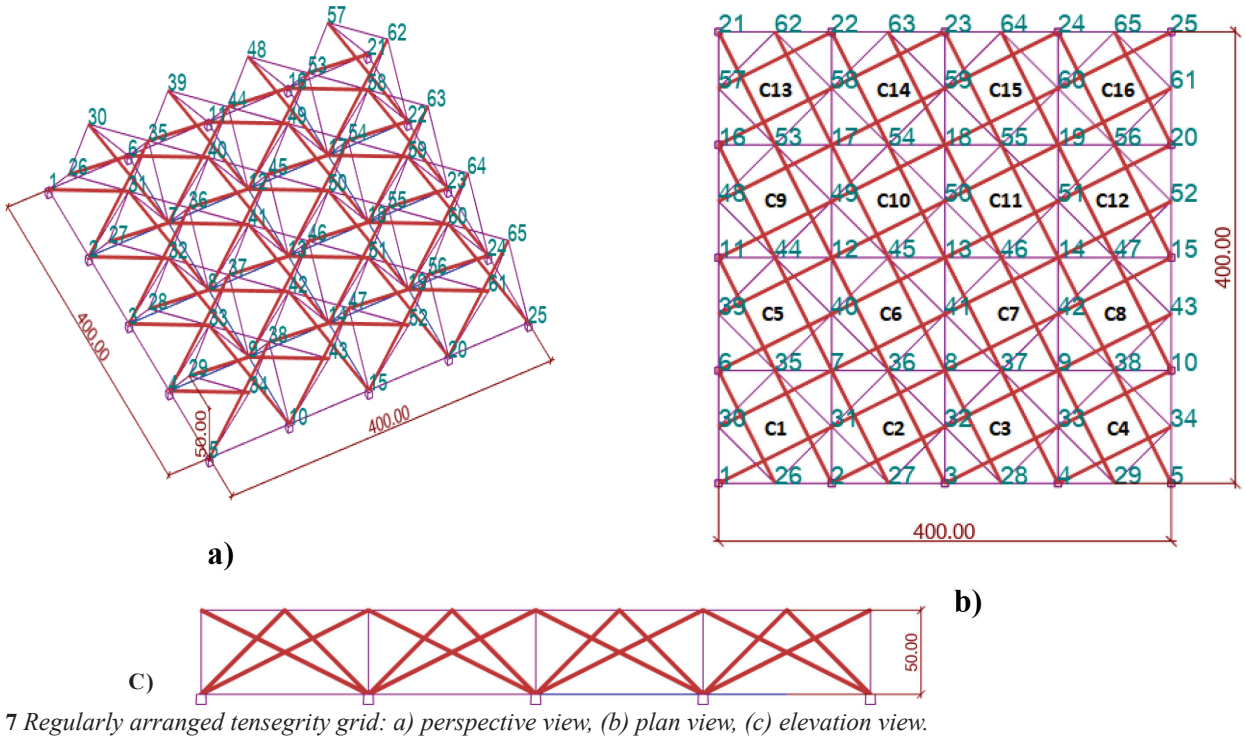

Fig. 7 *Regularly arranged tensegrity grid: a) perspective view, (b) plan view, (c) elevation view.*

Tab. 4. *Geometric and mechanical characteristics of cable and bar elements*

Group	Component Type	Initial yield stress σy (daN/cm²)	E (daN/cm²)	A (cm²)	(daN/cm²)	Critical buckling stress (daN/cm²)
1	Struts	2350	2,000,000	3.25	2350	1116.9
2	Base cables	4800	400,000	0.28	4800	-
3	Upper and braced cables	4800	400,000	0.28	4800	-

Tab. 5 *Initial Self-Stress Values Used in (daN)*

Nature of Element	S1(daN)
struts	-1469.64
Base cables	600.0
Upper and braced cables	848.52
Ordinary cables	848.52

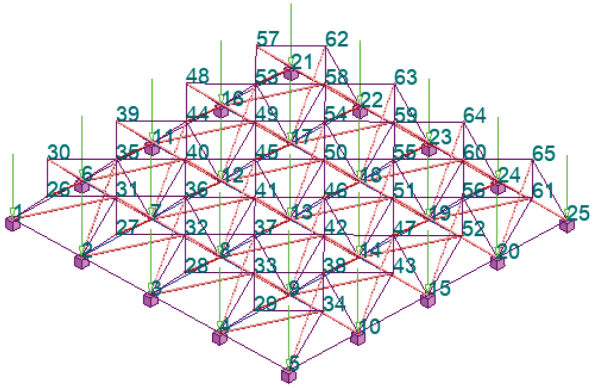

Fig. 8 *Geometry and loading of the tensegrity grid.*

Therefore, it can be concluded that the effect of the cable plasticization on the increase in grid flexibility is certain.

Figures 10 and 11 show a comparison between the variations in the internal tension in Cables 137 and 77 of the grid for **NEA and NEPA.** The two figures show that there is a difference in the internal forces. For **NEP**A, Cable 137 relaxed at F= 850 daN, while for **NEA** the same cable relaxed at F=900daN (Fig. 10).

In figures 12, 13, 14, and 15 and Table 6, we have attempted to present the NEPA of the response of the grid during bend-ing, considering the evolution of the internal forces in the ca-ble and bar elements of Modules C_1 (corner module) and C_2 (central module).

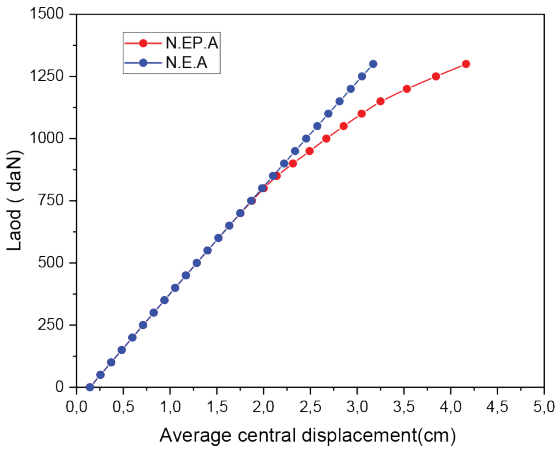

Fig. 9 *Comparison of elastic and elastoplastic behavior under flexion.*

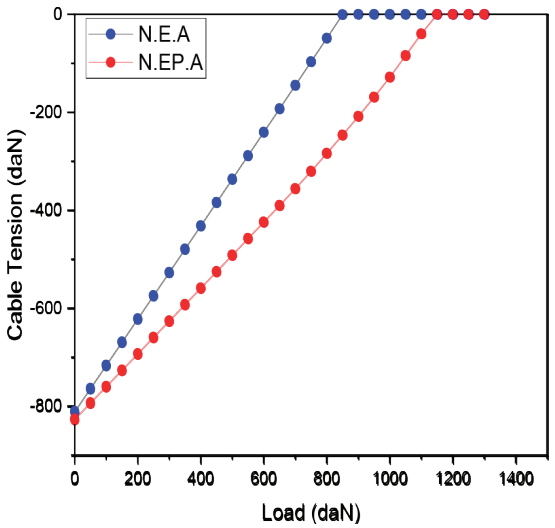

Fig. 10 *Tension in Cable 137.*

Tab. 6 *Analysis of the variation of internal forces in the struts and cables at the center and corners of the 4X4 grid based on the demi-cuboctahedron.*

	Corner area (Module C1)	Central zone (Module C6)
Cable states	Only one cable was released (slack cable). Most of the cables in the module displayed an almost constant development of tension. Cable K, whose tension increased visibly and approached the breaking point, was a spacer cable (Fig.10).	Three cables were released (top and bottom sheet cable). The release of Cables D, G, and F caused a rapid increase in tension in the other cables of the module. Cable B approached breaking tension (T=2100daN) (Fig.11).
Status of the struts	In Fig.12, we can clearly see the effect of slackening the cables (F=1150daN) on the increase in compression in struts C and D	The compression in the four bars showed an increasing beam influenced mainly by the loss of Cables D, G, and F through relaxation under F=1150daN.
	which shows that the internal forces are too far from the value of critical buckling force equal to 3629.925 daN, in both NEA and NEPA.	

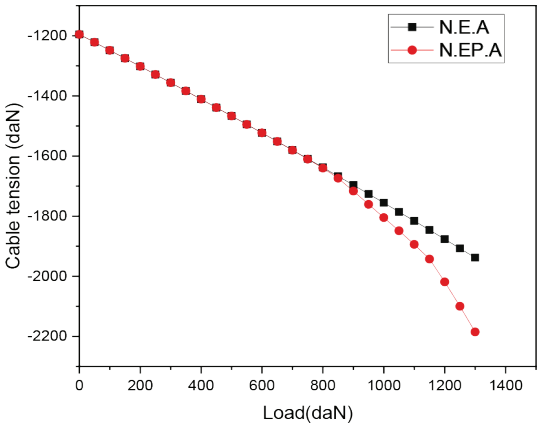

Fig. 11 *Tension in Cable 77.*

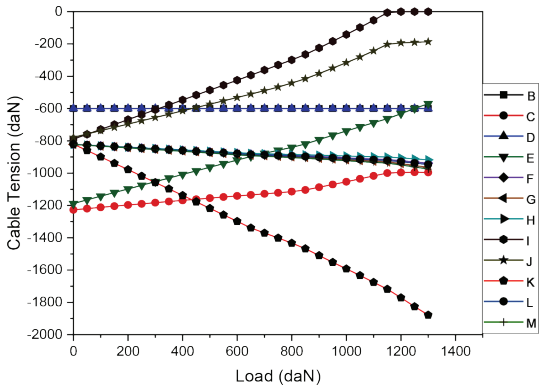

Fig. 12 *Variation of Tension Forces in Cable Elements of Cell C1 Considering an N.EP. A*

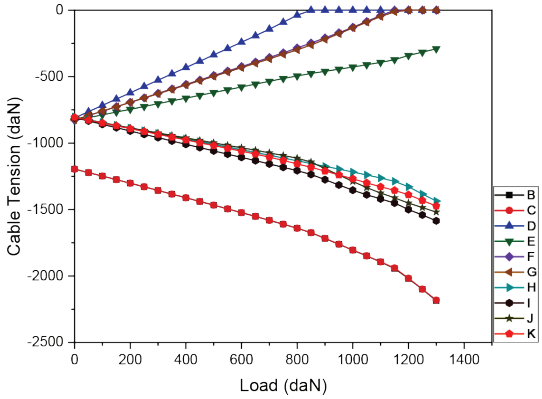

Fig. 13 *Variation of Tension Forces in Cable Elements of Cell C6 Considering an N.EP. A*

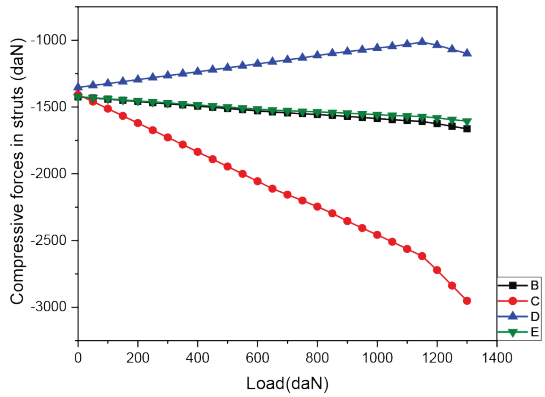

Fig. 14. *Variation of compression in the struts of cell C1 considering an N.EP.A*

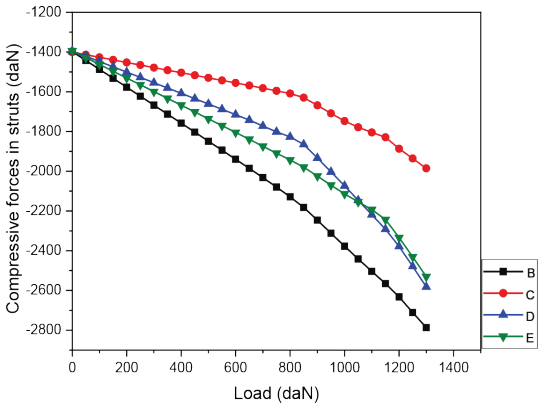

Fig. 15. *Variation of compression in the struts of cell C6 considering an N.EP.A*

5 CONCLUSION

A numerical method implemented in a computer program has been proposed for an inelastic analysis of a large deflection of tensegrity systems. The Newton-Raphson iterative solution method in the updated Lagrangian formulation was adopted, taking into account the geometric and material nonlinearities. Two types of analyses, i.e.s NEA and NEPA, are proposed.

The results obtained were validated experimentally and through the ANSYS commercial software; the validity and efficiency of the proposed method have been illustrated using numerical examples. The elastic and elasto-plastic responses of a double-layer quadruplex tensegrity grid were studied using the proposed formulation.

The proposed program plots the responses of the quadruplex double-layer tensegrity grid of the quadruplex module under external loads. From the numerical results obtained, the following conclusions can be drawn:

– The proposed program can accurately predict the geometric and material nonlinear behavior of tensegrity systems using both updated Lagrangian descriptions.

–The inclusion of a geometric non-linear analysis has generated a decrease in internal stresses. This suggests an optimization in the dimensioning of the structural elements (weight optimization).

–The results of the code we developed, which is specific to tensegrity structures in geometric and material nonlinearities, are in agreement with the results obtained from the commercial ANSYS software and the experimental work by Shekastehband et al. (2013).

REFERENCES

Abedi, K. – Shekastehband, B. (2008) *Static stability behavior of plane double-layer tensegrity structures*. Int. J. Space Struct. 23, 89–102 (2008)

Ansys, ANSYS Mechanical APDL Basic Analysis Guide. Release 15.0, ANSYS, Inc., Southpointe, 275 Technology Drive, Canonsburg, PA,USA 153

Bel Hadj Ali, N. – Ziyun, Y. – Peng, H. J. – Rhode-Barbarigos, L. (2021) *On static analysis of tensile structures with sliding cables: The frictional sliding case*. Eng. Comput. 37 (2): 14291442. https://doi.org/10.1007/s00366-019-00893-z.

Bel Hadj Ali, N. – Smith, I.F.C. (2010) *Dynamic behavior and vibration control of a tensegrity structure*. Int J Solids Struct 2010; 47:1285-96.

Ben Kahla, N. – Ouni, M. – Ali, N. – Khan, R. (2020) *Nonlinear dynamic response and stability analysis of a tensegrity bridge to selected cable rupture*. Latin Am. J. Solid. Struct. 17.

Faroughi, S. – Lee, J. (2014) *Geometrical Non-linear Analysis of Tensegrity Based on a Co-Rotational Method*. Adv. Struct. Eng. 2014, 17, 41–51.

Feng, X. – Guo, S. (2017) *Geometrical nonlinear elasto-plastic analysis of tensegrity systems via the co-rotational method*. Mech Res Commun. 2017;79:32-42.

Fuller, R. B. (1982) *Synergetics: explorations in the geometry of thinking*. Estate of R. Buckminster Fuller, 1982. doi: 10.2307/3103256.

Gómez-Jáuregui, V. (2012) *Mallas tensegríticas de doble capa y manipulaciones de Rot- Umbela*. Inf. Const. 64 (527) : 331-344. DOI:10.3989/ic.11.053

Greco, M. – Ferreira,I.P. (2013) *A classical time integration method applied for solution of nonlinear equations of a double-layer tensegrity*. J. Brazilian Society Mecha. Scienc. Engin. 35 (2013) 41- 50

Hanaor, A. **(1991)** *Double-Layer Tensegrity Grids: Static Load Response*. Part II: Experimental Study. J. Struct. Eng. 1991, 117, 1675–1684.

Kan, Z. – Song, N. – Peng, H. – Chen, B. – Song, X. (2021) *A comprehensive framework for multibody system analysis with clustered cables: examples of tensegrity structures*. International Journal of Solids and Structures 210, 289–309.

Kaveh, A. – Ghazaan, M. I. (2018) *Optimal Design of Double-Layer Grids*. Meta-heuristic Algorithms for Optimal Design of Real-Size Structures, Cham: Springer International Publishing, 2018, p. 65-83. doi: 10.1007/978-3-319-78780-0_5.

Kebiche, K. – Kazi-Aoual, M. – Motro, R. (1999) *Geometrical nonlinear analysis of tensegrity systems*. Eng Struct 1999;21(9): 864–76.

Khellaf, N. – Kebiche, K. (2013) *Nonlinear Analysis of Hexagon-Based Tensegrity Ring: Effect of Slackened and Yielded Cables.* KSCE Journal of Civil Engineering, Vol. 17, No. 6, 2013, pp. 1371–1382. https://doi.org/10.1007/s12205-013-0079-5

Khellaf, N. – Kebiche, K. (2014) *Geometric and Material Nonlinear Analysis of Square-Based Tensegrity Ring Structures*. Arab. J. Sci. Eng. 2014, 39, 5979–5989, doi:10.1007/s13369-014-1196-2.

Logzit, N. – Kebiche, K. (2020) *Numerical Model for High Relative Capacity of Tensegrity Domes*. Civ Eng Dimension 2020;22(1):29–36

Logzit, N. – Kebiche, K. (2021) *Biaxial fatigue analysis model under non-proportional phase loading of tensegrity cable domes*. Eng Struct.2021. DOI: 10.1016/j.engstruct.2021.112791

Motro, R.(1990) *Systèmes de tenségrité à double nappe et double courbure: étude infographique et construction de maquette*. Ministère de l'Equipement et du Logement, Direction de l'Architecture et de l'Urbanisme, B.R.A., 1990 France.

Motro, R. (1992) *Tensegrity Systems: The State of the Art*. In : International Journal of Space Structures, H. Nooshin & Z. S. Makowski Editors, Special Issue on Tensegrity Systems, Vol. 7, No. 2, 1992, pp 75-84

Murakami, H. (2001) *Static and dynamic analyses of tensegrity structures*. Part 1. Non-linear equations of motion. Int. J. Solids Struct. 2001, 38, 3599–3613

Nuhoglu, A. – Korkmaz, K.A. (2011) *A practical approach for nonlinear analysis of tensegrity systems*. Eng Comput 27(4):337–345

Obara, P. – Tomasik, J. (2020) *Parametric analysis of tensegrity plate-like structures: Part 1 - qualitative analysis*. Applied Sciences 10: 7042

Pellegrino, S. – Calladine, C. R. (1986) *Matrix analysis of statically and kinematically indeterminate frameworks*. Int. J. Solids Struct., 22(4), pp. 409-428.

Pellegrino, S. (1990) *Analysis of prestressed mechanisms*. Int J Solids Struct 26(12):1329–1350. https://doi.org/10.1016/0020-7683(90) 90082-7

Shekastehband, B. – Abedi, K. – Dianat, N. – Chenaghlou, M.R. (2012) *Experimental and numerical studies on the collapse behavior of tensegrity systems considering cable rupture and strut collapse with snap-through.* Int J Nonlinear Mech 2012; 47:751-68.

Snelson, K. (2013*) Kenneth Snelson, Art and Ideas*. Kenneth Snelson, Marlborough Gallery, NY, USA. 2013.

Tran, H. – Lee, J. (2011) *Geometric and Material Nonlinear Analysis of Tensegrity Structures*, Acta Mechanica Sinica, Vol. 27, No. 6, 2011, pp. 938–949. https://doi.org/10.1007/s10409-011-0520-2.

Zhang, A. (2013) *Numerical method for simulating nonlinear mechanical responses of tensegrity structures under large deformations*. J Appl Mech 2013;80:61

sciendo

Slovak Journal of Civil Engineering

Vol. 32, 2024, No. 1, 18 – 28
DOI: 10.2478/sjce-2024-0003

A SIMPLIFIED APPROACH FOR THE EVALUATION OF THE NON-VISUAL POTENTIAL OF DAYLIGHT IN SIDE-LIT ROOMS

Tomáš JOSAI[1], Jozef HRAŠKA[1*], Tomáš BACIGÁL[2]

Abstract

This article reports on the development, validation, workflow and implementation of a simplified method for evaluating the non-visual (melanopic) potential of daylight in typical side-lit rooms. The method is suitable for climatic areas with a dominant occurrence of cloudy skies. The non-visual daylight evaluation tool is based on a modified average daylight factor method. A simplified daylighting model improves the calculation of the vertical daylight factor and the passage of daylight through a vertical lighting opening. The proposed calculation method makes it possible to determine the illuminance of a vertical plane in the interior. The method is based on the uniform sky and the external diffuse horizontal illuminance at the location of interest. The outputs of the tool can also be used to quickly estimate visual levels of daylight. The article also proposes a classification of the availability of melanopic daylight in side-lit rooms, which is based on the outputs of the proposed calculation method.

Address

[1] Dept. of Building Construction, Slovak University of Technology, Bratislava, Slovakia

[2] Dept. of Mathematics and Descriptive Geometry, Slovak University of Technology, Bratislava, Slovakia

[*] ***Corresponding author:*** jozef.hraska@stuba.sk

Key words

- Daylighting,
- Non-visual potential,
- Evaluation tool,
- Circadian light,
- Healthy lighting.

1 INTRODUCTION

The availability of daylight in buildings and the built environment significantly affects the quality of life (Boyce, 2010; Aries et al., 2015). Landmark discoveries in the chronobiological research of novel blue light-sensitive photoreceptors in the human eye at the turn of the millennium (Provencio, 2000; Brainard et al., 2001; Berson et al., 2002) confirm the earlier empirical observation that light has non-visual effects that are involved in the regulation of several fundamental biological functions of the body; it also affects mood, reduces fatigue and stress, and increases work productivity (Pyeritz et al., 2019; Nagare et al., 2021). The basic reason for these effects is the fact that the production and oscillations of many hormones and enzymes are directly related to the alternation of night and day and to the spectrum and intensity of natural light. Recent research shows that non-visual responses are not only dependent on the blue component of light, but non-visual effects depend on the interaction of information from multiple photoreceptors in the human eye, while their processing depends on the spectral composition of light, its intensity, duration, time of exposure within a day and year, as well as other influences (Gooley et al., 2012; Schlangen and Price, 2021; Lucas et al., 2022).

There is currently a general consensus that light stimulates both visual and non-visual systems in the human body. The main practical questions for architects, lighting engineers, and other professionals are how to incorporate new medical knowledge about the non-visual effects of light into the everyday practice of designing buildings and their interiors. In response to these new challenges, research has been conducted, particularly in the field of artificial lighting, which has brought, among other things, several new color-based methods for assessing "circadian lighting" (Rea et al., 2010; CIE S 026/E, 2018; IWBI, 2022). Several metrics have also been proposed to guarantee "healthy" lighting in buildings. Using multi-spec-

tral simulation software (Inanici, M. & ZGF Architects, 2015; Solemma&Alertness, 2018), many studies have been conducted that analyze photopic and melanopic ocular light exposure in cases of daylight, artificial, and combined lighting (e.g., Amundadottir et al., 2017; Acosta et al., 2019; Innanici et al., 2015; Saiedlue et al., 2019; Pierson et al., 2023).

The spatial distribution of daylight in both exterior and interior spaces, as well as its spectral composition, is constantly changing over time (Diakite-Kortlever and Knnop, 2021; Ezpeleta et al., 2021). Detailed simulations of "vertical circadian daylighting" over the course of a year indicate difficulties with a criteria-based evaluation of the data calculated. The movement of people and their behavior in space can only be predicted to a limited extent. The amount of daylight entering the eyes of users of indoor spaces with lateral daylighting depends to a large extent on the direction of their glance. When someone is looking towards the window, vertical daylight illuminance is several times higher than when looking at a wall. If the window is equipped with a shading device, which is usually the case, its brightness changes, depending on the type of shading device and the way it is used. The illuminance on the eyes of office workers from computer screens can be higher than from windows, especially in the deeper parts of rooms. The results of detailed simulations of "circadian" light environments in buildings are significantly dependent on the evaluation scenario, are complex, and difficult to interpret.

This article focuses on the global and practical assessment of circadian (melanopic) daylight availability in side-lit rooms. The assessment is based on the melanopic average daylight factor method and on the availability of local exterior diffuse daylight. The simplified assessment method proposed allows for a clear assessment of the impact of various geometric urban and architectural parameters and the optical properties of materials and building surfaces on the level of visual and non-visual (melanopic) side daylighting of buildings in the early stages of their design.

2 SIMPLIFIED CALCULATION METHOD OF THE AVAILABILITY OF NON-VISUAL DAYLIGHT IN SIDE-LIT ROOMS

After World War II, building regulations gradually changed, moving from a prescriptive approach based on past experience to performance-based building regulations and building design. The amount of daylight in individual interior spaces was assessed in many countries using the daylight factor (DF) at a point in the room; subsequently, in several countries, the average daylight factor (ADF) of a reference plane in the room began to be used (Crisp and Littlefair, 1984). DF is the ratio of the horizontal indoor to horizontal outdoor daylight illumination under standardized overcast sky conditions. DF is a performance indicator that allows for the specification of the impact of the size and configuration of a room, the size and distribution of transparent parts of a building envelope and their light transmittances, and the reflectances of all surfaces on the distribution of diffuse daylight in side-lit rooms. DF provided architects, designers, and stakeholders with information on compliance with daylight legislation in the early stages of building design. In the early 21st century, the climate-based daylight modeling (CBDM) method began to be widely used for the design and assessment of daylight in buildings (Mardaljevic, 2000).

CBDM provides for the possibility of assessing daylight throughout the year in dynamic conditions of the local daylight climate, including direct sunlight. This performance-based approach to daylight design has many benefits but also pitfalls. The CBDM method is not considered suitable for use in the early stages of design. In the early stages, conceptual designs often, and significantly, change. Architects and designers prefer simple and yet sufficiently reliable methods for determining the availability of daylight in buildings. Many practical designers consider the ADF method to be a sufficiently proven method for assessing daylight in buildings in locations with a dominant occurrence of cloudy days. For the assessment of both visual and non-visual daylight in side-lit rooms, we propose a modified mADF (melanopic Average Daylight Factor) method that respects the principles of daylight theory and captures the essential parameters determining the non-visual potential of daylight.

2.1 Computational procedure

A well-known average daylight factor method will be modified to account for external obstacles with different reflectance factors and the vertical daylight component on the window. The proposed mADF method also includes several computational procedures, which improve the calculation of both melanopic and photopic daylight illuminance. During the year, a wide range of luminance patterns occur in the sky. We assume that the variability of luminance patterns noticeable in the annual average better reflects a uniform luminance sky model than a standard heavily overcast sky model. In mADF, the sky illuminance is determined from a sky of constant brightness. The interreflection of daylight in the outdoor and indoor environments is calculated under overcast sky conditions (an overcast sky is used in the ALFA software (Solemma & Alertness, 2018)) and standard overcast sky (CIE, 1955). mADF is a simplified flux-type method. Lynes (1979) proposed a formula for calculating the average illuminance over all interior rectangular indoor space in order to simplify the computational assessment of daylight in buildings based on point daylight factors. This formula was later modified (Crisp and Littlefair, 1984) based on measurements in a classroom model under an artificial standard overcast sky, so that the calculation results were the average illuminance on the reference plane according to the formula:

$$\mathrm{ADF} = A_w\ \tau_o\ \theta/(A_t\,(1-\rho^2))\ \ [\%] \qquad (1)$$

where

- A_W is the area of the window (m^2),
- θ is the vertical angle subtended by the visible sky in degrees (Fig. 1),
- τ_o is the overall loss factor for diffuse light passing through the daylight opening (-),
- A_t is the total area of the room surfaces (ceiling, floor, walls, windows) (m^2),
- ρ is the area weighted mean reflectance of all the interior surfaces (-).

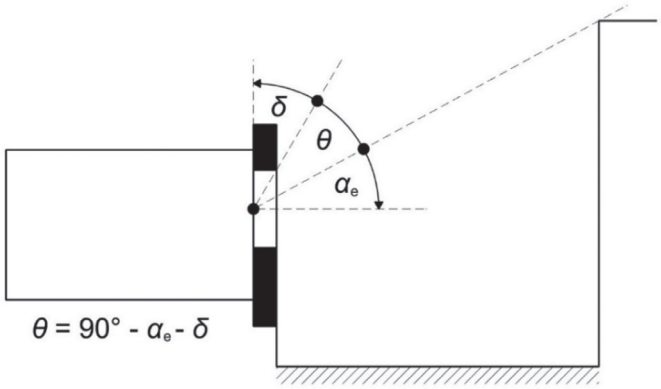

Fig. 1 *Angle θ*

Angle α_e in Fig. 1 is the equivalent obstruction angle, which can be determined for any obstructing geometry by using the method described by Hraška and Štujber (1997) and Hraška (2000). Later, several other authors analyzed and tested equation (Eq.) (1) (Naeem and Wilson, 2007; Bonaiuti and Wilson, 2007; Reinhart and LoVerso, 2010), primarily using the Radiance simulation program (Radiance, 2023). These authors concluded that the ADF method is adequate for the initial design of daylight provision in buildings. The ADF method has gained significant popularity in practice due to its simplicity and relatively loose interpretation of criteria. The ADF method is suitable for the work of architects because it simply and clearly relates the geometric and spatial characteristics of the creation of a building's environment to the requirements for daylight provision, especially in climatic conditions with a dominant occurrence of overcast skies.

From a practical point of view, the ADF method has the advantage of restricting the possibility of "creative manipulation" with computation parameters so that it can be used by the majority of designers and not only by specialists. On the other hand, the ADF is a certain mathematical construct, which is only valid for small rooms under a strict set of parameters. One of the disadvantages of the ADF is that it does not allow for the consideration of different reflectance factors of surfaces in front of a window. The proposed mADF method is based on the vertical daylight factor (VDF) on the window D_w. The value of D_w takes into account the range of external obstructions of the window as well as the reflectance factors of light from external surfaces. In mADF, the photopic and melanopic photometric properties of materials and surfaces are determined by the D65 light source, which represents the spectral composition of "average daylight".

D_w is the sum of the sky component of daylight factor D_s and the exterior reflected factor D_ρ, due to the interreflection of daylight between the terrain and the external surfaces of buildings, or other objects located in front of a window:

$$D_w = D_s + D_\rho \quad [\text{- or \%}] \tag{2}$$

The sky component of the daylight factor on a window is determined by the following formula:

$$D_s = 0.000051\,\alpha_U^2 - 0.01037\;\alpha_U + 0.51 \quad [-] \tag{3}$$

Where α_U is obstruction angle, according to Fig. 2, in degrees.

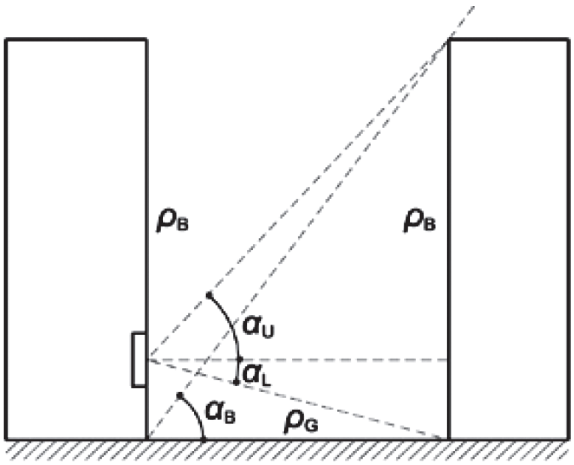

Fig. 2 *Angles α_U, α_L and α_B*

According to (Li et al., 2009), the ratio of the ground-reflected component of the daylight factor at a vertical window $D_{\rho T}$ to the unit horizontal ground illumination can be calculated from the equation:

$$D_{\rho T} = \rho_G\, E_G\, (1 - sin\,\alpha_L)/2 \quad [-] \tag{4}$$

Where

ρ_G average light reflectance of the ground (melanopic or photopic) [-],

$E_G = 0.9 - 0.009\,\alpha_B$ [-],

α_L and α_B are the angles marked in Fig. 2 [degrees].

The reflected component of the daylight factor on a vertical window from a shading building, $D_{\rho B}$, is determined as follows:

$$D_{\rho B} = \rho_B\, D_B\, S\, cos\,\delta/\pi \quad [-] \tag{5}$$

Where

D_B is the average vertical daylight factor on the obstacle according to (Li et al., 2009)

$$D_B = (0.92 - 2.7 \times 10^{-3}\alpha_U - 1.1 \times 10^{-4}\alpha_U^2) \times \times 0.935^{\left(\frac{\alpha_L}{10}-1\right)} \times 0.5,$$

ρ_B average light reflectance of obstructing building (melanopic or photopic).

Parameter S expresses the size of the obstacle (an infinite-length urban canyon), and δ is the angle between the window normal and the height center of the obstacle:

$$S = 2\,\beta\,\pi/180$$
$$\beta = \alpha_U + \alpha_L$$
$$\delta = \arctan(v_p - tan\,\alpha_L)$$
$$v_p = (tan\,\alpha_L + tan\,\alpha_U)/2$$

The effective reflectance of daylight, ρ_o, of the cavity among buildings and the ground can be approximately determined from the following equation:

$$\rho_o = 0.009 \times \alpha_B \times (\rho_B + \rho_T)/2 \quad [-] \tag{6}$$

We can estimate the reflected component D_ρ of D_w using the following formula:

$$D_\rho = \left(D_{\rho T} + D_{\rho B}\right) \times (1/(1-\rho_o)) \quad [-] \qquad (7)$$

The daylight illuminance in the room is determined by the value of the daylight flux falling on the window, whoch is reduced by light losses when passing through the window. The mADF on the reference plane is directly proportional to the D_w according to the following equation:

$$mADF = k \times D_w \quad [-] \qquad (8)$$

Chaiyakul (2005) presents a relationship for determining the value of k, which has the following form after our correction factors are added:

$$k = 2\, A_w\, \tau_o\, \psi\, \mu / (A_t\, (1-\rho^2)) \quad [-] \qquad (9)$$

The parameter τ_o takes into account the loss of diffuse light when it passes through the daylight opening:

$$\tau_o = \tau_d \,.\tau_2 \,.\tau_3 \,.\tau_4 \quad [-] \qquad (10)$$

Where τ_d is the light transmittace of glazing. For ordinary glazing $\tau_d = 0.9 \times \tau_1$.

The meaning of τ parameters is:

- τ_1 light transmittance when light hits the glazing perpendicularly (melanopic or photopic),
- τ_2 correction factor for the window framing,
- τ_3 correction factor for glazing dirt,
- τ_4 correction factor for elements that permanently shade the window glazing (e.g., fixed window grilles).

The parameter ψ takes into account the loss of daylight due to the thickness of the window wall. The meaning of the parameters in Eq. (11) is obvious from Fig. 3.

$$\psi = (1 - e^{-0.624\,x})(1 - e^{-0.614\,y}) \quad [-] \qquad (11)$$

Where

$$x = \frac{h_w}{th} \quad and \quad y = \frac{w_w}{th}$$

If $x > 10$, then $x = 10$; and if $y > 10$, then $y = 10$.

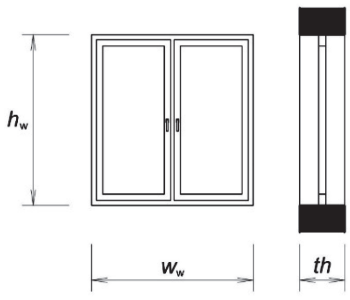

Fig. 3 *The dimensions in Eq. (11)*

The correction factor μ takes into account the leakage of light through the window due to the internal interreflection of light (Meshkov, 1957, p. 201).

$$\mu = 1 - \varphi$$
$$\varphi = (\rho\,(A_w/A_t) / (1 - \rho\,(1 - (A_w/A_t)))\,\tau_o \quad [-] \qquad (12)$$

In smaller rooms with bright interior surfaces and large windows, light leakage from a room can be noticeable.

Using Eq. (13), we can calculate the required size of the window to achieve the desired mADF (or photopic pADF) on the reference plane:

$$A_w = mADF\; A_t\; (1-\rho^2) / (2\, D_w\, \tau_o\, \psi\, \mu\,) \quad [-] \qquad (13)$$

Whether it is a photopic or melanopic daylight factor depends on whether the light transmission factors through the glazing and the light reflectance factors from the outer and inner surfaces are entered as photopic (pADF) or melanopic (mADF). In the mADF and pADF methods, the same D65 light source is considered.

The parameter k includes the geometry of the room and the daylight opening, as well as the photometric properties of the glazing and interior surfaces, and the interreflection of light in the room. The parameter k is significantly more suitable for predicting the average illuminance of a side-lit room than the commonly used wall-to-window ratio (WWR) or the ratio of the window area to the floor area (WFR), which only considers the geometry.

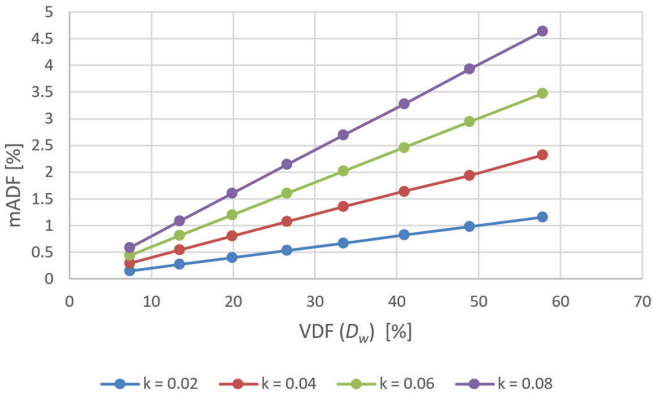

Fig. 4 *Melanopic average daylight factor (mADF) values plotted as a function of the vertical daylight factor at a window (Dw) and smaller values of the parameter k*

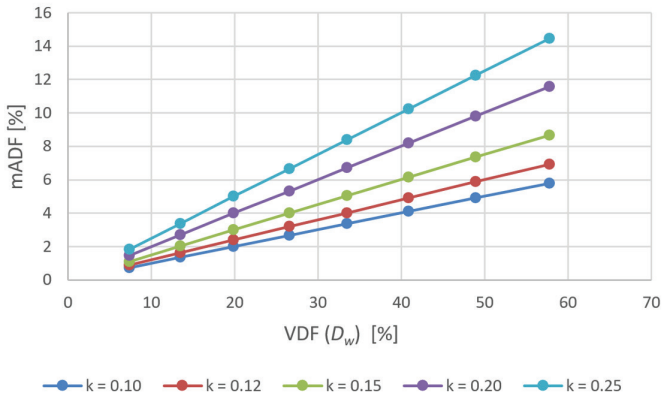

Fig. 5 *Melanopic average daylight factor (mADF) values plotted as a function of the vertical daylight factor at a window (Dw) and larger values of the parameter k*

The mADF method can be used to assess the side daylighting of smaller rooms, whose shape can be approximated by a prism, the length of which is not significantly larger than twice the height. The limiting size of a side-lit room can be considered to be a room with floor dimensions smaller than 7 × 7 m, whose ceiling height is up to 3.5 m.

2.2 Comparison of the mADF method with measurements under an artificial sky and with simulations by the ALFA software

The ALFA (Adaptive Lighting for Alertness) circadian lighting software (Solemma, 2017) was used for numerical modeling of non-visual (circadian) daylighting potential. Circadian lighting simulations in ALFA were compared to measurements on a model room (Fig. 6) under a hemispheric artificial CIE uniform sky (Fig. 7). The calculations in ALFA were carried out on December 21, at 12 o'clock in Bratislava (Lat 48°08', Lon 17°10') under a cloudy sky. Under these conditions, the orientation of the room to the cardinal points does not affect its daylighting. The ALFA software uses its own sky models (Mayer and Kylling, 2005), which differ from the standardized models by CIE (CIE, 2003). In the vicinity of the window in the model room, the measured values of the horizontal and vertical illuminance were significantly higher than the ALFA outputs for all the obstruction angles. In the middle of the room, the calculated and measured illuminances were almost equal, and the software-calculated illuminance values were slightly higher than the measured values in the back of the model room. One of the reasons for the large differences between the measured and ALFA-calculated DF values is likely the difference in sky models. Due to the fact that we do not know the luminance distribution on the cloudy sky in the software used, we cannot

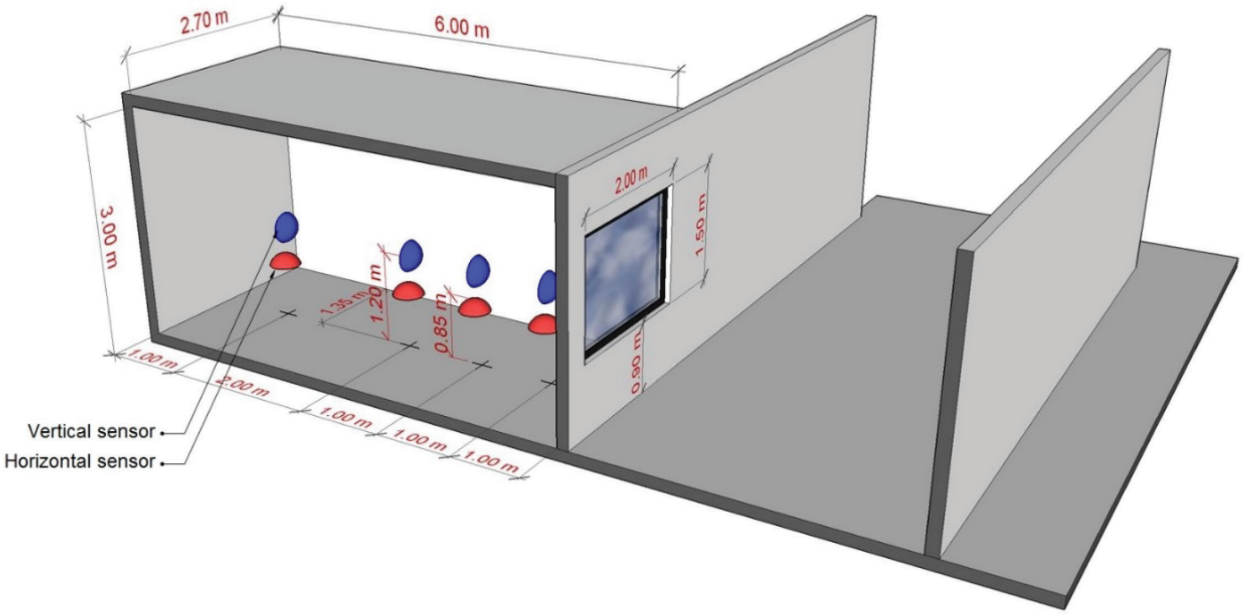

Fig. 6 *A room model and obstruction that was used to test a simplified calculation method by measurements under an artificial sky*

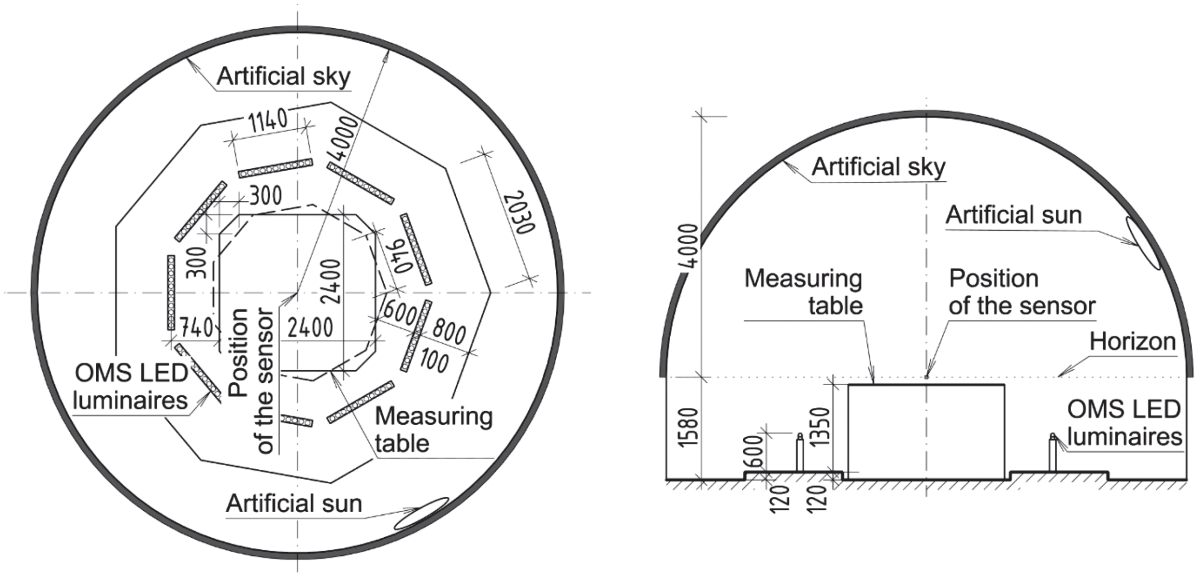

Fig. 7 *Scheme of the artificial sky of the Slovak Academy of Sciences in Bratislava (Slovak Republic)*

analyze the differences between the measured and calculated DF in more detail. ALFA sky models have not been validated against measured data (Diakite-Kortlever, 2022). The determination of the interreflection component of daylight illuminance in the proposed simplified calculation tool mADF is based on the results of the ALFA simulations.

Fig. 8 shows a comparison of the vertical daylight factors D_w on the window of the room in Fig. 6 calculated by the mADF method and the ALFA program with measured values under the artificial sky with uniform luminance. The values of D_w were measured and calculated for the light external surfaces and various angles of obstruction, at which the mADF method slightly overestimated the vertical illuminance of the vertical window.

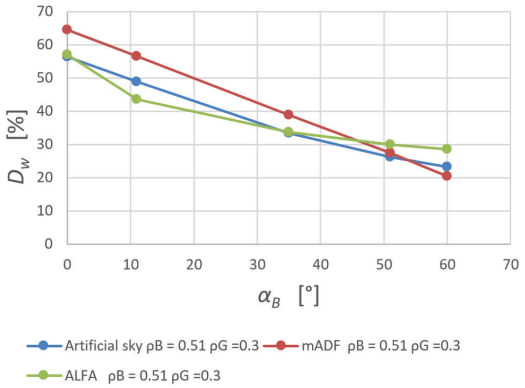

Fig. 8 *Measured and calculated values of D_w, depending on the obstruction angle α_B*

The ALFA software and the proposed simplified method were used to calculate the ADF in the room in Fig. 6 on a horizontal reference plane 0.85 m above the floor. The calculation parameters of the room and the window were defined as follows: room width 2.7 m, room depth 6 m, room height 3 m, window width 2 m, window height 1.5 m, sill height 0.9 m, wall thickness 0.18 m, ratio of glazing area to window area 0.82, glazing transmittance $\tau_1 = 0.88$, and correction factor for glazing dirt $\tau_3 = 1$. The values of the surface reflectance factors were determined as follows: gray floor and exterior terrain $\rho_v = 0.30$, light gray interior walls and obstacle $\rho_v = 0.51$, white ceiling $\rho_v = 0.72$, and reflectance of the inner side of the window $\rho_v = 0.25$. In the case considered, the value of the parameter k is 0.0586. A comparison of the results of the ADF calculations on the horizontal reference plane using the simplified mADF method and the ALFA program for multiple obstruction angles is shown in Fig. 9.

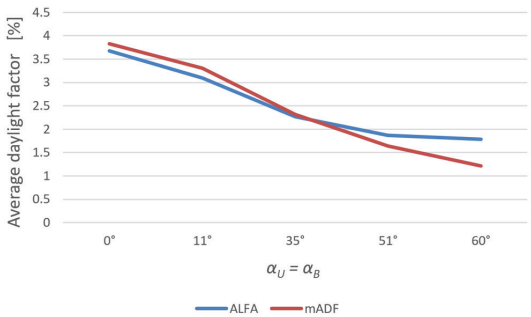

Fig. 9 *Average daylight factors in a model room calculated by the mADF method and the ALFA software for different obstruction angles*

Fig. 9 shows a relatively good agreement between the average illuminance of the reference plane of the above-characterized model room calculated by the numerical simulations using the ALFA software and calculated using the proposed simplified mADF method. This is quite surprising, given that the methods use different sky models.

Additive glazing in loggias, the occupant's use of shading devices, dark carpets on the floor, dusky wall and ceiling paints, trees and other plants in front of buildings, furniture, the user's behavior, etc., influence the daylighting of a room much more than a slight degree of uncertainty in a calculation method.

2.3 Calculation example

In the room shown in Fig. 6, with the photometric properties of the materials and surfaces listed in Tab. 1, we calculated the mADF and photopic ADF (pADF) on the reference plane. In Tab. 2, the values of mADF and pADF and their ratios were calculated using the proposed calculation method for several obstruction angles. The orange and yellow surfaces are spectral filters of blue light. For this reason, the values of mADF are lower than pADF. The impact of the pale orange obstacle on the reduction of mADF increases with the increasing obstruction angle.

Tab. 1 *Melanopic and photopic photometric characteristics of glazing and surfaces*

Surface (material) / color		Light reflectance / transmittance		M/P ratio [-]
		Melanopic (M) ρ_{mel} [-]	Photopic (P) ρ_v [-]	
Walls / pale yellow		0.54	0.79	0.68
Ceiling / white		0.79	0.84	0.94
Floor / grey		0.33	0.34	0.97
Glazing	reflectance	0.24	0.25	0.96
	transmittance	0.66	0.65	1.02
Obstacle / pale orange		0.28	0.57	0.49
Terrain / dark grey		0.20	0.20	1.00

Tab. 2 *The average melanopic (mADF) and photopic (pADF) daylight factors on the reference plane in the room assessed with different melanopic and photopic surface reflectances*

Obstruction angles $\alpha_B = \alpha_U$	mADF [%]	pADF [%]	M/P ratio [-]
0°	2.98	3.89	0.77
10°	2.53	3.41	0.74
20°	2.12	2.97	0.71
30°	1.74	2.56	0.68
40°	1.38	2.15	0.64
50°	1.04	1.70	0.61
60°	0.71	1.21	0.59
70°	0.40	0.68	0.59

The calculation example shows that the difference between the melanopic and photopic daylight illuminance is significant in the case considered. The decrease in the M/P ratio with the increasing obstruction angle of the window is caused by the low reflectance of melanopic light from the orange obstructing obstacle. The data in Tab. 2 show that the optimization of daylighting in terms of non-visual effects can differ from the evaluation, taking into account only the visual effects of light.

The proposed method makes it possible to evaluate daylight by photopic measures and, at the same time, to evaluate the non-visual potential by melanopic ADF, which can be converted into melanopic illumination.

2.3 Indicator of the non-visual potential of daylight in side-lit rooms

The latest metrics of non-visual effects are mostly based on the melanopic illumination of the eyes (Lucas et al., 2012). Melanopic illuminance is currently typically calculated using the melanopic action spectrum according to the CIE standard (CIE S 026/E, 2018). For practical reasons, melanopic illuminance is usually calculated on a vertical plane, typically at a height of 1.2 m above the floor level. Various studies have shown that exposure to melanopic illuminance levels of 100-300 lux can have a significant impact on non-visual effects of light. For example, in (Brown et al., 2022), a large group of experts recommended a minimum indoor melanopic light exposure of 250 mlx ("melanopic lux") vertically at eye level during the day in indoor environments.

Unfortunately, this recommendation does not specify either the time of day nor the places in the interior where the stated level should be achieved, nor the type of lighting. This recommendation also does not specify at what angle viewing the vertical illuminance of 250 mlx should be achieved. The direction of the view is of key importance for the evaluation of vertical illuminance in the case of lateral daylighting. Many authors and practitioners use the WELL Building Standard v2 methodology (IWBI, 2022) to assess circadian lighting. In section "L03: Circadian Lighting Design", Tier 1 requires a vertical illuminance of at least 136 melanopic equivalent daylight illuminance D65 (m-EDI) for artificial lighting in regularly occupied spaces. In the case that a physically unspecified level of daylight illuminance in the interior space is provided in the WELL method, Tier 2 requires a minimum of 109 mlx. In Tier 2, in the case of "enhanced daylight access", a minimum of 163 mlx is required for such a solution to receive 3 points in the evaluation system. During the several years of the existence of the WELL method, the criterion values for circadian lighting and the corresponding professional terminology have changed several times. In most cases, vertical illuminance is significantly lower than horizontal illuminance in artificially lit interiors. On the other hand, in

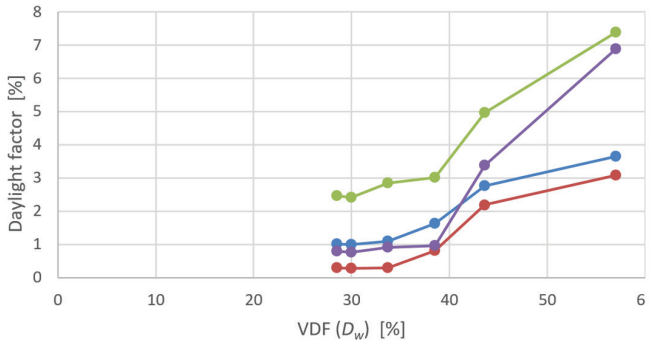

All the surfaces are orange except for the grey terrain.
$\rho_v = 0.48$, $\rho_{mel} = 0.17$, $\rho_G = 0.20$

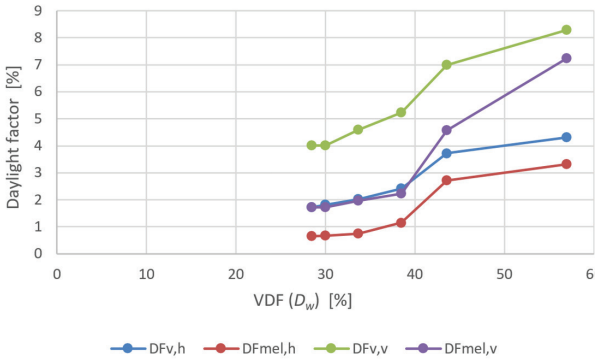

All the surfaces are orange except for the grey terrain.
$\rho_v = 0.48$, $\rho_{mel} = 0.17$, $\rho_G = 0.20$

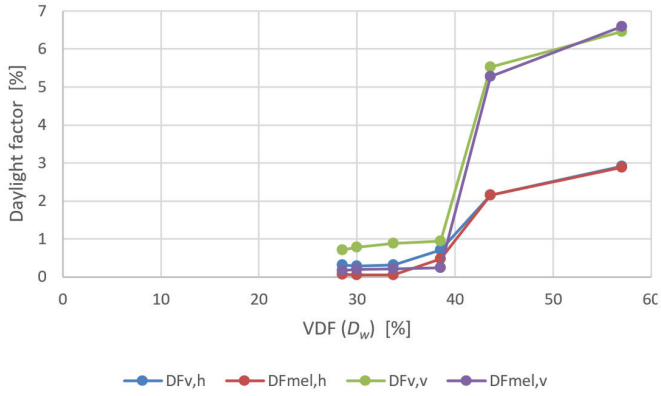

All the surfaces are dark red except for the grey terrain.
ρv = 0.16, ρmel = 0.04, ρG = 0.20

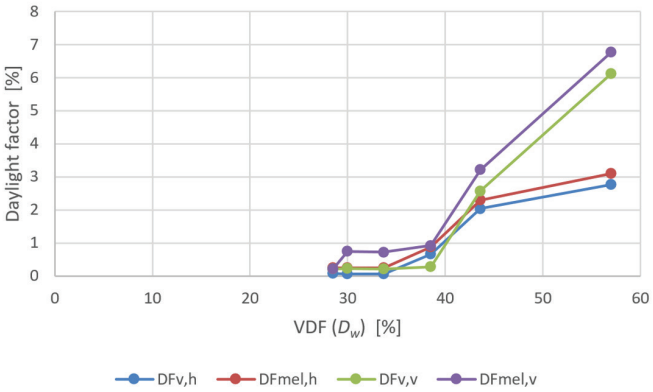

All the surfaces are dark blue except for the grey terrain.
ρv = 0.05, ρmel = 0.15, ρG = 0.20

Fig. 10 *Vertical photopic and melanopic daylight factors (DFv,v and DFmel,v) and horizontal daylight factors (DFv,h and DFmel,h) plotted against the daylight factor on a window (Dw) at a position 2 m from the window in the room in Fig. 6*

the case of lateral daylighting, vertical illuminance is typically twice as high as horizontal illuminance at the same point, when looking towards a window with little external shading.

In general, it can be stated that daylight in buildings is the most suitable for circadian lighting in terms of its intensity, spectral quality, and the timing of the exposure. The intensity and spectral composition of daylight are constantly changing. The spatio-temporal distribution of daylight in a room is constantly changing at each point during days and over years.

A detailed assessment of the non-visual potential of daylight in short time periods throughout the year has many challenges. In addition to dynamic changes in the local light climate and its spectral composition, it is necessary to take into account the difficult-to-predict dynamics in the use of shading devices and the behavior of the users of the spaces.

Using the ALFA simulation software, melanopic and photopic illuminance on vertical surfaces at a height of 1.2 m above the floor and horizontal illuminances at a height of 0.85 m above the floor were calculated in the same positions in side-lit rooms. The calculations were carried out under a cloudy sky in the location of Bratislava, Slovakia. At the same time, the average photopic and melanopic illuminances on the reference planes of rooms at a height of 0.85 m above the floor were calculated. In the calculation variants, the colors of the exterior and interior surfaces were changed. The colors of the surfaces were either the same on all the surfaces or the colors and light reflectances on the individual surfaces of the room were combined. Fig. 10 illustrates a part of the calculation results for a position 2 m from a window, with vertical photopic and melanopic daylight factors ($DF_{v,v}$ and $DF_{mel,v}$) and horizontal daylight factors ($DF_{v,h}$ and $DF_{mel,h}$) plotted against the daylight factor on the window (i.e. D_w). The graphs shown apply to the room in Fig. 6 and for the same colors of the exterior and interior surfaces, whose photopic and melanopic reflectances are shown in Fig. 10. As expected, both the $DF_{v,v}$ and $DF_{mel,v}$ values were higher than $DF_{v,h}$ and $DF_{mel,h}$. The size of the obstruction and surface reflectances significantly affected the distribution of light in the room, the average DF value on the reference plane, and the ratios of the vertical and horizontal illuminance in virtually every location in the room.

As the size of the obstruction increases, the difference between the values of the horizontal and vertical illuminance decreases, but the vertical illuminance always remains higher. In a very unlikely scenario of extremely dark interior surfaces, a larger dark obstruction and dark interior surfaces will cause a rapid decrease in both the vertical and horizontal illuminances to very low values. In the case of dark blue surfaces, the favorable ratio of the melanopic to photopic reflectance has only a small impact on the value of the melanopic illuminance. Spectrally neutral light surfaces are more effective in terms of melanopic illuminance than darker blue colors, even though they have a much more favorable ratio of melanopic to photopic reflectance (about 2.6).

Fig. 11 shows the ratios of vertical to horizontal illuminance calculated by ALFA at a distance of 2 m from the window in the room shown in Fig. 6 for ordinary spectrally neutral surfaces. The reflectances of the floor of the room and the external terrain were assumed to be $\rho_v = 0.31$, the reflectances of the walls of the room and obstacles to be $\rho_v = 0.51$, and the ceiling reflectance of the room to be $\rho_v = 0.72$. If we compare the values of the photopic average daylight factor (pADF) and $DF_{v,h}$ at a distance of 2 m from the window, their values are similar throughout the range of the D_w values. The vertical illuminance $DF_{v,v}$ is significantly higher than the horizontal illuminance, which is also due to the relatively bright external obstruction. With a small obstruction, the vertical illuminance towards the window is twice as high as the horizontal illuminance in a cloudy sky. As the obstruction increases, this difference decreases, but it is still significant.

The ratio of the vertical illuminance to the average illuminance on a reference plane in a side-lit room in a zone near a facade is nonlinear and is significantly affected by the size of the obstruction and its reflectance.

We propose to assess the non-visual potential of daylight in side-lit rooms using an indicator, which is the melanopic vertical illuminance of a sensor at a height of 1.2 m above the floor at a distance of 2 m from a window; this sensor is oriented perpendicular to a window. After analyzing the results of the simulations using the ALFA software in the case of light reflectance of the terrain in front of a window of around 0.20 and the light reflectance of an obstacle in the range of 0.25 – 0.55, we can approximately determine the ratio of the vertical illuminance to the average illuminance on a reference plane R at a distance of approximately 2 m from the window from the formula:

$$R = \frac{DF_{ver,2\,m}}{ADF} = 70.69 \times D_w^2 \times \rho_B + 5.87 \times D_w^2 - 49.01 \times D_w \times \rho_B + 0.099 \times \rho_B^2 - 6.555 \times D_w + 6.79 \times \rho_B + 3.701 \quad [-] \quad (14)$$

Where D_w and ρ_B are dimensionless numbers.

The functional dependence of the value R on the daylight factor at the vertical window D_w and the light reflectance of the obstruction ρ_B according to Eq. (14) is shown in Fig. 12.

3 THE AUTONOMY OF THE NON-VISUAL POTENTIAL OF DAYLIGHT IN SIDE-LIT ROOMS

The intensity of daylight and the amount of time it is available throughout the year varies greatly from location to location on the Earth. At mid-latitudes and in locations with predominantly overcast skies, daylighting criteria have traditionally been linked to the availability of diffuse natural light. We assess the autonomy of the non-visual potential by the availability of melanopic daylight on the potential non-visual indicator, which is defined above.

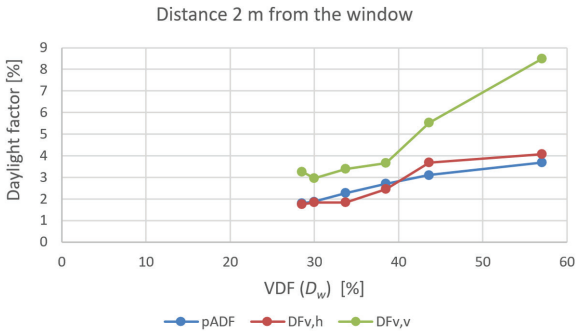

Fig. 11 Vertical and horizontal daylight factors (DFv,v and DFv,h) at a distance of 2 m from the window in the room in Fig. 6 and the average photopic daylight factor (pADF) on the reference plane of the room

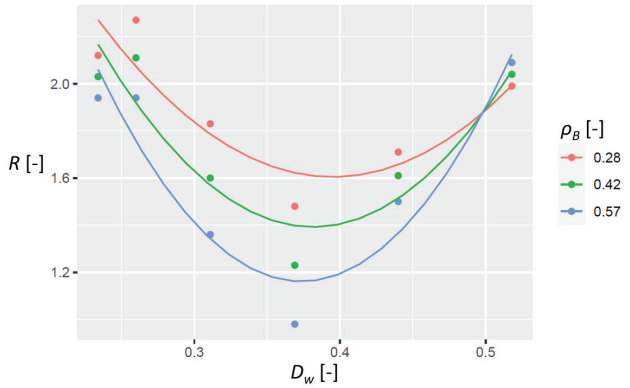

Fig. 12 *Dependence of the parameter R on the daylight factor at the vertical window Dw and the light reflectance of the obstruction ρB*

The occurrence of diffuse horizontal illuminance in Bratislava is variable throughout the year, see Fig. 13. Fig. 13 shows the cumulative frequency distribution of the exterior diffuse horizontal illuminance E_{vd} in Bratislava (Ferenčíková and Darula, 2019). In the winter, the levels of illuminance are significantly lower than in the other seasons. While on average throughout the year, horizontal illuminance above 10 klx occurs 60 % of the time of days, in the winter months it is less than 30 %. Relatively high intensities of diffuse illuminance in the summer months increase the average annual illuminance. Due to the purpose and method of the proposed simplified assessment of the non-visual potential of daylight in buildings, we consider that assessing it on the annual occurrence of diffuse daylight is a reasonable choice. However, the availability of diffuse light can be easily determined from Fig. 13, even in individual months of the year.

The illuminance at the window is calculated from the given exterior horizontal diffuse illuminance E_{vd} as follows:

$$E_W = E_{vd} \times D_w \quad (lx \text{ or } klx) \text{ [-]} \tag{15}$$

The average illuminance on the reference plane is:

$$E_{aver} = k \times E_w \quad (lx \text{ or } klx) \text{ [-]} \tag{16}$$

The average daylight factor (melanopic or photopic) on the reference plane is:

$$ADF = k \times D_w \quad (- \text{ or } \%) \text{ [-]} \tag{17}$$

We can assess the vertical illuminance of the virtual sensor (melanopic or photopic) approximately 2 m from the window (i.e., the indicator) using the following formula:

$$E_{ver,2\,m} = R \times E_{aver} \quad (lx \text{ or } klx) \text{ [-]} \tag{18}$$

The percentage probability of exceeding a certain value of the annual average diffuse horizontal illuminance E_{vd} in Bratislava P is determined by the following formula:

$$P = -8 \times 10^{-6} \times E_{vd}^{\,4} + 5 \times 10^{-4} \times E_{vd}^{\,3} + 4 \times 10^{-2} \times E_{vd}^{\,2} - 4{,}4 \times E_{vd} + 100 \quad [\%] \tag{19}$$

Assume that the mADF in a room in Bratislava is 1.5 %. The vertical daylight factor at the window is D_w = 0.45, and the melanopic light reflectance of the obstacle is ρ_B = 0.30. According to (EN 17037, 2018), the median exterior diffuse

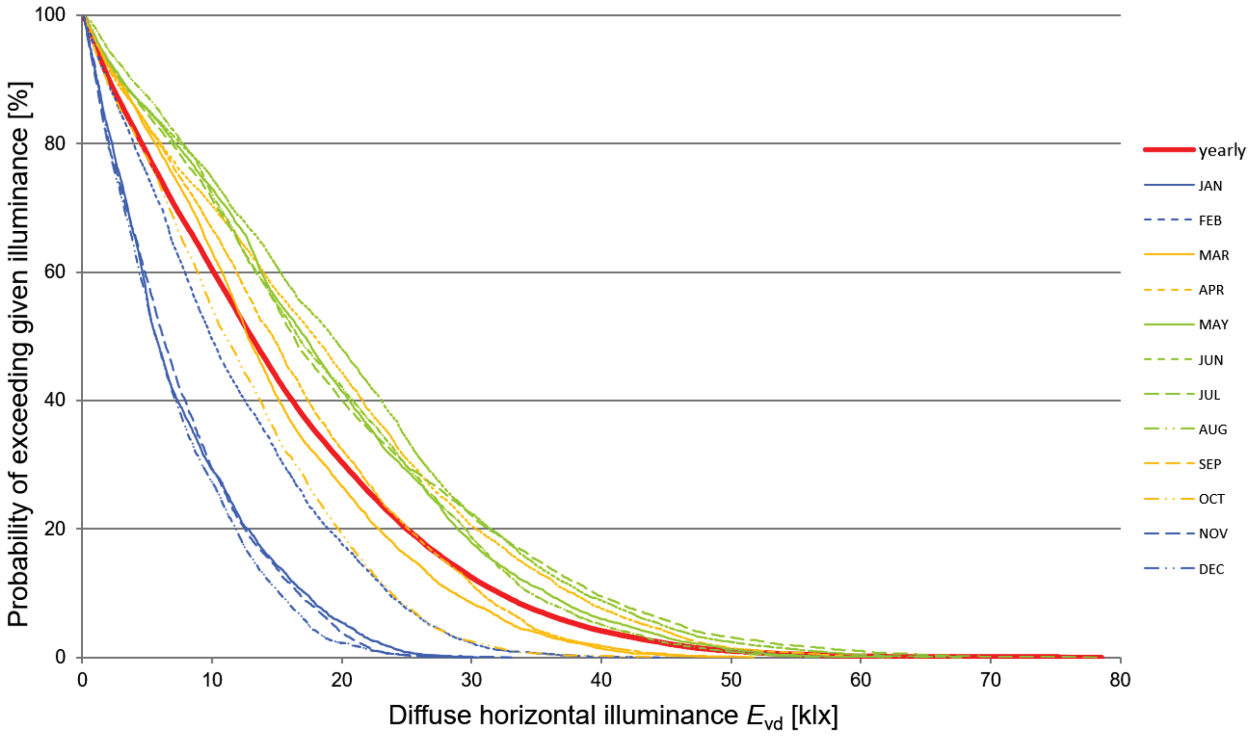

Fig. 13 *Cumulative frequency distribution of available exterior diffuse horizontal illuminance in Bratislava, Slovakia (Ferenčíková and Darula, 2019)*

horizontal illuminance in Bratislava is E_{vd} = 16,300 lx. The average median illuminance of the reference plane in the given hypothetical room will be E_{aver} = 244.5 mlx. From Eq. (14) under the given conditions, we can determine R = 1.66. From Eq. (18), we find $E_{ver,2\ m}$ = 406 mlx. The value of 406 mlx or higher will be achieved only half the time of the year with daylight. The median autonomy of the non-visual potential is 50 % in this case. The probability of exceeding 7,500 lx within the average annual availability of diffuse horizontal lighting E_{vd} in Bratislava is P = 69 %. In this case, the value of *Ever,2 m* will be above 187 mlx during 69% of all hours in the year with daylight.

4 CONCLUSIONS

This article describes a simple analytical method for assessing the non-visual potential of rooms with lateral daylighting. The proposed assessment method is based on the well-known average daylight factor method and was tested using model measurements under an artificial sky with constant luminance and simulations of photopic and melanopic horizontal and vertical illuminance in laterally lit rooms in the ALFA simulation software. Although approximate, this method is suitable for assessing the non-visual potential of the lateral daylighting of regular interior spaces in the initial stages of their design. The proposed method is applicable in concrete urban and architectural conditions. The computational method takes into account the size of the room, the size of the windows, external shading, and the photometric characteristics of materials and external and internal surfaces for both photopic and melanopic conditions. A user-friendly computational tool was also developed in the LabVIEW (2023) environment, which allows for the optimization of the design of both photopic and melanopic daylighting. This method also makes it possible to assess the photopic and melanopic autonomy of lateral daylighting, taking into account the available outdoor diffuse horizontal illuminance in locations with a year-round prevalence of cloudy skies. This easy-to-use tool can be used by people who are not specialized in the assessment of light environments in buildings.

Acknowledgments

This work was supported by the Slovak Research and Development Agency under Contract APVV-18-0174 and was also supported by VEGA Grant No. 01/0042/21.

REFERENCES

Acosta, I. – Campano, M. Á. **– Leslie, R. – Radetsk, L. (2019)** *Daylighting design for healthy environments: Analysis of educational spaces for optimal circadian stimulus*. Solar Energy, 193 /2019) 584-596.

Amundadottir, M. L. – Rockcastle, S. – Sarey, K. M. – Andersen, M. (2017) *A human-centric approach to assess daylight in buildings for non-visual health potential, visual interest and gaze behavior*. Building and Environment, 113, 5-21.

Aries, M. – Aarts, M. – van Hoof, J. (2015) *Daylight and health: a review of the evidence and consequences for the built environment.* Lighting Research and Technology; 47: 6-27.

Berson, D. M. – Dunn, F. A. – Takao, M. (2002) *Phototransduction by retinal ganglion cells that set the circadian clock. Science*, 295: 10-10.

Bonaiuti, S. P. G. – Wilson, M. (2007) *An analysis of the (BRE) average daylight factor and limiting depth guidelines as design criteria.* In: 2nd PALENC Conference and 28th AIVC Conference on Building Low Energy Cooling and Advances Ventilation Technologies in the 21st Century, Crete, Greece, pp. 739-745.

Boyce, P. R. (2010) *The impact of light in buildings on human health. Indoor Built Environment*, 19(1): 8-20.

Brainard, G. C. – Hanifin, J. P. – Greeson, J. M. – Byrne, B. – Glickman, G. – Gerner, E. – Rollag, M. D. (2001) *Action spectrum for melatonin regulation in humans: evidence for a novel circadian photoreceptor. Journal of Neuroscience*, 21: 6405-6412.

Brown, T. M. – Brainard, G. C. – Cajochen, C. – Czeisler, C. A. – Hanifin, J. P. – Lockley S. W. et al. (2022) *Recommendations for daytime, evening, and nighttime indoor light exposure to best support physiology, sleep, and wakefulness in healthy adults.* PLoS Biology 20(3): 1-24, e3001571

Chaiyakul, Y. (2005) *Daylighting criteria in urban buildings in Bangkok.* The 2005 World Sustainable Building Conference, Tokyo, 27-28 Sept., 04-030, pp. 1814-1821.

CIE (1955) Commission Internationale de l'Éclairage: *Natural Daylight, Official recommendation.* Compte Rendu CIE 13th Session, 2, part 3.2, 2-4.

CIE S 026/E (2018) *System for Metrology of Optical Radiation for ipRGC-Influenced Responses to Light.* CIE, Vienna.

CIE (2003) ISO 15469:2004/CIE S011/E:2003 *Spatial distribution of daylighting - CIE Standard General Sky.*

Crisp, V. H. C. – Littlefair, P. J. (1984) *Average daylight factor prediction.* Proceedings of the CIBS National Lighting Conference 1984, University of Cambridge, Robinson College, 16-18 April, London, CIBSE.

Diakite-Kortlever, A. – Knoop, M. (2021) *Forecast accuracy of existing luminance-related spectral sky models and their practical implications for the assessment of the non-image-forming effectiveness of daylight.* Lighting Research and Technology, 53(7):147715352098226

Diakite-Kortlever, A. (ed.) **(2022)** A Technical Report of IEA SHC Task 61 / EBC Annex 77 Subtask C3 "*Spectral sky models for advanced daylight simulations* "

Ezpeleta, S. – Orduna-Hospital, E. – Aporta, J. – Luesma, M. J. – Pinilla, I. – Sánchez-Cano, A. (2021) *Evaluation of Visual and*

Nonvisual Levels of Daylight from Spectral Power Distributions Considering Orientation and Seasonality. Applied Sciences, 11, 5996.

EN 17037 (2018) *Daylight in buildings.*

Ferenčíková, M. – Darula, S. (2019) *Daylight availability in interiors during operating time.* Saarbrücken: LAP LAMBERT Academic Publishing, 81 pp. ISBN 978-613-9-45969-8.

Gooley, J. J. – Ho Mien, I. – St Hilaire, M. A. – Yeo, S. C. – Chua, E. C. – van Reen, E. – Hanley, C. J. – Hull, J. T. – Czeisler, C. A. – Lockley, S. W. (2012) *Melanopsin and rod-cone photoreceptors play different roles in mediating pupillary light responses during exposure to continuous light in humans.* Journal of Neuroscience, Oct 10; 32(41):14242-53.

Hraška, J. – Štujber**, M. (1997)** *A Graphic Daylight Factor Technique for Estimating Daylight on Vertical Planes.* Slovak Journal of Civil Engineering, No. 3, pp. 5-8.

Hraška, J. (2000) *Right to light versus right to build.* Proceedings of PLEA 2000 "Architecture, City, Environment." Cambridge (UK) : James & James Ltd., pp. 839-840.

Hraška, J. (2012) *A proposal of simplified standardisation of dwellings daylighting in Slovakia.* Proceedings of the Conference LUMEN V4, Bratislava, Sept. 26-28, pp. 86-93. ISBN 978-80-89275-32-8

Inanici, M. & ZGF Architects LLP (2015) *Lark Spectral Lighting.*

Inanici, M. – Brennan, M. – Clark, E. (2015) *Spectral daylighting simulations: Computing circadian light.* Proceedings of 14th Conference of International Building Performance Simulation Association, Dec. 7-9, (1245-1252), Hyderabad, India: IBPSA.

IWBI (International WELL Building Institute) (2022) "*WELL v2 Building Standard, Light, Feature L03 Circadian Lighting Design*". https://v2.wellcertified.com/en/wellv2/light/feature/3 (accessed at 22/09/2023)

Li, D. H. W. – Cheung, G. H. W. – Cheung, K. L. – Lam, J. C. (2009) *Simple method for determining daylight illuminance in a heavily obstructed environment*. Building and Environment, 44 (2009) 1074-1080.

LabVIEW (2023) https://www.ni.com/en.html (accessed at 22/09/2023)

Lucas, R. J. – Lall, G. S. – Allen, A. E. – Brown, T. M. (2012) *How rod, cone, and melanopsin photoreceptors come together to enlighten the mammalian circadian clock.* Progress in brain research, 199:1-18.

Lynes, J. A. (1979) *A sequence for daylighting design.* Lighting Research and Technology, Vol. 11, No. 2, pp. 102-106.

Mardaljevic, J. (2000) *Simulation of Annual Daylighting Profiles for Internal Illuminances.* Lighting Research and Technology, 32(3), pp. 111-118.

Mayer, B. – Kylling, A. (2005) *Technical note: The libRadtran software package for radiative transfer calculations – description and examples of use.* Atmospheric Chemistry and Physics, 5, 1855-1877.

Meshkov, V. V. (1957) *Osnovy svetotekhniki.* (In Russian, Basis of illuminating engineering.) State Energy Publishing House, Moscow, 352 pp.

Naeem, M. – Wilson, M. (2007) *A study of the application of the BRE Average Daylight Factor formula to rooms with window areas below the working plane.* 2nd PALENC Conference and 28th AIVC Conference on Building Low Energy Cooling and Advances Ventilation Technologies in the 21st Century, Crete, Greece, pp. 682-686.

Nagare, R. – Woo, M. – MacNaughton, P. – Plitnick, B. – Tinianov, B. – Figueiro, M. (2021) *Access to Daylight at Home Improves Circadian Alignment, Sleep, and Mental Health in Healthy Adults: A Crossover Study.* Int. J. Environmental Research and Public Health, 18, 9980.

Pierson, C. C. – Mariëlle, P. J. – Aarts, M. – Marilyne, A. (2023) *Validation of spectral simulation tools in the context of ipRGC-influenced light responses of building occupants*. Journal of Building Performance Simulation, 16:2, 179-197.

Provencio, I. – Rodriguez, I. R. – Jiang, G. – Hayes, W. P. – Moreira, E. F. – Rollag, M. D. (2000) *A Novel Human Opsin in the Inner Retina.* Journal of Neuroscience, 20(2): 600-605.

Pyeritz, R. – Korf, R. – Grody, W. (editors). (2019) *Emery and Rimoin's Principles and Practice of Medical Genetics and Genomics. Clinical Principles and Applications.* (7th Ed.). Chapter 11 – Circadian Rhythms and Disease, authors: Zhang S.L. and Sehgal A., pp. 299-314. Academic Press.

Radiance (2023) https://www.radiance-online.org/ (accessed at 22/09/2023)

Rea, M. S. – Figueiro, M. G. – Bierman, A. – Bullough, J. D. (2010) *Circadian light.* J. Circadian Rhythm, 8, pp. 1-10.

Reinhart, C. F. – LoVerso, V. R. M. (2010) *A rules of thumb-based design sequence for diffuse daylight.* Lighting Research and Technology, Vol. 42, pp. 7-31.

Saiedlue, S. – Amirazar, A. – Hu, J. – Place, W. (2019) *Assessing circadian stimulus potential of lighting systems in office buildings by simulations.* ARCC Conference Repository, pp. 719-727.

Solemma & Alertness CRC (2018) *Adaptive lighting for alertness ALFA.*

Schlangen, L. J. M. – Price, L. L. A. (2021) *The Lighting Environment, Its Metrology, and Non-visual Responses.* Frontiers in Neurology, 12:624861.

sciendo Slovak Journal of Civil Engineering

Vol. 32, 2024, No. 1, 29 – 35
DOI: 10.2478/sjce-2024-0004

ON RELATIVE SUCCESS IN OBTAINING GRANTS FOR SMART CITIES IN THE EUROPEAN UNION AND ON THE COST OF THE OUTCOME

Tomáš Koreň[1], Ondrej Gajniak[2], Matúš Kubák[3*]

Abstract

The concept of smart cities is gaining momentum with efforts to go greener and be more sustainable along with the growing demand for data-driven policies. The European Union (EU) is highly committed to fostering sustainable urban development through targeted funding programs that encourage innovation, collaboration, and practical solutions for climate-neutral and smart cities. We have used data mining on the data of the Community Research and Development Information Service (CORDIS) and Eurostat during 2014 – 2022, to analyze such projects. Firstly, we can report that in absolute measures, Germany, Spain, France, Sweden and Lithuania have obtained the largest amounts of money fromthe EU Horizon program to support the development of smart cities. Secondly, we have found that when accounting for the size of funding per capita, Estonia leads in terms of funds invested in smart cities followed by Luxembourg, the Netherlands, Finland, and Cyprus. Focusing our attention on the cost of outcomes, i.e., the efficiency of spending funds on smart cities, we can see that the leading countries in the EU are Romania, Switzerland, Norway, and Luxembourg. The authors have compared the success of European projects in their different phases, while considering the overall results as most relevant for our evaluation.

Address

[1] Dept. of Economics and Economy, University of Presov in Presov, Faculty of Management and Business, Presov, Slovakia

[2] Dept. of the Humane Sciences, Faculty of Civil Engineering, Slovak University of ˙Technology in Bratislava, Bratislava, Slovakia

[3] Dept. of Regional Science and Management, Technical University of Kosice, Faculty of Economics, Kosice, Slovakia

* ***Corresponding author:*** *matus.kubak@tuke.sk*

Key words

- Smart cities,
- Project management,
- The EU,
- Funding, Horizon,
- Success,
- Data mining.

1 BIBLIOGRAPHICAL REVIEW

The European Union is highly committed to fostering sustainable urban development through targeted funding programs that encourage innovation, collaboration, and practical solutions for climate-neutral and smart cities. The European Union is actively supporting the development of smart cities through various funding programs. One significant initiative is the Horizon Europe research and innovation program for the years 2021-2027. The EU Missions is a novel approach within Horizon Europe and aims to address pressing challenges by delivering concrete solutions and tangible results by 2030. The goal of the Cities Mission is to make cities smart and climate-neutral, as they are key to reaching climate neutrality by 2050. This is essential because most EU citizens (75%) live in cities, which only cover 4% of the EU's land area. Globally, cities are responsible for more than 70% of the CO2 emissions and use over 65% of the world's energy. The Cities Mission wants to achieve 100% smart and climate-neutral cities by 2030 and turn these cities into hubs of innovation and experimentation, thereby encouraging other European cities to do the same by 2050.

There are many funding opportunities, and the estimated budget is more than €70 million (European Commission, 2021).The European Commission has been actively supporting the development of smart cities through its Horizon 2020

research and innovation programs by which the European Commission has funded the Smart Cities and Communities Project Clusters. The aim of these clusters is to bring together various stakeholders such as cities, industry, knowledge institutes, and citizens to showcase solutions and business models that have the potential to be scaled up and replicated. The EU has supported the development of innovative solutions for cities that could improve the quality of life for citizens and tackle urban challenges by investing around €3.1 billion in research on urban sustainability and development under the Horizon 2020 programme (European Commission, 2020). The European Structural and Investment Funds, which include the European Regional Development Fund, offer financial assistance to EU regions for urban development projects, such as smart city initiatives.These funds aim to reduce regional disparities and promote sustainable growth (European Commission, 2020). Caragliu et al. (2021) have stated that the Cohesion policy also plays a significant role in funding smart cities with a focus on improving infrastructure, innovation, and environmental sustainability. The policy's goal is to enhance the economic and social integration of EU member states.

Galati (2018) argues that implementing smart cities is not inexpensive. It requires a strategic and comprehensive plan to secure funding for individual smart projects or entire programs. Investors seek a clear understanding of the potential return on their investment before committing funds. Meanwhile, municipal bodies aim to enhance technology, mobility, and system capabilities to maintain the attractiveness of their cities.

Clerici et al. (2019) note that the European perspective on smart cities encompasses diverse visions, social goals, and data-driven approaches to enhance urban living. The European vision of smart cities is not uniform; it varies based on the diverse realities and perspectives of European citizens. European cities aspire to be more than just technologically advanced, they aim to be platforms for social progress, democratic dialogue, cultural diversity, and environmental regeneration. Data-driven transition is one of the key elements in the creation of smart cities. Over the last decade, cities have transitioned toward becoming smart cities, and data from information and communication technology applications play a crucial role in understanding, analysing, and planning cities for improved efficiency and equity.

Orejón-Sánchez et al. (2022) mention generational shifts that reflect the dynamic evolution of smart cities, from technology-driven initiatives to comprehensive, multi-dimensional approaches that consider various aspects of urban life and sustainability. The main focus of current smart city concepts is the inhabitants and societal goals, and they have the following dimensions: social cohesion and governance, smart city platforms, urban planning, international outreach, software (apps and websites), mobility, technology, the environment, and human capital.

Trindade et al. (2017) tried to understand the relationship between environmental sustainability and smart city concepts. Through a systematic review of the literature, the authors examine sustainable development in smart cities and provided the baseline idea that smart cities emerge from the intelligent use of digital information across various domains (health, mobility, energy, education, governance) and that sustainable urban development aims at the use of renewable resources within smart cities. Their review sheds light on the intersection of smart cities and sustainability, thereby providing valuable knowledge for future research and practical implementation.

The concept of an integrated smart city has been explored by Attaran et al. (2022). They claim that current smart city models do not have ideal solutions for integration and that aspects such as security and the information and communications technology infrastructure (ICT), created in a society are not fully incorporated. They suggested that new sub-components and extra-components are required for a comprehensive structure. They introduced an improved general model with six components: smart people, smart government, smart environment, smart transportation, smart economy, and smart life. These components are meant to ensure the integrity, dynamism, flexibility, and performance of a smart city, as well as to facilitate life cycle management and enable the better prediction and prevention of events such as natural disasters and pandemics. The model aims to address the integration challenges for sustainable urban development.

Javidroozi et al. (2023) has run an extensive review of smart, sustainable, and green cities and declares that smart cities should be integrated and collaborative. Their key points include a shared vision of all stakeholders, an integrated creative approach based on urban planning that fosters synergies across sectors and minimizes negative trade-offs, societal well-being and equity, and the incorporation of a green and blue infrastructure. Public–private partnerships can secure resources for smart, sustainable, and green city initiatives. Myeong et al. (2022) provides a comprehensive analysis of smart city research over the past decade (from 2011 to 2020). The authors emphasize that rapid urbanization has intensified the need for smart cities that can tackle problems invovlving transportation, the environment, welfare, the economy, safety, energy, and resource distribution. They note that future cities can benefit from data-driven applications for performance efficiencies, climate mitigation, and the well-being of citizens. Furthermore, by using data innovations, workplace paradigms and environmental biodiversity can be stimulated. Addressing security and privacy concerns is critical for responsible data handling, digital literacy, and online connectivity. Access to real-time data is crucial, especially during pandemics and other disasters.

2 INTRODUCTION

Smart cities have acquired a higher degree of relevancy since the technology has become a greater part of our lives. In recent years, governments, researchers, and the private sector have been investing heavily in smart cities. Ismagilova et al. (2019) has noted that smart cities are gaining in importance because of the rapid growth of the population in today's cities in a close connection with persistent advances in technology. Thanks to the increasing annual expenses of the municipalities themselves, which are cofinanced directly from state budgets or from the budgets of supranational entities with the generous cooperation of the private sector, there is an acute need for systematic research into the concept of smart cities, which can lead to the further development of this concept.

2.1 Characteristics and definitions of a smart city

With the growing role of contemporary cities as well as the irreplaceable role of technology in our lives, the concept of "smart cities" is gaining public attention. According to the European Commission, a "smart city" is a place where traditional networks and services are made more efficient with the use of digital solutions for the benefit of its inhabitants and businesses. A smart city goes beyond the use of digital technologies for better resource use and fewer emissions. It means smarter urban transport networks, upgraded water supply and waste disposal facilities, and more efficient ways to light and heat buildings. It also means a more interactive and responsive city administration, safer public spaces and meeting the needs of an aging population" (European Commission, 2023). Countless smart city definitions can be divided into groups according to the professional focus of a specific group; nevertheless, we still lack a definition of a smart city that legally matters. This term is currently more prevalent in technical and economic fields of the sciences than in terminology intended for the legal sector.

There is an approach to constructing smart city definitions on various bases that give information and communication technology an irreplaceable role in constructing and connecting other functional qualities of a smart city, such as the joint definition from the International Organization for Standardization and the International Electrotechnical Commission: "An innovative city that uses information and communication technologies (ICT) and other means to improve the quality of life, the efficiency of urban operations and services, and competitiveness, while ensuring that it meets the needs of present and future generations with respect to economic, social, environmental as well as cultural aspects" (The International Organization for Standardization, 2014).

Caragliu et al. (2009) adds another holistic definition, which highlights other tools and characteristics of the conceptualization of a smart city, while maintaining the importance of ICT, stating that an urban area might be determined to be "smart" when factors like human and social capital with the modern ICT drive for economic growth, which is sustainable and has a good quality of life, is coupled with a clever management of resources on the one hand and collective participatory governance on the other hand.

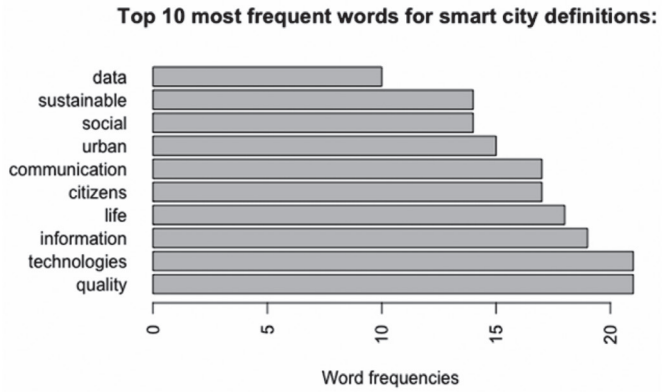

Fig. 1 *Word Frequency Plot Generated Using Compiled List of Smart City Definitions*
Source:https://doi.org/10.3390/smartcities6040080

According to Gracias et al. (2023), the results of the word cloud analysis shown in Figure 1 clearly demonstrate that the quality of life for inhabitants in cities is a criterium whitch plays a significant role when creating smart city definitions.

The leading position of the placement of the terms "technology" and "information" in Figure 1 highlights the importance of ICT as a primary factor in the implementation of smart city projects. Despite the unequivocal prevalence of individual terms in smart city definitions from different authors across the smart city sector, according to the subject analysis conducted by Gracias et al. (2023), smart cities lack a generally worldwide recognized definition.

2.2 Smart cities in the context of global investment

Even though the division of the investment domains of the smart city concept varies from source to source, we can state in general that the development and implementation of the smart city initiatives typically require significant investments in several areas. According to www.statista.com, "the global smart city market value will be worth approximately $1.38 trillion by 2030, while in 2019, it was only $392.9 billion" (Statista, 2021). Over the last ten years the European Union has distributed 1.32 billion EUR via its funding programmes into various smart city projects totalling 1.77 billion EUR overall investments (European Commission, 2023). The scale and scope of the investment can vary significantly, based on the size of the city, its existing infrastructure, the specific technologies being implemented, and the extent of integration. Governmental funding, private sector partnerships, and public-private collaborations often play a significant position in financing smart city projects. The long-term benefits of such investments are typically seen in the increased efficiency of city administrations on the one hand, thereby leading to improved public services, coupled with a better and healthier life for its residents on the other hand. Furthermore, net zero plays a central role in smart city projects and their further development. The European Commission has revealed a mission platform, the main objective of which is to prepare and accomplish 100 net zero smart cities by no later than 2030. There has already been a selection of 100 cities in the EU and 12 other cities in countries associated with Horizon Europe aiming for net zero by 2030, involving the testing of multi-sectoral approaches and applying the stakeholder engagement and management model whilst internally governed. Looking to the future, successful smart cities will play the role of innovative centres and will spread their innovations among the other European cities to achieve climate neutrality by 2050, which is the main goal of the European Green Deal (European Commission, 2023). Investments in large smart city projects require careful planning, strategic partnerships, and the prioritization of key areas to achieve success.

2.3 Smart city rankings and their meaning in smart city funding

With the rise of the smart cities concept and the subsequent competition for funds that flow from various sources, the level of the smartness of cities based on various rankings

has experienced a boom and attracted the attention of professionals from this area as well as the general public. There are countless ways as to how to evaluate smart city models, as well as a wide range of outputs from evaluations anchored in the form of smart city rankings. The methodology for ranking smart cities varies, depending on the organization conducting the rankings or the study.

For instance, the IESE Business School's Center for Globalization and Strategy looked at 174 cities around the world and analyzed them across nine metrics: "human capital, social cohesion, the economy, the environment, governance, urban planning, outreach technology, and mobility" (IESE Business School's Center for Globalization and Strategy, University of Navara, Spain 2023).

Similarly, the Smart Cities Index Report 2022 analyzed 31 smart cities using categories such as "service innovation, urban intelligence, urban sustainability, urban openness, infrastructure integration, urban innovativeness, collaborative partnerships, and smart city governance" (Institute for Manufacturing, University of Cambridge, and Digital Transformation Research Center at Yonsei University, China 2022).

Respectively, the smart city evaluation model developed by a team of scientists from Techniche Universität WIEN, Delft University of Technology, and the University of Ljubljana is based on an evaluation of 6 main areas, i.e., "the smart economy, smart people, smart governance, smart mobility, a smart environment, and smart living" (Techniche Universitat WIEN, Delft University of Technology, University of Ljubljana, 2023).

We believe that the importance of a place in the smart city rankings is self-contained at this time and that the potential value of creating smart city rankings is not used when allocating funds. This is also probably because no official and legally recognized smart city evaluation model can be found, where it would be possible to derive a legally recognized entitlement to the allocation of grant funds, or at least, the data of which could serve as one of the criteria for an entitlement to funding from public sources intended for the concept of smart cities.

As can be understood from the Horizon 2020 factsheet, the ability to seek funding and the allocation of funds for the smart cities sector is mostly based on the quality of a city's proposal, the project's feasibility, the projected costs or fullfilling other prescribed criteria, rather than the city's smartness ranking. We are not aware of any direct connection between the overall smart city rankings and the allocation of funds intended for smart cities (European Commission, 2020).

3 MATERIAL AND METHODS

In our analysis we applied data mining methods based on the Community Research and Development Information Service (CORDIS) and Eurostat databases. CORDIS is the European Commission's main public portal and repository for disseminating information on funded EU research projects and their results. CORDIS belongs to the Research and Innovation community platform of the European Commission and complements the Funding and Tender Opportunities website, where one can apply for funding and search for partners (European Commission, CORDIS, 2023).

The Cordis database contains broad datasets, such as those containing past funding programmes (e.g. FP7), data for non-member participating countries, and all kinds of domains driven by EU programmes. Therefore, our data selection had to be narrowed as follows:

- Funded and finished smart city projects
- Horizon 2020 and Horizon Europe
- Full years 2014 - 2022
- 28 EU member countries (but including Great Britain as well until 2022)
- Population data taken from Eurostat (European Commission, Eurostat, 2023)

4 RESULTS

Over the last decade some 319 smart city projects, representing 1.43% of all programme funding, have been financed by the EU Horizon funding programmes. This represents a group of nearly 3400 participants including SMEs, NGOs, academia, public organizations, and other institutions actively involved in smart city research and innovation projects. Fig-

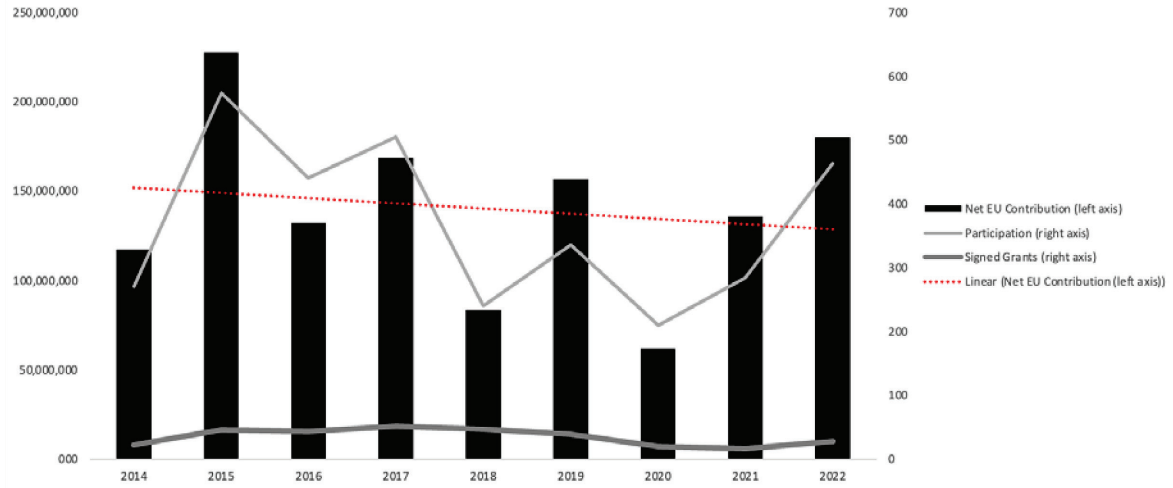

Fig. 2 *EU-funded smart city projects over the last 10 years*

ure 2 shows the distribution of net EU contributions as well as the amount of signed grants for the years 2014-2022 for two programmes, i.e., HORIZON EUROPE and H2020. Their evolution over the last ten years indicates relatively stable EU contributions with a correlating trend for signed grants. The years 2014 – 2021 represent the Horizon 2020 funding period, while 2022 marks the starting year of Horizon Europe. While 2015 was the strongest year in terms of EU smart city project contributions, the Covid-impacted year 2020 had the lowest level of EU funding.

4.1 Overall project success does not equal funding success

It should not come as a surprise that the largest EU economies such as Germany, Spain, the Netherlands, France, and Italy account for more than half (59%) of the Horizon funding awarded in the smart city domain. To put these figures into a broader perspective, we have added a "per capita" view, which changes the country ranking (Figure 3). Leaving all countries but the Netherlands out of the top 5 list and considering the size of funding per capita, Estonia leads the ranking with a solid 22.18 EUR contribution per citizen, followed by Luxembourg (10.81 EUR) and the Netherlands (8.16 EUR). These statistics indicate that large countries have a higher critical mass by imposing stronger penetration in EU projects while consuming a larger portion of the EU funding. From that perspective such countries can be seen as more successful, while underrepresented countries are less successful, since the first group deliver better results at the funding stage of projects and thus receive more funding for smart cities as a whole. In our view, however, it would be beneficial to increase visibility of the overall smart city project outcomes and results, i.e., in their final stage.

To provide a way forward, we decided to link project management perspectives to the rate of success. Instead of evaluating smart city projects as success-based relative to funding consumed (the participant's view), we aimed to analyze success through the optics of delivered project results and outcomes (the sponsor's view). It is important to note, that from a funding perspective, all the projects delivered might be seen as successful, assuming that the project grant has been consumed and maintained by the participants after the project has finished. Nevertheless, we are arguing that despite all 319 projects being funded in the end, the smart city projects analyzed should not be seen as equally successful. In this paper we provide a simplified framework for understanding the differences in success on a ranking scale. In our model, we have considered the following delivered outcomes as project success criteria for 319 smart city projects:

- Amount of intellectual property rights: patents, trademarks
- Number of scientific publications: book chapters, peer reviewed articles
- Number of deliverables: demonstrators' pilots, prototypes, websites
- Amount of project reports: periodic report summaries, etc.

As our model incorporates a project management context, two major success milestones will be analysed: (M1) funding success - a participant's view, and (M2) outcome success – a sponsor's view. A comparison of the M1 and M2 results leads us to the following research questions:

1) What is the level of success when measured in the funding stage of a project?
2) What is the level of success in the outcome stage of a project?
3) Can all SMART CITY PROJECTS funded be considered equally successful?
4) How can the success of SMART CITY PROJECTS be measured?

To provide perspectives to the above research questions, we refer the reader to Tables 1 and 2, which prove that a higher success rate of reaching the SMART CITY PROJECTS´ funding milestone will not correspond to the same success rate of delivered project results. Therefore, all the funded projects cannot be seen as equally successful. Applying the cost of outcomes in our model should help us understand the price EU

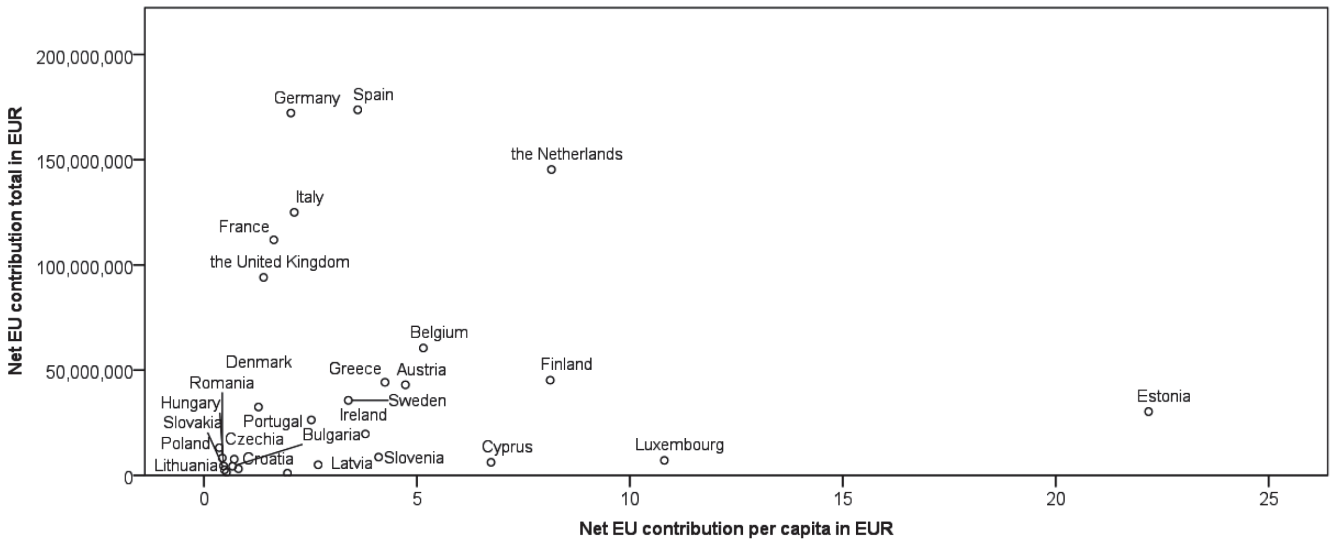

Fig. 3 *Net EU contributions in absolute and relative measures*

taxpayers have to pay for delivered smart city projects. The cost of the outcome has the following formula:

$$Cost\ of\ outcome\ = \frac{ecMaxContribution}{(Patents + Deliverables + Publications)} \quad (1)$$

In that sense, projects with the lowest outcome cost can be seen as more efficient and thus more successful (Table 2).

While Table 1 ranks countries by the amount of SMART CITY PROJECTS funding, sorting the same dataset by the Cost of Outcome (Table 2) changes the ranking significantly, i.e., the leading countries now become Romania, Switzerland, and Norway, while Germany and Spain leave the top 10 list completely. It is interesting to note that low-cost countries do not necessarily top the list.

5 CONCLUSION

Despite the growing importance of smart cities in the context of net zero goals, the net EU contribution in the last ten years has been rather stable, i.e., showing an increase in the recent years of 2021 and 2022. The importance of smart cities, coupled with the relatively low visibility of EU-funded project successes, has motivated us to deepdive into differences among member countries participating in SMART CITY PROJECTS. Even though all the funded projects are deemed more or less successful from a Horizon point of view, it is not clear how they perform after post-funding or how they perform relative to each other. Therefore, we decided to apply project success analyses to help us find subtle differences in terms of project results and their success as such. Currently, the EU Commission reports on project results in a somewhat limited way, such as listing only limited types of results (deliverables, publications, project websites or patents), while leaving the commercial point of view completely out of the equation. Having a higher visibility of the commercial and industrial impacts such as the improvement in the technological readiness level before/after a project, market share, the amount of customers, post-project activity, etc., would probably make the outcomes more transparent to EU taxpayers. We also hypothesize that a higher degree of transparency could lead to more efficient smart city project governance while opening new opportunities for researchers, policymakers, and potential project participants in this domain. Horizon might foster this by delivering more specific success information such as results-oriented project reporting, success KPIs on dedicated Horizon dashboards, and extended datasets.

We have recognized a few limitations in our analysis that require further attention. The first downside is the relatively low availability of commercial and industrial project results.

Tab. 1 *Total contribution by country*

Rank	Country	Projects	ecMaxContribution	Deliverables	Publications	Patents	Cost of outcome
1	Germany	19	105,902,015	409	624	1	102,420
2	Spain	33	86,923,889	348	216	3	153,305
3	France	19	53,488,379	212	297	2	104,674
4	Sweden	10	29,266,015	93	47	0	209,043
5	Lithuania	7	27,549,917	114	231	9	77,825
6	Italy	19	26,476,447	203	222	0	62,298
7	Denmark	3	24,744,149	78	111	0	130,921
8	the United Kingdom	13	15,623,913	138	140	2	55,800
9	Finland	3	12,767,625	100	62	0	78,813
10	Norway	4	10,085,201	116	108	0	45,023

Tab. 2 *Cost of outcome*

Rank	Country	Projects	ecMaxContribution	Deliverables	Publications	Patents	Cost of outcome
1	Romania	2	1,496,610	14	176	2	7,795
2	Switzerland	10	4,585,583	68	59	0	36,107
3	Norway	4	10,085,201	116	108	0	45,023
4	the United Kingdom	13	15,623,913	138	140	2	55,800
5	Luxembourg	2	3,624,795	1	61	0	58,464
6	Italy	19	26,476,447	203	222	0	62,298
7	Belgium	4	8,459,890	63	64	0	66,613
8	the Netherlands	6	10,072,340	52	78	0	77,480
9	Lithuania	7	27,549,917	114	231	9	77,825
10	Finland	3	12,767,625	100	62	0	78,813

Acquiring such data will require in-depth data mining for projects that continue to exist beyond their funding life cycle. The second issue we recognize is the dimension of quality, which should be taken into consideration when talking about results. This could be the impact factor of published articles, the number of citations to publications, etc., to name a few. A further investigation could involve adjusting the cost of outcome indicators to various price levels in EU countries, particularly the costs per person-month. We plan to address these opportunities in a follow-up study with the application of more robust econometric models.

Acknowledgments

The work was supported by the The Slovak Research and Development Agency Grant No. APVV-22-0090 - Application of behavioral economics in the mapping of preferences in the areas of housing, employment and transport mobility.

REFERENCES

Attaran, H. - Kheibari, N. - Bahrepour, D. (2022) *Toward integrated smart city: a new model for implementation and design challenges*. GeoJournal 87 (Suppl 4), pp. 511–526 https://doi.org/10.1007/s10708-021-10560-w

Clerici, P. - Civiero, M. P. - Gilda, M. (2019) *European Union Funding Research Development and Innovation Projects on Smart Cities: The state of the art in 2019*. International Journal of Sustainable Energy Planning and Management, pp. 24. https://doi.org/10.5278/ijsepm.3493

Caragliu, A. - Del Bo, C. - Nijkamp, P. (2011) *Smart Cities in Europe*. Journal of Urban Technology, 18:2, pp. 65-82, DOI: 10.1080/10630732.2011.601117

European Commission (2023) *CORDIS*, Available: https://cordis.europa.eu/

European Commission (2023) *Horizon Dashboard – Key Figures*, Available: https://dashboard.tech.ec.europa.eu/qs_digit_dashboard_mt/public/sense/app/d58f3864-d519-4f9f-855e-c34f9860acdd/sheet/KVdtQ/state/analysis

European Commission (2020) *H2020 FACT SHEETS*, Available: https://ec.europa.eu/research/participants/data/ref/h2020/other/gm/h2020-grant-factsheet_en.pdf

European Commission (2023) *SMART CITIES*, Available:https://commission.europa.eu/eu-regional-and-urban-development/topics/cities-and-urban-development/city-initiatives/smart-cities_en

European Commission (2023) *Innovating cities*, Available: https://research-and-innovation.ec.europa.eu/research-area/environment/urban-development/innovating-cities_en

European Commission (2023) *EU Mission: Climate-Neutral and Smart Cities*, Available: https://research-and-innovation.ec.europa.eu/funding/funding-opportunities/funding-programmes-and-open-calls/horizon-europe/eu-missions-horizon-europe/climate-neutral-and-smart-cities_en

European Commission (2023) *Eurostat*, Available: https://ec.europa.eu/eurostat

European Commission (2023) *Ten European cities awarded with EU Mission Label for their plans to reach climate-neutrality by 2030*, Available:https://ec.europa.eu/commission/presscorner/detail/en/IP_23_4879

Galati, S.R. (2018) *Funding a Smart City: From Concept to Actuality.* In: McClellan, S., Jimenez, J., Koutitas, G. (eds) Smart Cities. Springer, Cham. https://doi.org/10.1007/978-3-319-59381-4_2

Gracias, J.S. - Parnell, G.S. - Specking, E. - Pohl, E.A. - Buchanan, R. (2023) *Smart Cities - A Structured Literature Review*. https://doi.org/10.3390/smartcities6040080

IESE Business School's Center for Globalization and Strategy, University of Navara (2023) *IESE Cities in Motion Index*, Available: https://worldpopulationreview.com/world-city-rankings/smart-cities

International Organization for Standardization (2014) *Smart Cities Preliminary Report 2014*,Available:https://www.iso.org/files/live/sites/isoorg/files/developing_standards/docs/en/smart_cities_report-jtc1.pdf

Institute for Manufacturing, University of Cambridge and Digital Transformation Research Center at Yonsei University (2022) *Smart Cities Index Report 2022*, Available: https://smartcitiesindex.org/smartcitiesindexreport2022

Ismagilova, E. - Hughes, L. - Dwivedi, Y.K. - Raman, K.R. (2019) *Smart cities: Advances in research—An information systems perspective*. Int. J. Inf. Manag., 47, pp. 88–100 https://doi. org/10.1016/j.ijinfomgt.2019.01.004

Javidroozi, V. - Carter, C. - Grace, M. - Shah, H. (2023) *Smart, Sustainable, Green Cities: A State-of-the-Art Review.* Sustainability 2023, 15, 5353. https://doi.org/10.3390/su15065353

Myeong, S. - Park, J. - Lee, M. (2022) *Research Models and Methodologies on the Smart City: A Systematic Literature Review*. Sustainability 2022, 14, 1687. https://doi.org/10.3390/su14031687

Orejon-Sanchez, R. D. - Crespo-Garcia, D. - Andres-Diaz, J.R. - Gago-Calderon, A. (2022) *Smart cities' development in Spain: A comparison of technical and social indicators with reference to European cities, Sustainable Cities and Society*, Vol. 81, ISSN 2210-6707, https://doi.org/10.1016/j.scs.2022.103828.

Techniche Universität WIEN, Delft University of Technology and University of Ljublana (2023) *EUROPEAN SMART CITY: SMART CITY MODEL*, Available: https://www.smart-cities.eu/model.html

Trindade, E.P. - Hinnig, M.P.F. - da Costa, E.M. (2017) *Sustainable development of smart cities: a systematic review of the literature*, Available: https://doi.org/10.1186/s40852-017-0063-2

Statista (2023) *Size of smart cities market worldwide in 2019 and 2030*, Available:https://www.statista.com/statistics/1256262/worldwide-smart-city-market-revenues/

sciendo Slovak Journal of Civil Engineering

Vol. 32, 2024, No. 1, 36 – 45
DOI: 10.2478/sjce-2024-0005

CALIBRATION OF HYPOPLASTIC PARAMETERS FOR DANUBE SAND

Amir Mosallaei[1]*, András Mahler[1]

Abstract

The relationship between stress and strain tensors in soil is described by the soil constitutive equation, which depends on the soil type and deformation conditions. The development of various constitutive models has enabled a better understanding of the macromechanical properties of soil. One such model is hypoplasticity, which was discovered more than three decades ago. The purpose of this study is to determine whether hypoplasticity could accurately represent the behavior of Danube sand, a specific type of sand. The researchers conducted laboratory measurements to obtain the eight basic hypoplastic parameters of Danube sand and employed the intergranular strain concept as an extension of hypoplasticity to achieve a more precise material behavior. All the parameters were then utilized to simulate the cyclic triaxial test using the SoilTest Module of PLAXIS. The results showed that the hypoplastic constitutive simulation model for Danube sand was capable of making relatively accurate predictions for accumulative settlement.

Address

[1] Dept. of Engineering Geology and Geotechnics, Budapest University of Technology and Economics, Budapest, Hungary

* ***Corresponding author:*** mosallaei@edu.bme.hu

Key words

- Hypoplasticity,
- Intergranular strain,
- Cyclic triaxial test,
- Coarse-grained soil,
- Constitutive model.

1 INTRODUCTION

In recent decades, various numerical techniques have been developed to model soil behavior under static and cyclic loads. A suitable constitutive model must be used to effectively depict the interaction between soil and structures, especially in the case of geotechnical structures on water-saturated soils subjected to cyclic stress. The Mohr-Coulomb frictional constitutive model is often used, but it fails to account for the complex historical dependence of soil behavior. Therefore, more advanced models, such as the hypoplastic constitutive model with a critical state, have been proposed. The calibration of these models requires high-quality cyclic laboratory tests with a variety of boundary conditions (Gajári et al., 2021; Niemunis et al., 2005; Stutz et al., 2017a; Wei and Yang, 2020; Wichtmann and Triantafyllidis, 2018; Wu et al., 2017).

In this paper, the hypoplasticity parameters of Danube sand are calibrated to obtain an accurate set of soil properties for simulating pavement-subsoil interactions. It is important to consider the accumulation of cyclic traffic loads and residual stresses, which can cause tensile cracks in asphalt. Moreover, cyclic loading can cause irreversible strains and excessive pore pressure, leading to soil liquefaction and loss of overall stability. Therefore, the accumulation strain phenomenon is of practical importance.

1.1 Hypoplasticity and its basis

By defining the relationship between stress and strain through mathematical equations, constitutive laws are responsible for describing how materials deform. Various mathematical equations have been developed to describe the deformation behavior of soil. Hypoplastic equations,

which are based on non-linear tensor functions, have proven to be particularly useful for modeling granular soils (von Wolffersdorff, 1996). Unlike plasticity-based equations, hypoplastic equations do not rely on yield surfaces or the decomposition of a strain into elastic and plastic components, thereby resulting in simpler initial formulations with fewer parameters. These equations can also account for the effects of pressure and density changes and can be validated through laboratory tests. Over time, hypoplastic equations have been improved to include additional state variables, such as porosity, and can be determined through lab tests. The stress tensor is the only state variable in the basic hypoplastic equations (Bauer et al., 2020; Fellin, 2002; Wang and Wu, 2020).

Initially, the hypoplastic state equation only considered the stress tensor as a variable, and the basic hypoplastic equations included four polynomial expressions, four material characteristic coefficients, two linear coefficients, and two nonlinear coefficients to describe the strain rate. Over time, improvements were made to hypoplastic equations by adding a new state variable, i.e., porosity. The advantage of hypoplastic equations is that the main parameters can be obtained through triaxial equipment. The stress tensor remains the only state variable in the basic hypoplastic equations (Wu et al., 2017).

The hypoplastic behavior model has been extensively used to study the behavior of sandy soils and has been shown to accurately express uniform settlement. It can even be used for soft soils with a high internal friction angle. However, when using the hypoplastic behavior model for clay soils, the stiffness of the modeled soil is much lower than in reality (Herle and Kolymbas, 2004).

The hypoplastic model correctly predicts the arrangement of the grain skeleton causing sediment deformation, density, and pressure using material constants and a simple formula. However, without an intergranular strain (IS) parameter, it cannot predict soil behavior in certain cases, such as the soil‘s initial high degree of stiffness and cumulative plastic deformations generated by small stress loading cycles (Herle and Gudehus, 1999; Kolymbas and Wu, 1990; Mohammadi-Haji and Ardakani, 2020).

Model parameters for granular materials should directly depend on grain properties, such as shape, angularity, size distribution, and the friction coefficient, as well as the grain’s hardness or strength. However, determining these parameters from experimental investigations of single grains is not realistic (Herle and Gudehus, 1999).

2 METHODS ANDS PARAMETERS

The behavior of granular soils under a load is primarily determined by their stress level. As a confining pressure increases, the maximum shear strength of granular soils typically increases, while residual shear strength and stiffness may also increase or remain relatively constant, depending on the specific material properties and conditions. Cumulative deformation is a major concern for the long-term serviceability of structures susceptible to differential defor-mation. “Hypoplasticity” is a model used to describe the behavior of sand, which does not require a yield surface or other elements related to elastoplasticity. Wu and Bauer (1994) proposed a four-parameter model that could describe various characteristics of sand in both drained and undrained states. Niemunis and Herle (1997) presented the formulation of small strain stiffness, while Poblete et al., (2016) proposed the framework of intergranular strain anisotropy (ISA), which allows for improved model performance under cyclic loading conditions, such as memory effects and increased stiffness upon stress reversal (Mohammadi-Haji and Ardakani, 2020; Moussa et al., 2020; Yang et al., 2020).

2.1 Basic parameters

The hypoplastic model for sand is comprised of eight parameters, which can be divided into

four major categories. The first category pertains to the critical friction angle, denoted as φ_c.

The second category includes two parameters, i.e., h_s, which stands for granular stiffness, and n, which serves as an exponent for h_s. The third category is dedicated to various types of void ratios, where e_{d0} represents the minimum void ratio at zero pressure; e_{c0} represents the critical void ratio at zero pressure; and e_{i0} represents the maximum void ratio at zero pressure. The fourth and final category encompasses the last two parameters, α and β, which respectively impact the peak of the friction angle and control the stiffness. Wolffersdorff‘s hypoplastic model is used in this paper (von Wolffersdorff, 1996).

2.1.1 Friction Angle φ_c of the Critical State

The parameter φ_c represents the critical angle of internal friction, which is a fundamental parameter in soil mechanics and geotechnical engineering. It describes the minimum angle at which a soil mass will fail or slide under shear stress and determines the soil‘s shear strength. The critical friction angle varies, depending on the soil type and state of stress and can be determined through laboratory and field tests.

Herle and Gudehus (1999) showed that the angle of repose measured on a dry granular soil provides a good estimate of the critical friction angle determined through shear box measurements.

In coarse-grained soils, the angle of repose test is a straightforward method for determining φ_c. However, for soils with a larger proportion of fine grains, triaxial shear tests on normally consolidated samples are recommended.

Soil, typically reaches its critical state under monotonic shear loading when the volumetric deformation rate stabilizes while maintaining a constant mean stress. Triaxial tests are commonly used to determine the critical state.

Tab. 1 *Critical friction angle from angles of repose and from shear tests (Herle and Gudehus, 1999)*

Material	Hochstetten gravel	Hochstetten sand	Hostun sand	Karlsruhe sand	Lausitz sand	Toyoura sand	Zbraslav sand
Angle of repose	35.7	34	32	29.1	33	30.4	30.8
φ_c	36.5	34	32	30	32.2	30.9	29.7

2.1.2 Granulate Hardness (h_s) and exponent (n)

The term „granulate hardness“ refers to the extent of resistance or firmness displayed by granular materials when subjected to an applied force or load. The measurement of granulate hardness is valuable for gathering information on the particle size distribution, packing density, and flow characteristics of the material, which can aid in optimizing handling and processing operations. Various techniques, such as penetrometers, compressive testing, and shear testing, are available for measuring granulate hardness.

Granular hardness (h_s) is the only parameter that measures stress and should not be confused with the hardness of individual grains. The exponent „n“ accounts for the pressure-sensitivity of the grain skeleton, allowing for a non-proportional increase in incremental stiffness with increasing pressure. An oedometer test is a simpler way of determining “h_s” and “n”. Directly obtaining “h_s” and “n” from measured data is not recommended due to strong non-linearity. The knowledge of “n” is necessary for determining “h_s”, but “n” can be calculated independently of “h_s”. An oedometric test can replace isotropic compression for calibration asit is easier to perform and allows for reaching higher pressure, as “h_s” and “n” control the slope and curvature of the compression line, respectively.

Performing an oedometer test and plotting the compression curve yields a graph similar to Figure 1, which represents a schematic of the compression curve. The calculation of the exponent „n“ is the first step, as it is not dependent on the parameter „h_s,“ which is absent in Equation 1. The determination of „n“ is crucial in determining „h_s,“ which can be calculated using Equation 2. Thus, the value of „h_s“ depends on knowledge of „n.“

$$n = \frac{\ln\left(\frac{e_{p1}\times c_{c2}}{e_{p2}\times c_{c1}}\right)}{\ln\left(\frac{p_{s2}}{p_{s1}}\right)} \tag{1}$$

$$h_s = 3 \times p \times \left(\frac{n\times e}{c_c}\right)^{\frac{1}{n}} \tag{2}$$

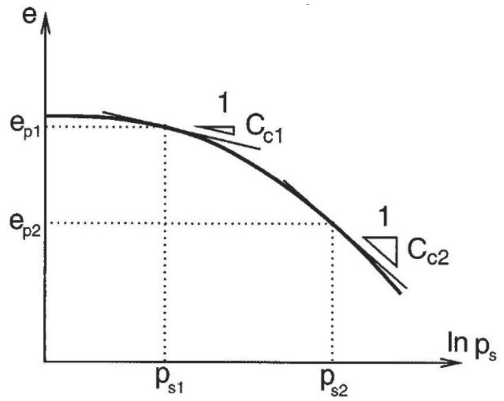

Fig. 1 *Schematic of compression curve (Herle and Gudehus, 1999)*

2.1.3 Minimum e_{d0}, critical e_{c0}, and maximum e_{i0} of a void ratio at zero pressure

Generally, the most effective way to achieve the optimal compaction of a granular soil is by applying cyclic shearing with a small amplitude under constant pressure. When this technique is implemented following static compression, it will gradually approach a minimum void ratio e_d, which decreases with increasing pressure. Equation 3 below can be used to describe the relationship between e_d and p_s, enabling the extrapolation of the value of e_d at zero pressure.

$$\boldsymbol{e_{d0} = e_d\, exp\left[\left(\frac{3p_s}{h_s}\right)^n\right]} \tag{3}$$

Typically, a minimum void ratio (e_{min}) is determined using index tests outlined in several standards. However, these tests are not as efficient as cyclic shearing. As a result, the measured value of e_{min} may be higher than that of e_d. Upon comparing e_{d0} with e_{min}, it is determined that they are relatively similar, with e_{min} being slightly higher than e_{d0}. Therefore, in the absence of data for e_{d0}, e_{min} can be used as a substitute (Herle and Gudehus, 1999).

Similarly to e_{d0}, the critical void ratio value at zero pressure can be computed using equation 4 below:

$$\boldsymbol{e_{c0} = e_c\, exp\left[\left(\frac{3p_s}{h_s}\right)^n\right]} \tag{4}$$

The parameter e_c can be determined through a shear test on a soil element while calculating φ_c. An undrained triaxial test is usually sufficient for establishing e_c. It has been noted that the value of e_{c0} is comparable to e_{max}.

Previously, Herle and Gudehus (1999) indicated a narrow range of 0.52 to 0.64 for the ratio of e_{d0}/e_{c0}. Mašín (2019) also proposed an empirical formula of e_{d0}=0.5*e_{c0} to be used when experimental data is not available. Tables 2 and 3 include 39 sets of hypoplastic parameters obtained from previous investigations. Based on Tables 2 and 3, the range for the aforementioned ratio is 0.37 to 0.77, with an average ratio of 0.56, which is very similar to the earlier empirical formula.

The parameter e_{i0} represents the highest possible void ratio of a basic grain skeleton achieved during an isotropic consolidation of a grain suspension in an environment without gravity. There are several ways to determine the maximum void ratio e_{max} in the laboratory, with most standards involving pouring dry soil into a calibrated mold. However, the soil often reaches a critical state during pouring, which is denser than the theoretical e_{max}. While the maximum void ratio in a gravity-free space is proposed, it cannot be measured in a laboratory. Herle and Gudehus (1999) discovered that for spherical grains, this value is 1.2 times the emax, while for cube grains, it is 1.3 times the e_{max}.

By examining Tables 2 and 3, it can be observed that the ratio of e_{i0} to e_{c0} is generally less than 1.3, and sometimes even less than 1.2. The average value for this parameter is 1.14.

2.1.4 Exponents α and β

The stiffness and pyknotropy factors are controlled by parameters α and β, which can be determined through a parametric study involving simulations of the triaxial shear test. To obtain α, Herle and Gudehus (1999) suggested using equation (2) and considering the peak state in a triaxial compression test.

$$\alpha = \frac{\ln\left[6\times\frac{(2+K_P)^2+a^2K_P(K_P-1-\tan\nu_P)}{a(2+K_P)(5K_P-2)\sqrt{4+2(1+\tan\nu_P)^2}}\right]}{\ln\frac{e-e_d}{e_c-e_d}} \tag{6}$$

Equation 6 above involves K_p, a and tan(ν_p), which can be calculated using equations 7, 8, and 9 below, respectively.

$$K_P = \frac{1+\sin\varphi_P}{1-\sin\varphi_P} \quad (7)$$

$$a = \frac{\sqrt{3}(3-\sin\varphi_c)}{2\sqrt{2}\sin\varphi_c} \quad (8)$$

$$\tan\nu_P = 2\frac{K_P-4+5AK_P{}^2-2AK_P}{(5K_P-2)(1+2A)} - 1 \quad (9)$$

To determine tan(ν_P), equation 10 can be used to calculate parameter A. An evaluation of α and β requires knowledge of these preceding parameters.

$$A = \frac{a^2}{(2+K_P)^2}\left[1 - \frac{K_p(4-K_P)}{5K_P-2}\right] \quad (10)$$

The parameter β is significant only when the void ratio e is significantly lower than the initial void ratio e_i. According to Herle and Gudehus (1999), for natural sands, assuming β = 1 is usually adequate, regardless of granulometric properties. However, among the 38 data sets in Tables 2 and 3, it can be observed that only 10 out of 38 have a value of 1 for β, while the β parameter for the remaining sets is greater than 1.

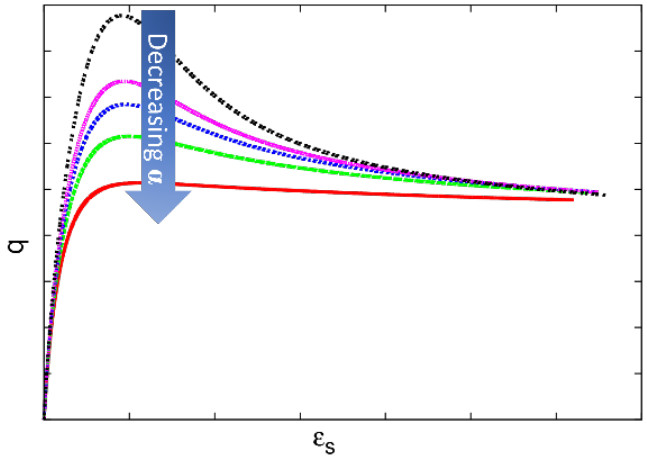

Fig. 2 *Effect of α on the peak of a stress- strain curve (Mašín, 2015)*

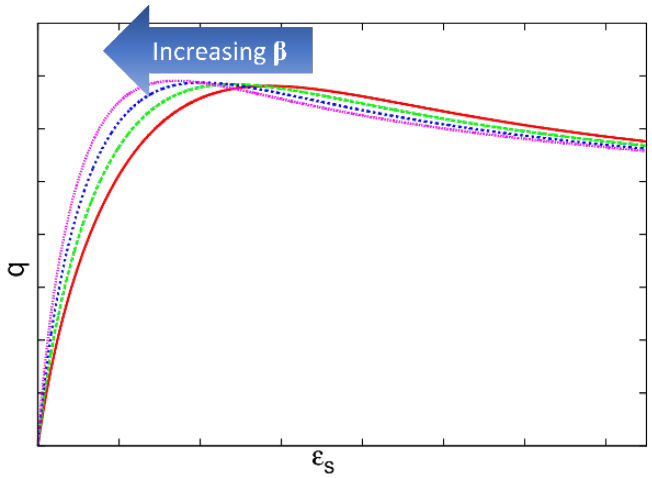

Fig. 3 *Effect of β on the peak of a stress-strain curve (Mašín, 2015)*

The impact of the α and β parameters on stress-strain curves can be understood through Figures 2 and 3. A drained triaxial test on a dense sample and curve simulation using various amounts of α can be conducted to calibrate these parameters. Fitting the resulting curves will yield the optimal value for α. Figure 2 shows that increasing α decreases the stress peak on the stress- strain curve, while Figure 3 shows β changes the location of the peak by reducing the strain value and shifting the peak to the left.

2.2 Intergranular strain parameters

Basic hypoplastic models are inadequate in predicting high initial stiffness and ratcheting, which is the accumulation of strains in stress cycles and stresses in strain cycles. The intergranular strain concept is the most widely-used approach for overcoming this limitation (Niemunis and Herle, 1997). The ISA theory provides a useful mathematical platform for developing constitutive models to simulate cyclic loading in soils by considering the effect of recent strain history. The intergranular strain evolution equation is elasto-plastic and based on a simple bounding surface approach. The concept assumes that the reversible deformation of the intergranular strain layer, combined with the elastic deformation of the grains, accounts for all the measured soil deformations at the beginning of the loading process until a certain amount of strain is reached, and the grains start to rearrange. This reversible deformation is described by an additional component of the model, while the deformation associated with the grain rearrangement is irreversible and predicted by the standard hypo-plastic model. Introducing the intergranular strain adds five more parameters, namely, m_R, m_T, β_r, R, and χ to the basic parameters; they are discussed in detail in the following sections (Yang et al., 2020). Niemunis' IS model is used for this investigation (Niemunis et al., 2005).

2.2.1 Stiffness factor (m_R)

The m_R parameter has a crucial role in regulating the shear modulus strength at extremely low strain values, whether it is during initial loading or when the strain path direction is reversed by 180 degrees. The most precise approach for ascertaining the value of m_R is via shear wave propagation experiments such as bender element tests. Although static shear tests can also measure the shear modulus, this method is less dependable as it relies on local measurements of sample deformations, and strain transducers have limitations regarding their accuracy.

2.2.2 Parameter m_T

Determining the m_T parameter (or m_{rat} ratio = m_T / m_R) through experimentation is a difficult task. The m_{rat} value indicates the ratio of the initial shear stiffness (G_0) to the shear stiffness after a 90-degree change in the strain path direction (G_{90}), expressed as G_{90}/G_0. Measuring G_{90} requires precise local strain transducers as it cannot be measured through wave propagationtechniques. To make it more convenient, Mašín (2019) recommends a default value of 0.7 for m_{rat} if there is no experimental data available for the soil of interest.

Figure 5 illustrates the relationship between m_R and m_T based on 14 sets of data collected in Tables 2 and 3. Therefore, in the absence of experimental data for m_T, according to Figure 4, a value of m_T=0.5*m_R can be used.

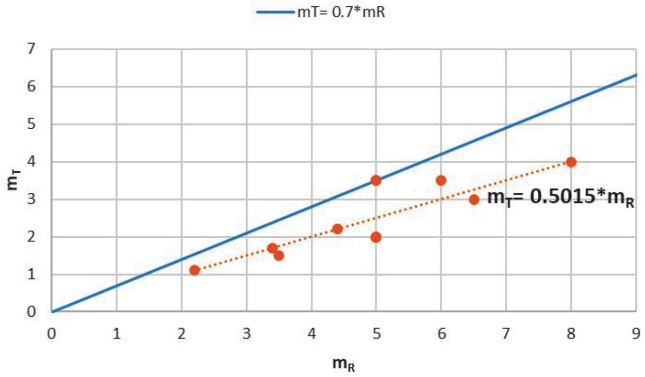

Fig. 4 *Relation between m_T and m_R*

2.2.3 Elastic strain amplitude, Intergranular strain hardening parameter and exponent

The intergranular strain concept model utilizes three parameters, namely R, β_r, and χ, each with a distinct physical interpretation. The parameter R specifies the extent of the elastic range in the strain space, whereas β_r controls the rate of evolution of the intergranular strain tensor. On the other hand, χ regulates the interpolation between the reversible elastic and nonlinear hypoplastic response. Despite their varied interpretations, these parameters work together to determine the rate of stiffness degradation with increasing strains, which, in turn, affect the predictions of the model. The calibration of these parameters usually involves triaxial shear experiments, which measure local deformations, and obtains shear moduli versus shear strain curves. An increase in R causes a decrease in βr and shifts the stiffness degradation curve horizontally in the G versus ln(ε_s) diagram. Conversely, χ influences the rate of a decrease in stiffness with a strain, and a higher χ value leads to a larger quasi-elastic range size and a faster subsequent rate of decrease in stiffness. To calibrate the χ parameter, an experimental trial-and- error process is required to fit the data.

Tab. 2 *Basic hypoplastic parameters of different types of soil*

	Basic hypoplastic							
	φ_c (°)	h_s (MPa)	n	e_{d0}	e_{c0}	e_{i0}	α	β
Hochstetten gravel (Herle and Gudehus, 1999)	36	3.2000E+04	0.18	0.26	0.45	0.5	0.1	1.9
Hochstetten sand (Herle and Gudehus, 1999)	33	1.5000E+03	0.28	0.55	0.95	1.5	0.25	1
Hochstetten sand (A. Niemunis and Herle, 1997)	33	1.0000E+03	0.25	0.55	0.95	1.5	0.25	1
Hostun sand (Herle and Gudehus, 1999)	31	1.0000E+03	0.29	0.61	0.96	1.9	0.13	2
Karlsruhe sand (Herle and Gudehus, 1999)	30	5.8000E+03	0.28	0.53	0.84	1	0.13	1
Lausitz sand (Herle and Gudehus, 1999)	33	1.6000E+03	0.19	0.44	0.85	1	0.25	1
Toyoura sand (Herle and Gudehus, 1999)	30	2.6000E+03	0.27	0.61	0.98	1.1	0.18	1.1
Zbraslav sand (Herle and Gudehus, 1999)	31	5.7000E+03	0.25	0.52	0.82	0.95	0.13	1
Uncemented gravel (Fu et al., 2021)	39.5	7.5000E+01	0.55	0.17	0.40	0.48	0.06	1.5
Uncemented sand (Fu et al., 2021)	28.6	9.5500E+01	0.45	0.48	0.75	0.86	0.15	1.25
Karlsruhe fine sand (Poblete et al., 2016)	33	8.6260E+01	0.32	0.67	1.9	1.21	0.21	1.5
Karlsruhe fine sand (Fuentes et al., 2020)	32.6	4.0000E+03	0.27	0.677	1.054	1.212	0.14	2.5
Prague sand (Kadlíček et al., 2016)	35.47	9.0530E+01	0.56	0.33	0.66	0.79	0.03	1.9
Komorany sand (Mašín, 2019)	35	5.0000E+01	0.2	0.35	0.87	1.4	0.26	4
Dobrany (Kadlíček et al., 2022)	41.1	6.5339E+01	0.207	0.592	1.183	1.42	0.05	4
Hrusovany (Kadlíček et al., 2022)	42.6	1.9030E+00	0.162	0.591	1.182	1.418	0.07	6.3
Jablonec (Kadlíček et al., 2022)	42.6	1.0370E+00	0.232	0.616	1.232	1.478	0.02	4.1
Kralupy (Kadlíček et al., 2022)	41.2	1.7560E+00	0.149	0.809	1.1618	1.942	0.23	4.8
Stvanice (Kadlíček et al., 2022)	35.8	8.5300E-01	0.199	0.844	1.689	2.026	0.23	4.9
Hochstetten sand (Khalaj, 2021)	33	1.5000E+03	0.28	0.55	0.95	1.5	0.25	1.5
Toyoura sand (Ng et al., 2013)	30	2.6000E+03	0.27	0.61	0.98	1.1	0.14	3
Firoozkuh sand (Mohammadi-Haji and Ardakani, 2020)	32.7	3.5000E+02	0.24	0.58	0.91	1.1	0.5	1
Hostun sand (Moussa et al., 2020)	32	1.0000E+03	0.29	0.61	0.96	1.9	0.13	2
Tehran silica sand (Namaei-kohal et al., 2022)	38.4	4.6000E+02	0.26	0.41	0.82	0.98	0.3	1.5
Used for model (Niemunis et al., 2005)	32.8	1.5000E+02	0.4	0.575	0.908	1.044	0.12	1

⇒

	Basic hypoplastic							
	φ_c (°)	h_s (MPa)	n	e_{d0}	e_{c0}	e_{i0}	α	β
Original model (Yang et al., 2020)	34	3.6000E+03	0.43	0.72	0.934	1.2	0.24	1.2
Karlsruhe sand (Stutz et al., 2017b)	31	1.0000E+03	0.29	0.61	0.96	1.9	0.13	2
Toyoura sand (Stutz et al., 2016)	30	2.6000E+03	0.27	0.61	0.98	1.1	0.25	1
Ticino sand (Stutz et al., 2016)	31	1.0000E+03	0.29	0.61	0.96	1.9	0.13	2
Density sand (Stutz et al., 2016)	32	7.5000E+02	0.25	0.62	0.97	1.6	0.13	1.5
Toyura sand (Stutz and Wuttke, 2018)	31	1.0000E+03	0.29	0.61	0.96	1.9	0.13	2
Berlin Sand (Le et al., 2017)	31.5	2.3000E+03	0.30	0.391	0.688	0.791	0.13	1
Castro sand (Tsegaye et al., 2010)	30.5	1.1070E+03	0.26	0.5	0.8	0.97	0.2	2
Karlsruhe fine sand (Wichtmann et al., 2019)	33.1	4.0000E+03	0.27	0.677	1.054	1.212	0.14	2.5
Kolny sand, set 1 (Mašín, 2019)	35	4.8000E+02	0.26	0.33	0.87	1.4	0.06	1.47
Kolny sand, set 2 (Mašín, 2019)	36	1.2000E+02	0.49	0.28	0.74	0.89	0.03	1.41
Parameter used (Sturm, 2009)	32.8	6.2500E+02	0.33	0.67	1.5	1.21	0.18	1.12
Toyoura sand (Arnold, 2008)	30	2.6000E+03	0.27	0.61	0.98	1.1	0.18	1

Tab 3. *Intergranular strain parameters of different types of soil*

	Intergranular strain				
	m_R	m_T	$R \times 10^{-4}$	βr	χ
Hochstetten sand (Niemunis and Herle, 1997)	5	2	1	0.5	6
Karlsruhe fine sand (Poblete et al., 2016)	5	3.5	1.4	0.35	7
Karlsruhe fine sand (Fuentes et al., 2020)	5	3.5	1.4	0.25	5
				3	17.7
Komorany sand (Mašín, 2019)	3.4	1.7	2	0.12	0.7
Toyoura sand (Ng et al., 2013)	8	4	0.2	0.1	1
Firoozkuh sand (Mohammadi-Haji and Ardakani, 2020)	5	2	1	0.5	3
Tehran silica sand (Namaei-kohal et al., 2022)	3.5	1.5	0.7	0.7	0.8
Used for model (Niemunis et al., 2005)	6.5	3	1	0.1	6
Original model (Yang et al., 2020)	1	--	3.3	0.5	3
Berlin Sand (Le et al., 2017)	4.4	2.2	1	0.2	6
Castro sand (Tsegaye et al., 2010)	5	2	1	0.5	6
Karlsruhe fine sand (Wichtmann et al., 2019)	2.2	1.1	1	0.1	5.5
Parameter used (Sturm, 2009)	6	3.5	1	0.2	6
Toyoura sand (Arnold, 2008)	5	2	1	0.12	1

3 RESULTS

3.1 Basic Parameters

3.1.1 Critical state friction angle (φc)

The critical state line (CSL) in the q-p plane was utilized to determine the value of the critical state friction angle, φ_c, using the equation:

$$q = M \times p \tag{11}$$

and the formula:

$$\sin \varphi_c = \frac{3M}{6+M} \tag{12}$$

Three monotonic triaxial tests were conducted, and the final point for each test was plotted on the q-p diagram. To obtain the M constant, a trendline was drawn, and the constant slope of the resulting linear equation 12 was designated as the M parameter.

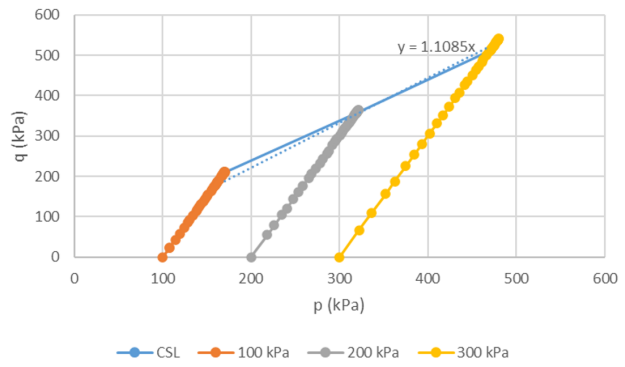

Fig. 5 *Results of triaxial tests to determine CSL*

By using equations 11 and 12, the critical state friction angle, φ_c, was computed to be 27.89289 degrees.

3.1.2 Granular hardness (hs) & Exponent (n)

It is worth mentioning that the maximum compression stress utilized in the experiment has a significant impact on granulate hardness. One might consider conducting an oedometer test on a loose sample to get these two parameters:

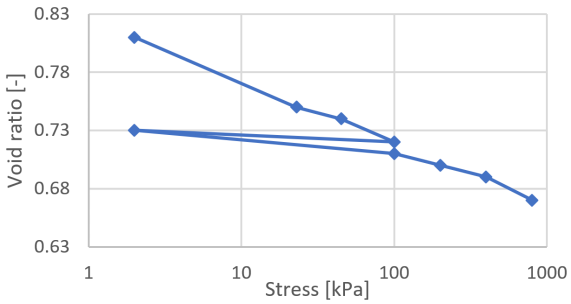

Fig. 6 *Compression Curve*

The following table is the result of the oedometer test:

Tab. 4 *Result of oedometer test*

Vertical stress (kPa)	2	100	200	400	800
Void ratio	0.73	0.71	0.7	0.69	0.67

Table 4 and equations 1 and 2 lead the parameter n and h_s as follows:

n =0.303153655

h_s =3.085316 (GPa)

3.1.3 Minimum (e_{d0}), Critical (e_{c0}) and Maximum void ratio at zero pressure (e_{i0})

The values of e_{min} and e_{max} were obtained through laboratory measurements, yielding 0.62 and 1.01, respectively. Additionally, e_{i0} was defined using the empirical formula e_{i0}=1.2*e_{c0}, which resulted in a value of 1.2 for e_{i0}. Although e_{c0} should be similar to e_{max}, previous investigations have suggested that its value is slightly lower, i.e., around 0.971. Finally, e_{min} and e_{d0} were found to be the same, with a value of 0.62 for this parameter.

3.1.4 Dilatancy (α) and Exponent (β)

In order to obtain the calibrated value for the parameters, several simulations with different values for α were performed. According to the comparison between the experimental drained cyclic triaxial test and the simulated cyclic triaxial test, the optimized value for α is 0.3. The initial void ratio for the simulated test was e_0=0.65.

β seems to mostly be independent of granulometric features, and 1 may be assumed for many natural sands.

To gain a deeper comprehension of the impact of β, multiple simulations were conducted using various values of β. The test involved 10,000 cycles, each lasting 2 seconds. The most accurate curve was identified when β was set to 1.1.

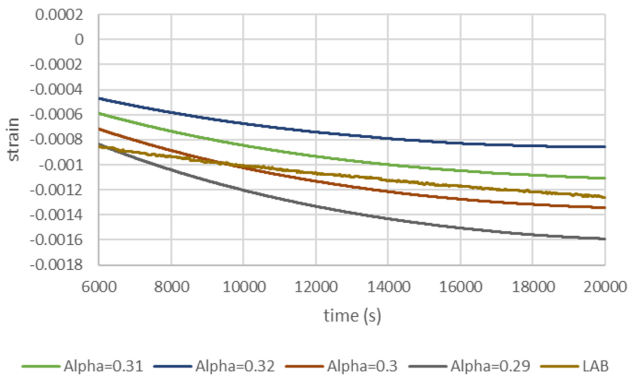

Fig. 7 *Value of the strain over time for different α's*

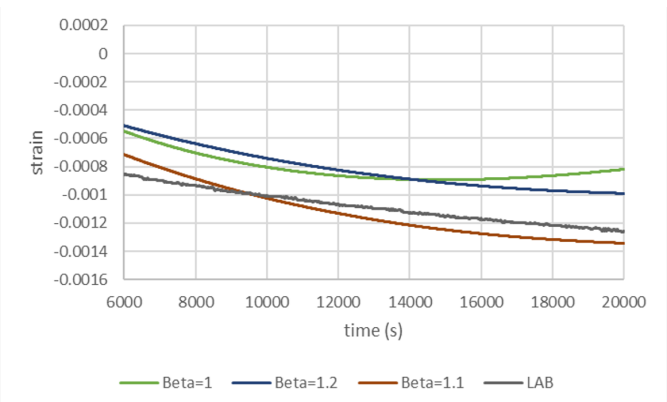

Fig. 8 *Value of the strain over time for different β's*

3.2 Intergranular parameters

3.2.1 Stiffness factor (m_R) and Parameter m_T

A comparison was conducted between the results of a drained cyclic triaxial test performed on a soil sample and a simulated triaxial test using the SoilTest Module of PLAXIS software to calibrate the intergranular strain parameters. Figure 9 shows that an increase in stiffness leads to a decrease in the amount observed of the average axial strain. According to Figure 10, setting the parameter m_T to 1 results in a similar amount of the average axial strain observed in both the simulated and laboratory samples.

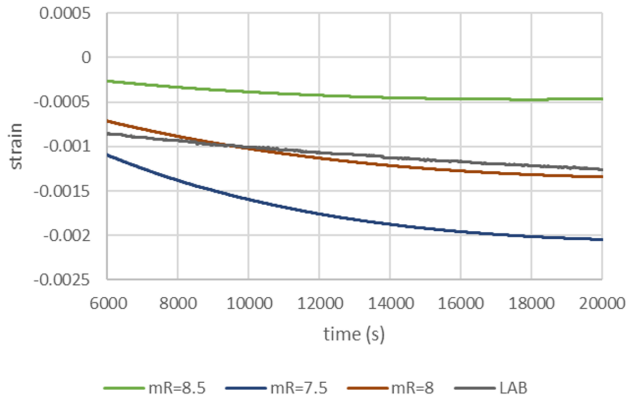

Fig. 9 *Value of the strain over time for different mR's*

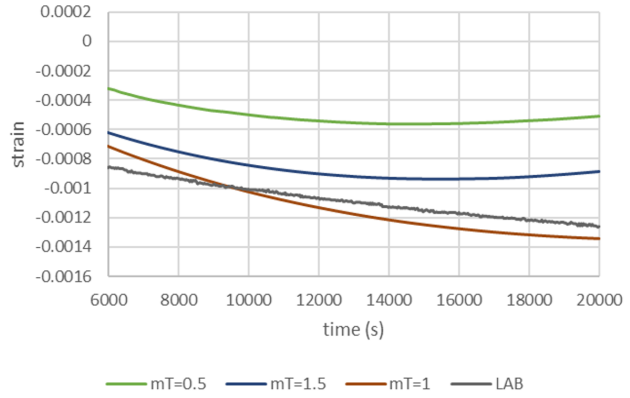

Fig. 10 *Value of the strain over time for different mT's*

3.2.2 Elastic strain amplitude, Intergranular strain hardening parameter and the exponent

According to Mašín (2019), it is difficult to differentiate the effect of m_R, β_r, and χ on the accumulation of strain caused by cyclic loading. Hence, he suggested a calibration method that involves treating $R=10^{-4}$ and $\chi=1$ as constants independent of the material. Then, m_R can be calibrated using bender element measurements, which are relatively simple to perform. Moreover, m_T can be set at $0.7*m_R$. Finally, the cyclic behavior can be controlled by adjusting only the parameter β_r.

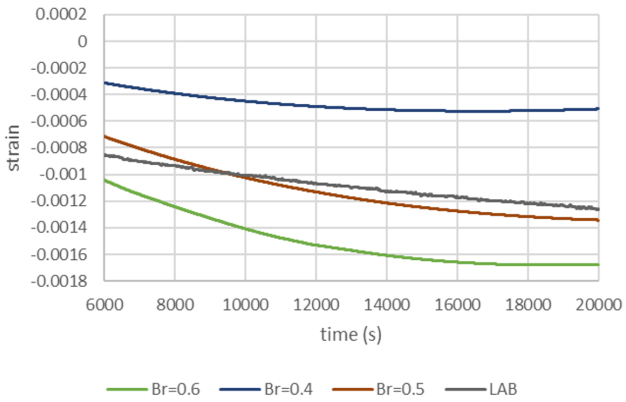

Fig. 11 *Value of the strain over time for different βr's*

Figure 12 demonstrates that increasing R_{max} alters the curvature behavior to a linear one. Furthermore, Figure 11 shows that decreasing β_r results in a reduction in the final average axial strain observed. From Figure 13, it can be inferred that the optimal value of the parameter χ is 1.2, as both higher and lower values lead to a decrease in the final average axial strain value.

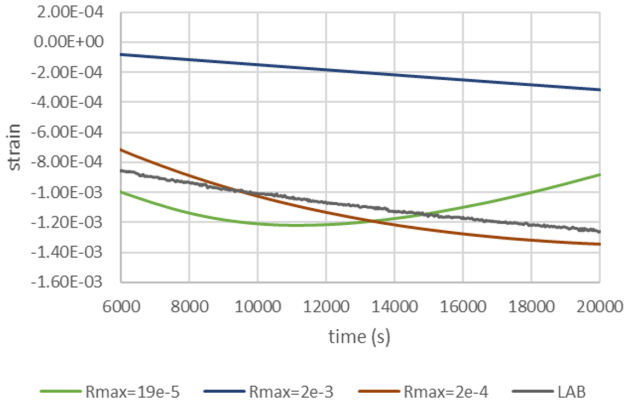

Fig. 12 *Value of the strain over time for different Rmax's*

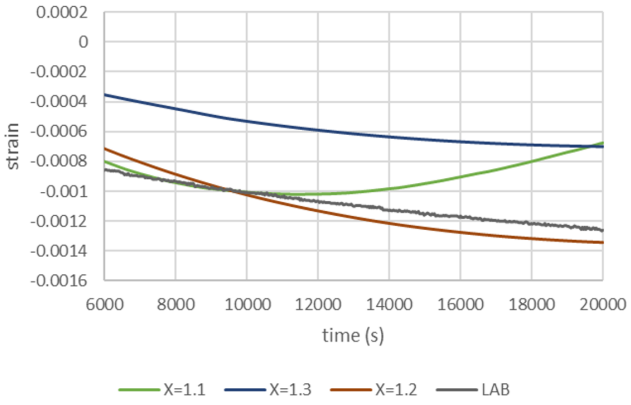

Fig. 13 *Value of the strain over time for different χ's*

4 CONCLUSIONS

This paper describes the calibration of the hypoplastic constitutive model with an intergranular strain for Danube sand using experimental static and dynamic soil tests, analytical solutions, and numerical simulations. The required parameters and their appropriate computation are provided, and the calibration technique used eliminates the need for complex geotechnical experiments. The accuracy of the constitutive parameters determined in this study was verified through numerical modeling and analytical solutions.

The values for the basic hypoplastic model parameters φ_c, n, h_s, e_{i0}, e_{d0}, e_{c0}, α, and β were determined using drained triaxial and oedometer testing, and previous research provided suggested values for e_{d0} and e_{i0}. α and β were adjusted to ensure a good fit between the simulated curve and the drained cyclic triaxial test. Similarly, the intergranular parameters m_R, m_T, β_r, R_{max}, and χ were determined through drained cyclic triaxial tests and numerical simulations to achieve the best fit.

Tab. 5 *Danube Sand data and range of basic hypoplastic parameters*

	φ_c (°)	h_s (GPa)	n	e_{d0}	e_{c0}	e_{i0}	α	β
Danube Sand	27.89	3.08	0.30	0.62	0.971	1.2	0.3	1.1
Minimum	28.6	8.53e-4	0.149	0.17	0.4	0.48	0.02	1
Maximum	42.6	32	0.56	0.844	1.689	2.026	0.5	6.3

The results show that both overestimating and underestimating χ and β lead to a lower predicted average axial strain in the final cycle. The predicted average axial strain in the first regular cycles is the same as in the experiment for all substitutional values. Thus, for long-term cyclic loading, the first cycles should not be considered. Tables 5 and 6 display the hypoplastic constitutive parameters of Danube sand, which were adjusted based on laboratory measurements. It also provides information on the range of values for each parameter, with the minimum and maximum values taken from Tables 2 and 3, which were derived from previous research.

Tab. 6 *Danube Sand data and range of intergranular strain parameters*

	m_R	m_T	R_{max}	β_r	χ
Danube Sand	8	1	2e-4	0.5	1.2
Minimum	1	1	2e-5	0.1	0.7
Maximum	8	4	3.3e-4	0.7	7

REFERENCES

Arnold, M. (2008) *Application of the intergranular strain concept to the hypoplastic modelling of non- adhesive interfaces.* 12th International Conference on Computer Methods and Advances in Geomechanics 2008, 1(1999), 747–754.

Bauer, E. – Kovtunenko, V. A. – Krejčí, P. – Krenn, N. – Sováková, L. – Zubkova, A. V. (2020) *On proportional deformation paths in hypoplasticity.* Acta Mechanica, 231(4), 1603–1619. https://doi.org/10.1007/s00707-019-02597-3

Fellin, W. (2002) *Hypoplasticity for beginners.* Institu Für Geotechnik Und Tunnelbau, (June), 1–6. Retrieved from ftp://ftp.uibk.ac.at/pub/uni-innsbruck/igt/publications/_fellin/hypo_beginner.pdf

Fu, Z. – Chen, S. – Zhong, Q. – Ji, E. (2021) *A damage hypoplasticity constitutive model for cemented sand and gravel materials.* Acta Geotechnica, *9*. https://doi.org/10.1007/s11440-021-01206-9

Fuentes, W. – Wichtmann, T. – Gil, M. – Lascarro, C. (2020) *ISA-Hypoplasticity accounting for cyclic mobility effects for liquefaction analysis.* Acta Geotechnica, 15(6), 1513–1531. https://doi.org/10.1007/s11440-019-00846-2

Gajári, G. – Kisgyörgy, L. – Ádány, S. – Mahler, A. – Lógó, J. (2021) *A visco-hypoplastic constitutive model for rolled asphalt.* Periodica Polytechnica Civil Engineering, 65(3), 798–809. https://doi.org/10.3311/PPci.17515

Herle, I. – Gudehus, G. (1999) *Determination of parameters of a hypoplastic constitutive model from properties of grain assemblies.* Mechanics of Cohesive-Frictional Materials, 4(5), 461–486. https://doi.org/10.1002/(SICI)1099-1484(199909)4:5<461::AID-CFM71>3.0.CO;2-P

Herle, I. – Kolymbas, D. (2004) *Hypoplasticity for soils with low friction angles*. Computers and Geotechnics, 31(5), 365–373. https://doi.org/10.1016/j.compgeo.2004.04.002

Kadlíček, T. – Janda, T. – Šejnoha, M. (2016) *Calibration of Hypoplastic Models for Soils.* Applied Mechanics and Materials, 821, 503–511. https://doi.org/10.4028/www.scientific. net/amm.821.503

Kadlíček, T. – Janda, T. – Šejnoha, M. – Mašín, D. – Najser, J. – Beneš, Š. (2022) Automated calibration of advanced soil constitutive models. Part I: hypoplastic sand. Acta Geotechnica,17(8), 3421–3438. https://doi.org/10.1007/s11440-021-01441-0

Khalaj, O. – Abedin Nejad, S. – Janda, T. (2021) *Multi Elements Simulation of Biaxial Test with Two Different Soil Layers Using Hypoplastic Constitutive Model.* IOP Conference Series: Materials Science and Engineering, 1161(1), 012001. https://doi.org/10.1088/1757-899x/1161/1/012001

Kolymbas, D. – Wu, W. (1990) *Recent results of triaxial tests with granular materials.* Powder Technology, 60(2), 99–119. https://doi.org/10.1016/0032-5910(90)80136-M

Le, V. H. – Rackwitz, F. – Savidis, S. A. (2017) *Accumulation of monopile deformation in sand due to change in load direction.* (March 2018).

Mašín, D. (2019) *Modelling of Soil Behaviour with Hypoplasticity: Another Approach to Soil Constitutive Modelling.*

Mašín, D. (2015) *Hypoplasticity for Practical Applications Part 4: Determination of material parameters*.

Mohammadi-Haji, B. – Ardakani, A. (2020) *Calibration of a Hypoplastic Constitutive Model with Elastic Strain Range for Firoozkuh Sand.* Geotechnical and Geological Engineering, 38(5), 5279– 5293. https://doi.org/10.1007/s10706-020-01363-w

Moussa, A. – Salah, M. – Rafik, D. (2020) *Improvement of a Hypoplastic Model for Granular Materials Under High-Confining Pressures.* Geotechnical and Geological Engineering, 38(4), 3761–3771. https://doi.org/10.1007/s10706-020-01256-y

Namaei-kohal, A. – Ardakani, A. – Hassanlourad, M. (2022) *Hypoplastic soil model parameters calibration for Tehran silica sand and verification with a monotonic geocell pullout test.* Arabian Journal of Geosciences, 15(9). https://doi.org/10.1007/s12517-022-10110-9

Ng, Ch. W. W. – Boonyarak, T. – Mašín, D. (2013) *Three-dimensional centrifuge and numerical modeling of the interaction between perpendicularly crossing tunnels.* Canadian Geotechnical Journal, 50(9), 935–946. https://doi.org/10.1139/cgj-2012-0445

Niemunis, A. – Herle, I. (1997) *Hypoplastic model for cohesionless soils with elastic strain range.* Mechanics of Cohesive-Frictional Materials, 2(4), 279–299. https://doi.org/10.1002/(SICI)1099-1484(199710)2:4<279::AID-CFM29>3.0.CO; 2-8

Niemunis, A. – Wichtmann, T. – Triantafyllidis, T. (2005) *A high-cycle accumulation model for sand.* Computers and Geotechnics, 32(4), 245–263. https://doi.org/10.1016/j.compgeo.2005.03.002

Poblete, M. – Fuentes, W. – Triantafyllidis, T. (2016) *On the simulation of multidimensional cyclic loading with intergranular strain.* Acta Geotechnica, 11(6), 1263–1285. https://doi.org/10.1007/s11440-016-0492-2

Sturm, H. (2009) *Numerical investigation of the stabilisation behaviour of shallow foundations under alternate loading.* Acta Geotechnica, 4(4), 283–292. https://doi.org/10.1007/s11440-009-0102-7

Stutz, H. H. – Wuttke, F. (2018) *Hypoplasticmodeling of soil-structure interfaces in offshore applications.* Journal of Zhejiang University: Science A, 19(8), 624–637. https://doi.org/10.1631/jzus.A1700469

Stutz, H. – Mašín, D. – Sattari, A. S. – Wuttke, F. (2017a) *A general approach to model interfaces using existing soil constitutive models application to hypoplasticity*. Computers and Geotechnics, 87, 115–127. https://doi.org/10.1016/j.compgeo.2017.02.010

Stutz, H. – Mašín, D. – Sattari, A. S. – Wuttke, F. (2017b) *A general approach to model interfaces using existing soil constitutive models application to hypoplasticity.* Computers and Geotechnics, 87, 115–127. https://doi.org/10.1016/j.compgeo.2017.02.010

Stutz, H. – Mašín, D. – Wuttke, F. (2016) *Enhancement of a hypoplastic model for granular soil–structure interface behaviour.* Acta Geotechnica, 11(6), 1249–1261. https://doi.org/10.1007/s11440-016-0440-1

Tsegaye, A. B. – Molenkamp, F. – Brinkgreve, R. B. J. – Bonnier, P. G. – De Jager, R. – Galavi, V. (2010) *Modeling liquefaction behavior of sands by means of hypoplastic model.* Numerical Methods in Geotechnical Engineering - Proceedings of the 7th European Conference on Numerical Methods in Geotechnical Engineering, (1), 81–87. https://doi.org/10.1201/b10551-18

von Wolffersdorff, P. A. (1996) *Hypoplastic relation for granular materials with a predefined limit state surface.* Mechanics of Cohesive-Frictional Materials, 1(3), 251–271. https://doi.org/10.1002/(SICI)1099-1484(199607)1:3<251::AID-CFM13>3.0.CO;2-3

Wang, S. – Wu, W. (2020) *A simple hypoplastic model for overconsolidated clays.* Acta Geotechnica, 16(1), 21–29. https://doi.org/10.1007/s11440-020-01000-z

Wei, X. – Chen, Y. – Yang, J. (2020) *A unified critical state constitutive model for cyclic behavior of silty sands.* Computers and Geotechnics, 127 (July), 103760. https://doi.org/10.1016/j.compgeo.2020.103760

Wichtmann, T. – Fuentes, W. – Triantafyllidis, T. (2019) *Inspection of three sophisticated constitutive models based on monotonic and cyclic tests on fine sand: Hypoplasticity vs. Sanisand vs. ISA.* Soil Dynamics and Earthquake Engineering, 124 (April 2018), 172–183. https://doi.org/10.1016/j.soildyn.2019.05.001

Wichtmann, T. – Triantafyllidis, T. (2018) *Monotonic and cyclic tests on kaolin: a database for the development, calibration and verification of constitutive models for cohesive soils with focus to cyclic loading.* Acta Geotechnica, 13(5), 1103–1128. https://doi.org/10.1007/s11440-017-0588-3

Wu, W. – Bauer, E. (1994) *A simple hypoplastic constitutive model for sand*. International Journal for Numerical and Analytical Methods in Geomechanics, 18(12), 833–862. https://doi.org/10.1002/nag.1610181203

Wu, W. – Lin, J. – Wang, X. (2017) *A basic hypoplastic constitutive model for sand.* Acta Geotechnica, 12(6), 1373–1382. https://doi.org/10.1007/s11440-017-0550-4

Yang, Z. – Liao, D. – Xu, T. (2020) *A hypoplastic model for granular soils incorporating anisotropic critical state theory.* International Journal for Numerical and Analytical Methods in Geomechanics, 44(6), 723–748. https://doi.org/10.1002/nag.3025

sciendo

Slovak Journal of Civil Engineering

Vol. 32, 2024, No. 1, 46 – 51
DOI: 10.2478/sjce-2024-0006

THE EFFECT OF THE DEVELOPMENT OF BICYCLE TRANSPORT FROM THE POINT OF VIEW OF THE INHABITANTS OF THE CITY OF BRATISLAVA

Jakub TAKÁCS[1*]

Abstract

As part of a change in the division of transport work, bicycle transport has made the most progress in recent years. As the largest city in Slovakia Bratislava, is trying to keep up with foreign cities. In recent years, it has developed projects that have made it possible to increase the development of cycling in the city. The last major cycling survey was conducted in 2011 by Cyklokoalicia. This survey aims at determining the momentum of bicycle traffic by identifying its greatest shortcomings or, conversely, the most positives. The data from the analysis given will also be used to develop a concept for the development of bicycle transport in the city of Bratislava.

Address

[1*] Dept. of Transportation Engineering, Slovak University of Technology in Bratislava, Slovakia

[*] ***Corresponding author:*** *jakub.takacs@stuba.sk*

Key words

- Mobility,
- Cycling traffic,
- Capital city,
- Survey.

1 INTRODUCTION

Slovakia is a country that still lags behind other countries in the world in the development of transport. Cities should focus on all modes of transport when determining their development and growth. In recent years, emphasis has been placed on non-motorized transport, such as bicycle transport, which has a positive effect on the environment and overall sustainability in a city. The problem of sustainable mobility is a longstanding issue in Slovakia that needs to be addressed. The city of Bratislava was chosen, as it lacks a developed cycling infrastructure. Based on the missing documentation, a survey which could help us to take a closer look at people's views on the matter and also initiate the basis for a design of the development of bicycle transport was created. The questionnaire addresses the basic issues affecting the attitude of the inhabitants of the capital of Slovakia on the issue of bicycle transport. It was shared on social networks and also in cooperation with Cyklokoalícia. After the gathering of sufficient answers, the questionnaire was evaluated and compared with the questionnaire conducted in 2011 by Cyklokoalícia to determine how people's attitudes towards cycling in the city of Bratislava have changed over the past 10 years.

2 THE IMPACT OF CYCLING ON SUSTAINABLE MOBILITY

Based on a methodology (European Commission, 2011) written by European Union experts, individual Member States (MS) plan to reduce their greenhouse gas emissions by 60%. As the current transport system is still unsustainable, it is clear that transport in the next 40 years cannot develop in the same way as before. If the current approach were to continue, transport's dependence on fossil fuels would only not increase, but would reach 90%. In this way, CO2 emissions from transport would be one-third higher in 2050 than in 1990. In order to reduce greenhouse gas emissions, Member States have set 10 targets for competitive and resource-efficient transport systems. The first goal is to halve the use of "conventionally powered" urban transport cars by 2030 and phase them out of cities by 2050. Also, MS intend to achieve the introduction of essentially CO2-free urban logistics in large city centres by 2030. This measure would also significantly reduce other harmful emissions in public areas of a city. Some Western European countries have been making progress on sustainable mobility plans for years and are trying to create acceptable conditions for cycling in their cities. These countries are based on their

national cycling strategies, which currently serve as a model for other European countries, as they have managed to ensure that the share of cycling in urban mobility is significantly higher than in other countries (The Netherlands 27%, Denmark 19%). In 2015, Slovakia adopted its own national strategy for the development of bicycle transport (Ministry of Transport, Construction and Regional Development of the Slovak Republic, 2015). The national strategy sets out several priorities for achieving the sustainable development of cycling. One of these priorities is the development of a cycling infrastructure. It tells us that it is necessary to ensure the conditions for the creation and updating of planning and strategic documents integrating cycling and ensuring sustainable urban mobility. An equally important condition is the construction of a new cycling infrastructure, which can be divided into a main one, which includes the bike paths themselves, and an additional one, which includes bicycle stands and shelters, information boards and signs. Based on the set priorities of the National Strategy, various benefits can be expected for the development of bicycle transport (Fig. 1).

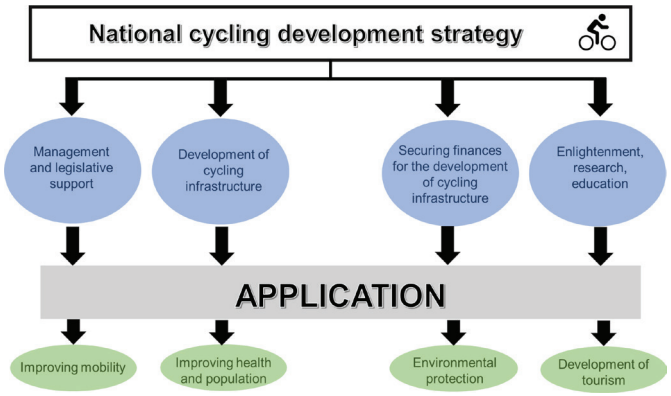

Fig. 1 *Priorities and benefits of the national cycling development strategy*

Each city has specific conditions, so it must adapt the National Strategies and create its own documents to meet the goals of sustainable mobility. The city of Bratislava has created several strategic documents that take bicycle traffic into account. These documents include a zoning plan, transport master plan, the principles for the development of cycling, and pedestrian transport, which are included annually in the action plans for the development of cycling and pedestrian transport for the given years. Although the city has these documents, the problem is their interconnection, and the concept of bicycle transport in the future is not addressed in detail. This is based on the statement that: "Cycling routes in Bratislava are not safe or interconnected, there are few of them. This is despite the fact that the number of bicycles in Bratislava is greater than the number of cars. Almost every household has access to a bicycle, while only 65% of households own a car" (Vallo et al., 2018).

The importance of increasing the share of bicycle traffic is addressed not only in Slovakia but also abroad (Vaismaa et al., 2012) (Ton et al., 2019). An increase in the share of bicycle traffic has a positive effect on improving air quality and the associated reduction in emissions from traffic (Neves and Brand, 2019). The creation of concepts at individual levels should be comprehensively devoted to individual elements of the cycling infrastructure, such as, for example, bicycle parking (CROW platform, 2011) (European Cyclists Federation, 2018). All these elements should be included in a single manual for a given city or state (CROW platform, 2016) (Manoela et al., 2014) (Nabors et al., 2012). Improving cycling infrastructure will help to change the division of transport labour, which will not only be reflected in environmental and economic terms (Floater et al., 2014) (Gehl Architects, 2010), but also in terms of accessibility (Rode et al., 2014). With shorter commuting distances using walking or cycling, the sales of local businesses can be increased (Guy, 1983) (Guers, 2018) (Koopmans et al., 2013). Cities where such local economic growth have occurred include New York City, which by building bike lanes, BUS lanes, and increasing public spaces, has achieved economic growth just in local stores. The above considerations show the importance of multimodal planning in urban transportation network design, where, if designed properly, a city can support different social groups of residents and improve their living standards (Litman, 2018) (Schlosser and Schlosser, 2018).

3 EVALUATION OF SURVEY

In December 2021, a questionnaire was created, which was in electronic form due to the ongoing pandemic situation. It was created on the my.survio.com website, where the collection of responses took place until the end of January 2022. It consisted of 11 questions, which were used to find out the basic viewpoints of respondents on cycling. Information was also obtained on the regularity of the use of bicycle transport, the purpose of the transport, parking sites, accidents, etc. The questionnaire was published on the Facebook and Instagram social networks. To increase awareness of the survey, Facebook groups such as Cyklokoalícia, Bicykluj Bratislava, Švihaj šuhaj, and STU Bratislava helped.

A total of 280 people participated in the survey, 194 of which were male, which represents 69% of the total number of respondents, 80 were female (29%), and 6 people (2%) chose the option of a different gender (Fig. 2).

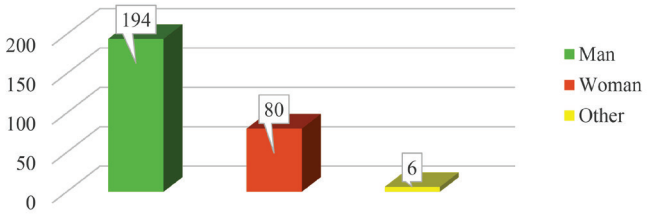

Fig. 2 *Evaluation of the question asking about gender*

Of the 280 people surveyed, people aged 26 to 40 most often use cycling. It is this age group that accounts for 50.7% of the total responses. The next most common response was from riders aged 19 to 25, with a percentage of 23.9%. Between the ages of 41 and 60, the percentage was 21.4%. The survey involved 6 people aged 61 and over, 4 people aged 16 to 18, and 1 person under 15 years old. From the resulting data, the small representation of age groups 61 and older and respondents under 18 years of age could be due to the publishing of the questionnaire mainly on Facebook and Instagram groups,

in which seniors and youth under 18 years have little active representation (Fig. 3).

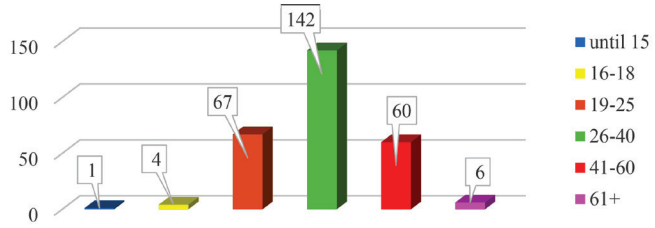

Fig. 3 *Evaluation of the age-related question*

The third question in the survey was to obtain information on the use of cycling in terms of time. Seven response options were created, which included the regular use of bicycle transport during the year. It was determined that the weekly regularity of rides of our respondents is 66.4%, where 27.96% are the number of people who use the bicycle as a source of transport every day. From the data obtained, it can be seen that respondents aged 26-60 mostly ride every day and, conversely, young people aged 19-25 only ride seasonally (Fig. 4).

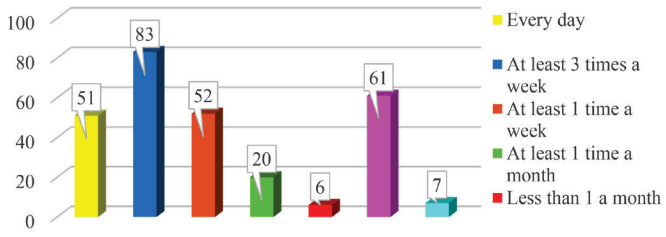

Fig. 4 *Evaluation of the question asking about the use of bicycle transport*

Question No. 4 dealt with transport by bicycle in terms of ownership. According to the options chosen for the answer, it seems that respondents use only their own bicycle for transport, which corresponds to 70.4% of the respondents. Another option is to get around using public bicycles (bikesharing), where 6.4% of respondents answered us. It can be assumed that due to the pandemic situation, the preference for only this type of transport has not grown among people, which resulted in a low percentage. Of all the respondents 19.6% use both public and private bicycles. The data show us that bikesharing companies are popular mainly in the age category of 26-40 years, while they are not so preferred among young and older people, and the possibility of owning a bicycle prevails (Fig. 5).

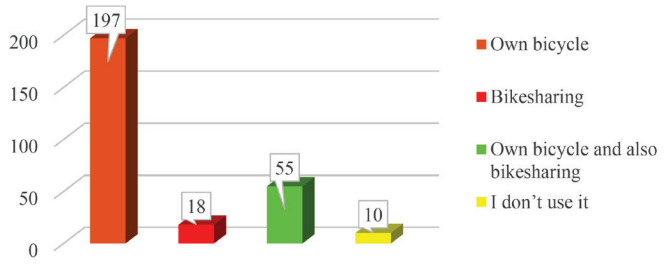

Fig. 5 *Evaluation of the question asking about the bicycling method used*

One of the questions of interest was whether our respondents have a place to park their own bicycle. Of the 280 respondents, it seems that 40.7% carry a bicycle with them, while 47.1% of the respondents also use public stands or covered spaces for parking. An interesting finding was that only 37 of the 117 respondents who carried a bicycle with them also indicated the possibility of missing bicycled stands, which means that a lack of parking stands is not a reason to carry a bicycle with you (Fig. 6).

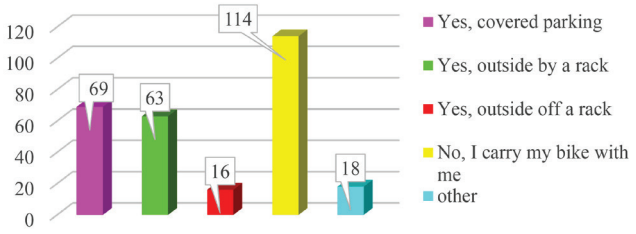

Fig. 6 *Evaluation of the question asking about parking options*

Question No. 6 addressed the purpose of using a bicycle. The respondents were able to choose the answers that agreed with their most frequent rides. Most respondents (71.4 %) ticked recreation as one of the options. On the other hand, 70.7% chose travel to the post office, bank or shopping as the most common option, while 59.6% of the respondents chose the option of using a bike for work or education. The least chosen option was entertainment, which was given by only 36.4% of the total number. Young people in the 19-25 age group prefer cycling mainly for recreation and not for education and work, while respondents in the 26-40 age group use a bicycle at least three times a week for work (Fig. 7).

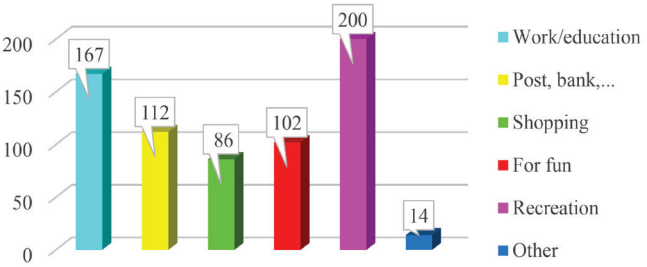

Fig. 7 *Evaluation of the question asking for the purpose of bicycle use*

Another important aspect was the identification of deficiencies in the infrastructure for cyclists. Respondents chose from the 9 options that they think are most lacking in their city. According to the percentage results, we see that the inhabitants of the city of Bratislava noted a lack of cycling routes the most, which was indicated by up to 82.5% of respondents, as well as separation from car transport, which corresponded to 77.5%. A major shortcoming was also the condition of the existing bicycle paths (42.5%), separation from pedestrian traffic (39.3%), or missing parking stands (32.5%). Less than 20% of the respondents chose more information about the possibilities of using bicycles (maps, tips) or technical equipment (charging stations, pumps, tools, etc) (Fig. 8).

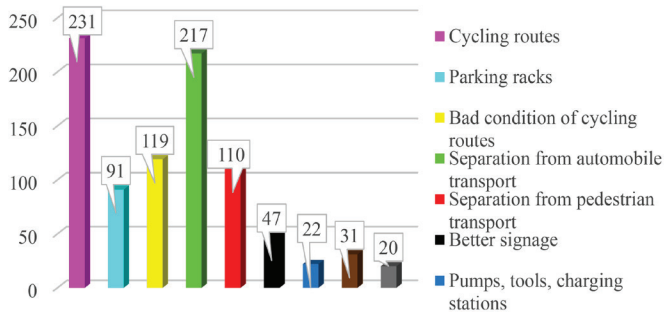

Fig. 8 *Evaluation of the question asking about infrastructure deficiencies*

Also of interest was whether the respondents used bicycle transport after dark and also when it is raining or snowing. Surprisingly, up to 80.7% said that they ride even after dark, and 48.9% use bicycle transport even in bad weather such as snow or rain. It was found that respondents who ride after dark cited the lack of bike paths and separation from car traffic as the biggest problem.

The accident rate was 23.2%, which was higher than expected. Of the 65 respondents who have had an accident, as many as 41 checked the possibility that they were riding when it was snowing, raining and even after dark. It is assumed that some accidents may be caused by these factors.

4 DEVELOPMENT OF A VIEW OF A CYCLING INFRASTRUCTURE

Based on the two completed surveys, the change in people's view of the cycling infrastructure and their attitude to the basic issues related to their relationship to cycling was of interest. One of the larger surveys on bicycle transport in Bratislava, which was conducted in 2011, was compared with our survey, so that we could see how the creation of newer projects in the city of Bratislava affected people's attitudes on the issue. In addition to the new projects that had arisen in the city, attitudes may have been influenced by the attempt to change the division of transport work, i.e., when cities are trying to reduce car traffic and cycling is gaining ground. The results of this year's survey are marked in blue in the tables. The results of the 2011 survey are in green.

Gender representation has not changed after ten years. From the given data we can see that there is still a higher interest in cycling by men than by women (Tab. 1).

Tab. 1 *Comparing the question asking about gender*

What is your gender?			
Man	69.3%	**Man**	67%
Woman	28.6%	**Woman**	32%

According to the percentage result of the 26-40 year old age group, where in 2011, there was a higher interest in bicycle transport compared to 2021, it was assumed that two thirds of this age group have moved to the category of older than 41 years after ten years. It can also be seen that young people's interest has not changed (Tab. 2).

Tab. 2 *Comparing the question asking for age*

What is your age?			
19-25	23.9%	**19-25**	21%
26-40	50.7%	**26-40**	66%
41+	23.5%	**41+**	13%

As can be seen, the respondents' interest in cycling has increased on a more regular basis after ten years, as they only rode once a week ten years ago, while they currently use bicycles daily or at least three times a week (Tab. 3).

Tab. 3 *Comparing the question asking about the use of bicycle transport*

How often do you use a bicycle?			
Every day	18.2%	**Every day**	16%
At least 3 times a week	29.6%	**At least 3 times a week**	38%
At least 1 time a week	18.6%	**At least 1 time a week**	38%

The data show that respondents stopped carrying bicycles with them, but began to use covered parking and also outdoor stands. Based on the data, it can be assumed that the number of these bicycle storage places has increased (Tab. 4).

Tab. 4 *Comparing the question asking about parking options*

Do you have a place to park your bike outside your home?			
Yes, covered parking	24.6%	**Yes, covered parking**	16%
Yes, outside on a rack	22.5%	**Yes, outside on a rack**	5%
No, I carry my bike with me	40.7%	**No, I carry my bike with me**	61%

After ten years, it can be seen that the interest in using a bicycle for ordinary things such as a trip to the post office, to the bank or for shopping has increased, which may be due to the greater number of indoor and outdoor storage spaces, as follows from the question before (Table 4). But it can also be seen that interest in a journey for recreation has dropped significantly, which would be worth further examination (Tab. 5).

Tab. 5 *Comparing the question asking for the purpose of use*

What purpose do you use a bicycle for?			
Work/education	59.6%	**Work/education**	53%
Post, bank,...	40.0%	**Post, bank,...**	33%
Shopping	30.7%	**Shopping**	20%
Recreation	71.4%	**Recreation**	83%

It can be seen that, according to the percentages, the cycling infrastructure has in general improved considerably,

Tab. 6 *Comparing the question asking about infrastructure deficiencies*

What infrastructural deficiencies does cycling transport have?			
Cycle routes	82.5%	**Cycle routes**	94%
Parking racks	32.5%	**Parking racks**	57%
Better signage	16.8%	**Better signage**	51%
Information about the possibilities of using a bicycle (maps, tips,...)	11.1%	**Information about the possibilities of using a bicycle (maps, tips,...)**	52%

which may be a consequence of the successful implementation of cycling projects over the last 10 years (Tab. 6).

The percentages found after ten years show us that the accident rate has increased slightly (Table 7), which may be due to the increased use of bicycle traffic even when it snows, rains or is after dark (Table 8, Table 9).

Tab. 7 *Comparing the question asking about the accident*

Have you had an accident on your bike?			
Yes	23.2%	**Yes**	19%
No	76.8%	**No**	81%

Tab. 8 *Comparing the question asking about riding after dark*

Do you ride after dark?			
Yes	80.7%	**Yes**	75%
No	19.3%	**No**	25%

Tab. 9 *Comparing the question of riding in the rain or snow*

Do you ride in the rain or snow?			
Yes	48.9%	**Yes**	38%
No	51.1%	**No**	62%

5 CONCLUSION

Although some 112 kilometres of cycle lanes and other infrastructure have been constructed in Bratislava between 2012 and 2022, and larger companies have begun to promote bicycle transport by creating covered storage areas or providing various benefits compared to using other modes of transport, this division of transport work still has not reached a sufficient share. Although fewer people took part in the survey than in 2011, the situation was affected by the coronavirus, where it was not possible to conduct a field survey. Cyklokoalícia, which conducted the 2011 survey, also participated in the promotion. The data from the survey was mainly used to compare the change in public opinion of the population over the last 10 years. The results helped the city evaluate improvements in the overall bicycle infrastructure. The system of building a bicycle infrastructure is not uniform, which is due to an insufficient concept for the development of a bicycle infrastructure in the city. In order to achieve a higher share of bicycle traffic, the city of Bratislava will have to proceed strategically when procuring new projects and building bicycle infrastructure. An important aspect is also the support of bicycle transport by employers or educational institutions. Construction of facilities, the provision of various benefits by the employer, and the construction of sufficient cycling infrastructure by the city will lead to increased interest in this mode of transport and a gradual positive change in the division of transport work, which could affect other cities not only in Slovakia but also in surrounding countries.

REFERENCES

CROW platform (2011) Bicycle parking and the quality of public space, Crow platform

CROW platform (2016) Cycle highways, cycle lanes and bicycle streets in The Netherlands, Crow platform

European Commission (2011) White paper, Roadmap to a single European transport area – towards a competitive and resource efficient transport system, Brussels, Belgium

European Cyclists Federation (2018) Making buildings fit for sustainable mobility, comparing regulations for off-street bicycle and car parking in Europe, European Cyclists' Federation

Floater, G. - Rode, P. et al. (2014) Cities and the new climate economy: the transformative role of global urban growth, NCE Cities – Paper 01. London School of Economics and Political Sciences

Gehl Architects (2010) Our city ourselves – the future of transportation in urban life. ITDP – Institute for Transportation and Development Policy

Guers, K. T. (2018) Transport planning with accessibility indices in The Netherlands. International Transport Forum, OECD

Guy, C. M. (1983) The assessment of access to local shopping opportunities: A comparison of accessibility measures. Environment and Planning B: Planning and Design, 10

Koopmans, C. W. et al. (2013) Measuring generalised transport costs as an indicator of accessibility changes over time. Transport Policy, 29

Litman, T. (2018) Evaluating transportation diversity – multimodal planning for efficient and equitable communities. Victoria Transport Policy Institute

Manoela S. da Rocha P. - King. R. (2014) Projects and programs manual to encourage cycling in communities, EMBARQ Brasil

Ministry of Transport, Construction and Regional Development of the Slovak Republic (2015) National strategy for the development of bicycle transport and cycling in the Slovak Republic

Nabors D. - Goughnour E. - Thomas L. - DeSantis W. - Sawyer M. (2012) Bicycle road safety audit guidelines and prompt lists, Federal Highway Administration

Neves A. - Brand Ch. (2019) Assessing the potential for carbon emissions savings from replacing short car trips with walking and cycling using a mixed GPS-travel diary approach, Transportation research part A: Policy and practice, vol. 123

Rode, P. - Floater, G. et al. (2014) Accessibility in cities: Transport and urban form, NCE Cities – Paper 03. London School of Economics and Political Sciences

Schlosser, T. - Schlosser, P. (2018) Traffic engineering analysis in the preparation and reconstruction of urban roads. Slovak Journal of Civil Engineering. Vol. 26, No. 2, ISSN 1210-3896

Ton D. - Duives D. - Cats O. - Hoogendoorn-Lanser S. - Hoogendoorn S. (2019) Cycling or walking? Determinants of mode choice in The Netherlands, Transportation research part A: Policy and practice, vol. 123

Vaismaa K. - Mäntynen J. - **Metsäpuro P. - Luukkonen T. - Rantala T. - Karhula K. (2012)** Best European practices in promoting cycling and walking, Tampere University of Technology, Transport research centre, Verne, Tampere 2012, ISBN 978-952-15-2716-6

Vallo M. and team (2018) Guide to a Better City, Plan Bratislava, ISBN 978-80-556-3596-5

sciendo

Slovak Journal of Civil Engineering

Vol. 32, 2024, No. 1, 52 – 57
DOI: 10.2478/sjce-2024-0007

PROPERTIES OF OLIVE STONES WITH A VIEW TO THEIR USE AS LIGHTWEIGHT AGGREGATE IN CONSTRUCTION MORTARS

Michal KURUC[1*], Zuzana ŠTEFUNKOVÁ[1]

Abstract

In countries that are big producers of olive oil such as Spain, Italy, or Greece, large amounts of olive husk remain as waste from processing olives and pose a serious environmental issue. One of the solutions could be to use this waste to partially replace sand in cement mortar to preserve the environment, decrease the consumption of cement, and improve economic benefits. This work presents our initial results which show the viability of using olive waste as an aggregate in cementitious mortars, indicating that the organic materials studied can be promising for this purpose.

Address

[1] Dept. of Materials Engineering and Physics, Slovak University of Technology, Bratislava, Slovakia

[*] ***Corresponding author:*** *michal.kuruc@stuba.sk*

Key words

- Olive waste,
- Water absorption,
- Aggregate.

1 INTRODUCTION

Green building materials and the valorization of waste from various industries have gained ever-increasing interest from the construction industry in recent years. Almost 50 % of global CO2 emissions come from the civil engineering sector (Aouba et al., 2016). The construction sector is the largest energy consumer and the largest producer of waste. Therefore, it is currently a great challenge to develop more sustainable, environmentally friendly, and economically efficient building materials. In recent decades, many researchers have investigated the use of various waste materials, including olive waste, in the civil engineering sector in order to achieve environmentally viable materials that are in accordance with the relevant standards (Aouba et al., 2016; Bourema et al., 2023; Junaid et al., 2022).

Natural lightweight aggregates, such as those provided from natural lightweight rocks (Shafigh et al., 2014), are economically rather feasible in comparison with artificial lightweight aggregates. The production of artificial lightweight aggregates is rather energetically demanding, and much of this energy is due to the burning of coal and combustible liquid waste products (Priyanka et al., 2013). However, since the building industry uses large amounts of raw materials and since natural resources are limited, it is very convenient and ecofriendly to utilize as much waste material and by-products as possible.

Alkheder et al. (2016) studied the behavior of cement paste and mortar after the use of olive waste in their production of samples. The results showed that the normal consistency and workability of cement pastes containing different percentages of olive waste are slightly worse than that of normal cement paste and slightly decrease with increasing the percentage of substitutes. The use of expanded clay in mortar and concrete not only helps in obtaining lighter materials, but also improves their thermal and acoustic properties (Merino et al. 2017). The thermal conductivity of cement composites mixed with olive waste was investigated in (Liuzzi et al. 2017). A decrease in density and thermal conductivity in the mixture with olive waste was measured in comparison with a reference sample. An analogous result was concluded for plasters with a content of fibers from olive waste. Based on the study, it can be stated that if the percentage of olive fibers increases, the thermal insulation will increase. Cheboub et al. (2020) replaced natural sand in cement mortar with olive waste and investigated its physical, mechanical, thermal, and acoustic properties. The results showed a decrease in both compressive and bending strengths. The heat insulating and acoustic properties of these samples were also better compared to the reference samples.

The relationship of the density, thermal conductivity, and compressive strength to the proportion of the olive waste in the samples mixed with olive waste was observed in (Belkharchouche et al. 2016). In this research, all the results obtained in the thermal and mechanical tests showed that the addition of olive pomace fibers slightly improved the thermal and mechanical parameters. More studies on the use of olive waste in lightweight concrete can be found in a review paper (Junaid et al., 2022).

In this paper a preliminary characterization of the aggregates, olive waste, and sand is presented. To determine the geometric properties of the aggregate, a sieving and granulometry method is applied. In addition, tests using a pycnometer are carried out to determine the apparent volume density and water absorption. The potential of olive waste for possible use as a lightweight aggregate in cement mortars is stressed; it is worth pointing out that replacement of expanded clay could be viably used in olive producing countries. The main goal is to prepare mortars with properties similar to traditional ones, but which are more ecofriendly. Another goal that could be achieved simultaneously would be to recycle organic (olive) waste in the large amounts produced in many countries that would not be otherwise used industrially, thereby providing the potential for a new production cycle.

2 EXPERIMENTAL PART

2.1 Specimens

The cement used in this study was CEM II / A-V 42.5 R according to EN 197-1, which was supplied by CEMEX. The cement complies with what is specified in the Instruction for the reception of Spanish cement RC-16, published by RD 256/2016 (MTMAU, 2016) as ordinary cement, CEM II, Portland cement with fly ash, strength class 42.5, and high initial strength.

As a result of their being crushed in the oil mills as residue from the olive industry, olive stones could be a partial substitute for natural sand. Specifically, two different types of olive stones have been used with different granulometric characteristics called (see Fig. 1): MIX (1 mm – 4 mm), and FINE (0.1 mm – 2 mm). All these products have been supplied by the company Peláez Renovables S.L. located in Jaén, southern Spain.

2.2 Granulometry test

The first test to characterize an aggregate to be used in mortar is the granulometry test (see Fig. 2). This sand granulometry test is conducted according to standards EN 933-1 and EN 933-2. This test provides the sizes of the aggregates that make up the sand; it also allows us to determine the content of fines or fillers (whose coarse sizes are less than 0.063 mm in sand). The size of sieve openings is 2 mm – 1 mm – 0.5 mm – 0.25 mm – 0.125 mm – 0.063mm – bottom. All the equipment meets the general requirements according to EN 932-5.

We used the following equipment: test sieves with openings as specified in EN 932-5 according to standards ISO 3310-1 and ISO 3310-2. The minimum sample mass for the granulometry test for aggregates with a grain size of up to 4 mm is 200 g.

This process was carried out as follows:

1. A sample weighing over 800 g was taken from the base. In order to obtain an evenly divided sample of 200 g into different fractions, a distributor was used.
2. The test portion was placed in a tray, and sufficient water was added to cover it; all the organic waste and

(a) (b)

Fig. 1 *Fractions of olive stones: the FINE fraction (0.1 mm – 2 mm) on the left and the MIX fraction (1 mm – 4 mm) on the right.*

(a) *(b)* *(c)*

Fig. 2 *A set of sieves (a). Quartering, dividing the sample (b). Screening method and material used (c).*

fine aggregates were washed away. The samples were washed with a sufficient force of water flow to obtain the complete separation and suspension of the fines. The retained aggregate and residue were dried in a laboratory drying oven of (110 ± 5) ºC, over 24h, up to a constant mass. Then it was allowed to cool; it was weighed, and its mass was recorded.

3. The washed and dried material was set into the sieving column. The column was shaken manually for approximately 1 min. The sieves were then removed one by one, starting with the larger opening size (4 mm). Each individual sieve was shaken again manually for 1 min. All the material that passed through each sieve was transferred to the next sieve in the column. This procedure was repeated down to the smallest sieve (0.063 mm). The sieving process should be considered completed when additional sieving does not entail a change in the mass of the material retained on any sieve greater than 1.0 % of the mass. The finest particles (less than 0.063 mm) that were collected at the bottom were weighed and added to the total mass of the fines (i.e., the washed particles along with the sieved particles amounted to the total mass of fine particles).
4. The material retained by the sieve was weighed, and its mass was recorded. The same operation was continued for all the sieves in the column in order to obtain the masses of the different particle sizes. Then, the test was repeated three times with different samples and masses to get an average value.

The material fractions obtained by this process are shown in Fig. 3.

Fig. 3 *Material divided according to factions.*

2.3 Determination of the bulk density and absorbency of a material

The test to determine the bulk density of the grain and the water absorption of the test sample was carried out according to the standard EN 1097-6. The samples were selected in accordance with standards EN 932-1 and EN 932-2.

We used a pycnometer in the measurement with a 500 ml volume, a metal mold in the form of a cone stem (40 ± 3) mm in diameter at the top, (90 ± 3) mm diameter at the bottom, and (75 ± 3) mm high (a minimal thickness of 0.8 mm), and a metallic rammer of mass (340 ± 15) g with a flat circular ramming surface of (25 ± 3) mm diameter for use with a metal mold.

The pycnometer method was used for aggregate particles passing the 4 mm test sieve that were retained on the 0.063 mm test sieve. The mass of the 0.063 mm / 4 mm test aggregate portion was not less than 300 g.

The prepared test portion was immersed in water at (22 ± 3) ºC in the pycnometer; trapped air was removed by turns and careful shaking of the pycnometer in an inclined position (see Fig. 4). The pycnometer was left in the water bank, and the test portion was kept at a temperature of (22 ± 3) ºC for (24 ± 0.5) h. At the end of the immersion period, the pycnometer was removed from the water bath, and any trapped air was removed by twisting and carefully shaking the pycnometer.

The water temperature was recorded. Most of the water covering the test portion was decanted, and the pycnometer was emptied into a tray. The submerged test portion was spread in a single uniform layer over the bottom of the tray. The sample was exposed to a tempered air stream carefully to evaporate any surface moisture (see Fig. 4). To assess whether the state of the surface drying had been reached, a metal conical mold with its larger opening face down on the bottom of the tray was held. The conical mold was filled with part of the portion of the sample in the drying test.

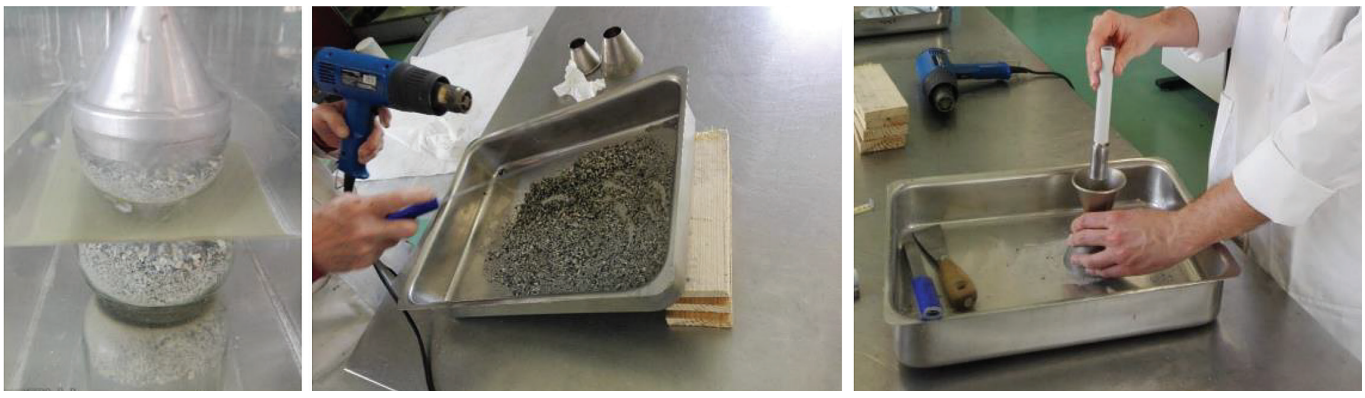

(a) ***(b)*** ***(c)***

Fig. 4 *A pycnometer filled with an aggregate sample and water immersed in a tank with water and a thermostat (a). The content of the pycnometer in the container, drying (b). A testing cone with a rammer (c).*

(a) (b) (c)

Fig. 5 *The cone test to determine the water absorption of sand: a compact cone, a saturated sample (a); a less compact cone, a less saturated sample (b); a broken cone, an almost unsaturated sample (c).*

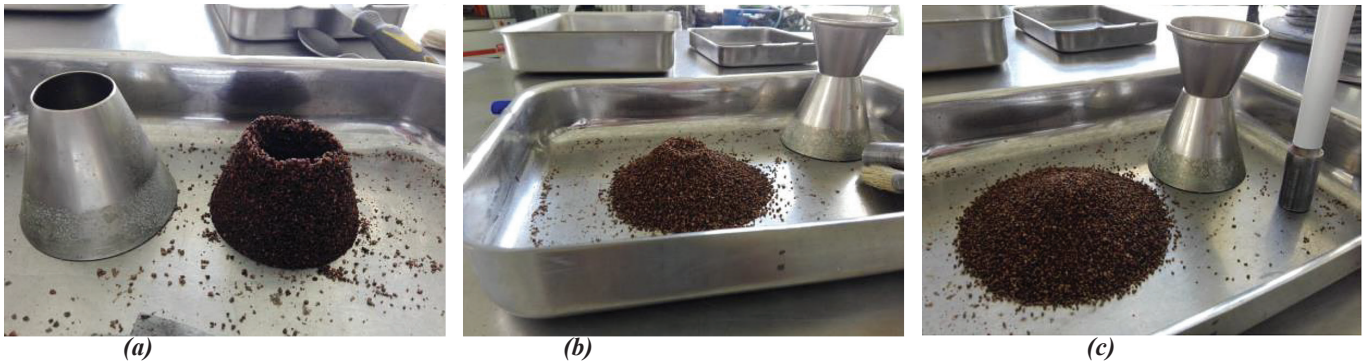

(a) (b) (c)

Fig. 6 *The cone test to determine the water absorption of FINE olive stones: a compact cone, a saturated sample (a); a less compact cone, a less saturated sample (b); a broken cone, an almost unsaturated sample (c).*

Through the hole in the upper part of the mold, the metal tamper-rammer was placed on the surface of the sample (see Fig. 4). The surface was compacted 25 times by dropping the rammer by its own mass. The mold was not refilled after compacting. After that, the mold was carefully lifted; if the cone of the aggregate did not crumble, it continued drying, and the cone test was repeated until crumbling occurred upon removal of the mold.

The saturated and surface dried test portion was weighed. The aggregate was dried in a ventilated stove at a temperature (110 ± 5) ºC until a constant mass was reached. The sample was allowed to cool to room temperature and then weighed.

Drying took place in stages. With the help of the test cone (see Fig 4), the moisture status of the sample was determined. A metal conical mold with a wider surface was placed on the container and filled with the mass. Through the hole in the upper part of the mold, the surface of the mass was compacted with a rammer (see Fig 4). The hammering took place with 25 drops of the hammer from a height of 2 cm from the upper edge of the cone onto the surface of the sample. The mold was later carefully lifted without shaking the aggregate. If the cone of the aggregate did not fall apart, it was compact; the drying and pounding procedure was repeated. According to the standard EN 1097-6, the moisture status of the sample was checked until the sample was surface dried. The methods of evaluation are shown in Fig 5.

The slightly inner saturated and surface-dried sample (together with the container) was weighed. The surface-dried aggregate together with the container was placed in a dryer for (24 ± 0.5) h at a temperature of (110 ± 5) ºC. After this time, the sample was removed from the dryer, allowed to cool to a constant room temperature, and then weighed. Then, the test was repeated three times with different samples and masses to get an average value.

The same pycnometer method used for the sand aggregate was applied to determine the bulk density and water absorption of the olive stones (see Fig 6). The pycnometer was filled with olive stones only to 1/3 of its volume due to dimensional changes. Norm EN 1744-1:2010+A1 and the pycnometric method for aggregate particles of an organic origin were followed. The surface-dried aggregate together with the container were placed in a dryer for (24 ± 0.5) h at a temperature of (85 ± 5) ºC.

The determination of (a) the bulk density of particles, ρ*a*, (b) the bulk density of particles after drying, ρ*rd*, and (c) the bulk density of particles saturated only on the surface, ρ*ssd* was made using the formulas:

$$\rho_a = \rho_w \frac{m_4}{m_4-(m_2-m_3)},$$
$$\rho_{rd} = \rho_w \frac{m_4}{m_1-(m_2-m_3)}, \quad (1)$$
$$\rho_{ssd} = \rho_w \frac{m_1}{m_1-(m_2-m_3)},$$

where ρ_w is the density of water at the temperature during the test (in thousands of kg/m^3 according to norm EN 1097-6); m_1 (kg) is the mass of a saturated sample dried only on the surface; m_2 (kg) is the mass of a pycnometer filled with water and a sample; m_3 (kg) is the mass of a pycnometer filled only with water; and m_4 (kg) is the mass of a dried sample cooled to a stable temperature. The water absorption of particles after 24 h was calculated as

$$WA_{24} = 100 \times \frac{m_1 - m_4}{m_4} \ (\%). \quad (2)$$

The calculations were verified by the formula $\rho_{ssd} = \rho_{rd} + \rho_w(1 - \rho_{rd}/\rho_a)$.

3 RESULTS

According to the granulometry test, the size parameters of the aggregate and sand grains were distinguished. This test made it possible to determine the content of the fine particles. The fraction of the aggregate used was Ø 4 mm / 0.063 mm. The test results, which are presented in Fig. 7, showed that the fine particles washed away together with the particles caught at the bottom of the sieves had a mass of 29.78 g. The total percentage of the share of fine particles in the aggregate was 14.9 %. Then, to get an average value, the test was repeated 3 times with different samples and masses. The average value of the fine particles in the aggregate was 15.3%. The test results also showed that the percentage of fine particles in the aggregate was not sufficient for the optimal dosage of cement mortar and that the addition of fine additive particles is necessary. The optimal parameter is 20 % to 25 % of the content of fine particles of the total mass of the dry mixture of the cement mortar. We could achieve the required percentage of fine particles by adding another inorganic aggregate, such as fly ash.

To determine the bulk density and water absorbency of the materials, the pycnometer method was used for the aggregate particles (sand) falling through a 4 mm test sieve and retained on a 0.063 mm sieve. The results from a single experiment are given in Table 1. To get average values, the test was repeated 3 times with different samples and masses. The results show that the average water absorption of the aggregate is WA24 = 0.35 % and that the bulk density of the particles is 2710 kg/m3 (see Fig. 8). The water absorption of the arid aggregate was 0.35 % on average with a standard deviation of 0.02 %.

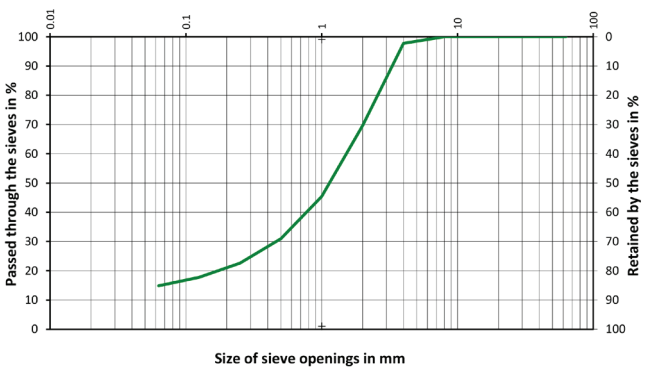

Fig. 7 *The granulometric curve of the aggregate particles.*

The bulk density and water absorption of the olive stones were determined by the pycnometric method for aggregate particles of an organic origin. Examples of a single test for both the FINE and MIX samples are given in Table 1. The calculations and procedures were the same for the pycnometric method as for the aggregate. Again, to get the average values, the test was repeated 3 times with different samples and masses. As expected, the water absorption of the olive stones was much higher than that of the conventional aggregate, which is normally below 1%.

The average water absorption of the FINE olive waste was WA_{24} = 28.2 %, and the bulk density of the particles was 1380 kg/m^3, while for the MIX olive waste it was WA_{24} = 25.1 %, and the bulk density of the particles was 1390 kg/m^3 (see Fig. 8). Thus, the FINE olive stones absorbed more water than the MIX olive stones. The standard deviations for the water absorption were 0.16 % for the FINE and 1.12 % for the MIX olive stones.

Tab. 1 *Data from a single set of experiments used to calculate the water absorption. Three sets were used to calculate the average values and standard deviations.*

Material	m_1 (g)	m_2 (g)	m_3 (g)	m_4 (g)	ρ_a (kg/m^3)	ρ_{rd} (kg/m^3)	ρ_{ssd} (kg/m^3)	WA_{24} (%)	St.dev. (%)
Aggregate	401.60	953.50	700.90	400.25	2711	2686	2695	0.35	0.02
FINE	127.60	726.10	698.90	99.40	1377	990	1271	28.24	0.16
MIX	130.00	728.80	699.90	103.90	1385	1028	1286	25.12	1.12

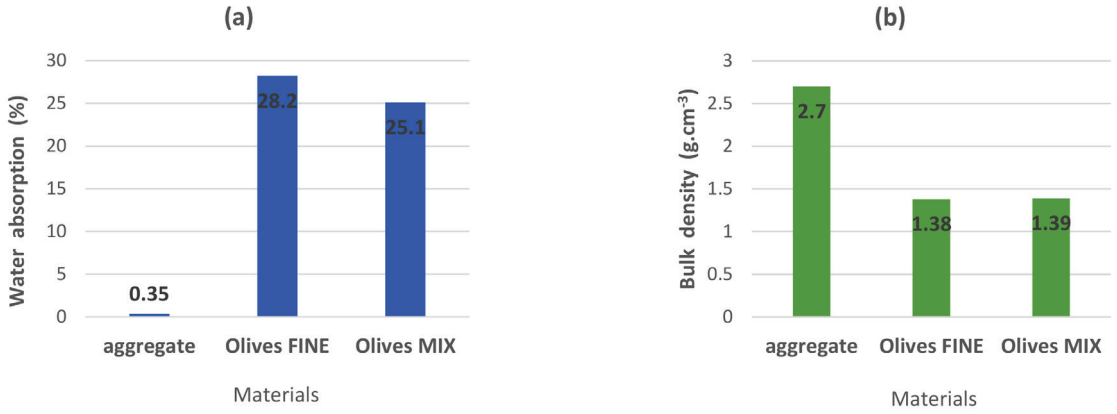

Fig. 8 *The average water absorption (a) and bulk density (b) of the aggregate particles and FINE and MIX olive stones.*

4 CONCLUSIONS

A preliminary analysis of the materials originating from olive waste (two types of crushed olive stones, i.e., FINE and MIX) was carried out with a view to its further use as part of building materials. Their use would result in a decrease in the amounts of aggregate or sand that are used in building materials, thereby leading to both environmental and economic benefits. Measurements of granulometry, bulk density and water absorption were performed. The average value of fine particles in the aggregate was 15.3 %, whereas the optimal value (20 % to 25 %) of fine particles would require adding a suitably fine inorganic aggregate, such as fly ash. It would not be a good idea to use milled olive stones because they have a different bulk density in comparison to inorganic additives (a different cohesion with a cement matrix) and a much higher absorption coefficient of water (causing a major swelling effect). In addition, the average value of the water absorption for the aggregate (0.35 %) was much lower than for the FINE and MIX olive stones (28.2 % and 25.1 %, respectively). Thus, the water absorption for either organic material attained values common in the scientific literature. Finally, the bulk densities of the olive stones (1380 kg/m^3 and 1390 kg/m^3) are satisfactory, thereby resulting in a decrease in the bulk densities of the final products. All the results indicate that both organic materials can be promising for their use as an input aggregate for the production of lightweight building materials. Further research on their effect on the physical and mechanical properties of the final cement composites is required.

REFERENCES

Alkheder, S. – Obaidat, T. Y. – Taamneh, M. (2016) *Effect of olive waste (Husk) on behavior of cement paste*: Case Studies in Construction Materials, Vol. 5**,** pp. 19–25.

Aouba, L. – Bories, C. – Coutand, M. – Perrin, B. – Lemercier, H. (2016) *Properties of fired clay bricks with incorporated biomasses: Cases of Olive Stone Flour and Wheat Straw residues*. Construction and Building Materials, Vol. 102, pp. 7–13.

Belkharchouche, D. – Chaker, A. (2016) *Effects of moisture on thermal conductivity of the lightened construction material.* International Journal of Hydrogen Energy, Vol. 41, pp. 7119-7125

Bourema, M. – Goual, I. – Ferhat, A. (2023) *Experimental contribution to study the Physico- mechanical and thermal properties of Lightweight cellular concrete prepared with different types of sand and waste marble powder.* Slovak Journal of Civil Engineering, Vol. 31, No.4, pp. 16-25. DOI: 10.2478/sjce-2023-0023.

Cheboub, T. – Senhadji, Y. – Khelafi, H. – Escadeillas, G. (2020) *Investigation of the engineering properties of environmentally friendly self-compacting lightweight mortar containing olive kernel shells as aggregate.* Journal of Cleaner Production, Vol. 249, art. no. 119406.

EN 197-1 (2011). Cement – Part 1: Composition, specifications and conformity criteria for common cements.

EN 932-1 (2018). Tests for general properties of aggregates – Part 1: Methods for sampling.

EN 932-2 (2022). Tests for general properties of aggregates – Part 2: Methods for reducing laboratory samples.

EN 932-5 (2012). Tests for general properties of aggregates - Part 5: Common equipment and calibration.

EN 933-1 (2012). Tests for geometrical properties of aggregates – Part 1: Determination of particle size distribution – Sieving method.

EN 933-2 (2020). Tests for geometrical properties of aggregates - Part 2: Determination of particle size distribution - Test sieves, nominal size of apertures.

EN 1097-6 (2022). Tests for mechanical and physical properties of aggregates – Part 6: Determination of particle density and water absorption.

EN 1744-1:2010+A1 (2013). Tests for chemical properties of aggregates – Part 1: Chemical analysis.

ISO 3310-1 (2016). Test sieves. Technical requirements and testing Test sieves of metal wire cloth.

ISO 3310-2 (2013). Test sieves. Technical requirements and testing Test sieves of perforated metal plate.

Junaid, M. F. – Rehman, Z. U. – Kuruc, M. – Medved, I. – Bacinskas, D. – Curpek, J. – Cekon, M. – Ijaz, N. – Ansari, W. S. (2022) *Lightweight concrete from a perspective of sustainable reuse of waste byproducts.* Construction and Building Materials, Vol. 319, art. no. 126061.

Liuzzi, S. – Rubino, CH. – Stefanizzi, P. (2017) *Use of clay and olive pruning waste for building materials with high hygrothermal performances.* Energy Procedia, Vol. 126, pp. 234–241.

Merino, M. R. –Rodríguez, J. G. – Martínez F. F. – Astorqui, J. S. C. (2017) – *Viability of using olive stones as lightweight aggregate in construction mortars.* Revista de la Construcción, Vol. 16., pp. 431 -438.

MTMAU (Ministerio de Transportes, Movilidad y Agenda Urbana) **(2016)** Real Decreto 256/2016, de 10 de junio, por el que se aprueba la Instrucción para la recepción de cementos (RC-16). In Spanish.

Priyanka, A. – Jadhav, D. – Kulkarni, K. (2013) *Effect of replacement of natural sand by manufactured sand on properties of cement mortar.* International Journal Civil and Structural Engineering, Vol. 3, pp. 621–628.

Shafigh, P. – Bin Mahmud, H. – Bin Jumaat, M. Z. – Ahmmad, R. – Bahri, S. (2014) *Structural lightweight aggregate concrete using two types of waste from the palm oil industry as aggregate*. Journal of Cleaner Production, Vol. 80, pp. 187–196.